Magnetic Studies of an Effective Field Model and Several Potentially Re-entrant Palladium Alloys

Kirk Russell Kornik
(University of Manitoba)

A thesis presented to the
University of Manitoba
in fulfillment of the
thesis requirement for
the degree of
Master of Science
in the
Department of Physics.

Winnipeg, Manitoba

ISBN 0-315-63211-9

MAGNETIC STUDIES OF AN EFFECTIVE FIELD MODEL AND SEVERAL POTENTIALLY RE-ENTRANT PALLADIUM ALLOYS

BY

KIRK RUSSELL KORNIK

A thesis submitted to the Faculty of Graduate Studies of the University of Manitoba in partial fulfillment of the requirements of the degree of

MASTER OF SCIENCE

Abstract

The static magnetization of three very dilute Pd alloys, containing 700 ppm Fe, 700 ppm Mn, and 1000 ppm Mn, was measured for temperatures between 50 milli-K and 1 K, and applied fields of up to 10 Gauss. The zero-field-cooled data possess features which can be replicated by numerical calculations based on a mean-field effective field model with exchange-bond disorder and arbitrary spin. Moreover, the comparisons suggest that the alloys are within the re-entrant region of the magnetic phase diagram, and hence undergo sequential transitions, from paramagnetic to ferromagnetic to spin glass ordering, as the temperature is lowered.

The time dependent thermo-remanent magnetization of the 700 ppm Fe sample, as measured over 7200 seconds for several temperatures above and below the proposed re-entrant transition temperature, is consistent with a logarithmic (or possibly a stretched- exponential) decay. However, the relaxation rate is apparently temperature independent.

Detailed numerical calculations of the theoretical differential susceptibility reveal a singular anomaly in the non-linear components near the re-entrant transition temperature. Furthermore, experimental A.C. susceptibility isotherms, measured below the proposed re-entrant transition temperature of a $(\mathbf{Pd}_{0.9965}\mathrm{Fe}_{0.0035})$ + 5 *at.*% Mn sample, display systematics which are strikingly similar to the theoretical investigations. The analysis illustrates a potentially useful technique for identifying re-entrant transitions in experimental systems.

Acknowledgements

Firstly, I thank my advisor Dr. Roy Roshko for his kind (and patient!) guidance over the past few years. Special thanks also go to Wenxin Ruan and Dr. Henry Kunkel for their expert assistance with sample preparation and data aquisition. I also thank the above mentioned persons, and Dr. G. Williams, for the many useful and informative discussions in which they played a role. Last but not least, I thank my family and friends, without whose support this thesis would not have been possible.

Contents

Chapter 1

Introduction and Theory

1.1 General Background

1.1.1 Phase Transitions in Pure Ferromagnets

Magnetic Ordering in Iron-like Metals

The traditional concepts of magnetic phase transitions are typefied by the properties of (non-dilute) transition metals such as Iron or Nickel. These systems display a form of critical phenomenon; a transition (at the Curie temperature) between a low temperature ferromagnetic phase and a high temperature paramagnetic phase.

To describe the physics of magnetic materials it is necessary to approach the problem at an atomic level. Each atom in an Iron-like metal lattice has a net spin $\vec{S}$ and a corresponding magnetic dipole moment $-g\mu_B\vec{S}$ ($g = 2$ is the Landé factor, and $\mu_B = e\hbar/2m_ec$ is the Bohr magneton), due mainly to the incomplete filling of the $3d$-band electron states. The inhomogenous electric field produced by the ions in the crystal tends to quench the orbital moments so that the effects of spin-orbit coupling may be ignored. Though the magnetic properties are best

described by non-localized (itinerant) electron models, it is convenient to assume that the electrons are localized on the lattice sites. With the application of a uniform external magnetic field $\vec{H}_0$, the dipoles tend to align themselves along the field direction to minimize energy. Summing over the lattice sites, the magnetic energy is given by

$$g\mu_B \sum_i \vec{H}_0 \cdot \vec{S}_i \quad .$$

The resulting paramagnetic ordering must compete with random thermal motions of the spin orientations. If there are no other sources of magnetic order, the magnetization drops to zero when the field is removed.

In ferromagnetic systems, there exists another much stronger source of magnetic order. The *direct exchange interaction* is actually a consequence of the Coulombic repulsion of electronic charge distributions, together with the Pauli exclusion principle. It is characterized by the exchange energy J, between two electronic wavefunctions Φ_1 and Φ_2, such that (after Cohen-Tannoudji et al., 1977)

$$J = \int d^3r_1 \int d^3r_2 \, \Phi_2^*(\vec{r_1}) \, \Phi_1^*(\vec{r_2}) \, \frac{e^2}{\mid \vec{r_1} - \vec{r_2} \mid} \, \Phi_1(\vec{r_1}) \, \Phi_2(\vec{r_2}) \quad ,$$

where the magnitude depends on the amount of *overlap* between the wavefunctions. If J is positive, antisymmetric wavefunctions minimize the energy and overall symmetry considerations require the spin states to be symmetric. That is, parallel arrangements of the spin orientations are favoured. It is important to note that the direct exchange between the atoms in a lattice is of relatively short range, and only neighboring spins interact strongly.

The interaction between all the spins of the lattice can be modelled using the Heisenberg Hamiltonian,

$$-\frac{1}{2}\sum_{i,j} J_{ij}\vec{S}_i \cdot \vec{S}_j \quad ; \; J_{ij} = J_{ji}, \;\; J_{ii} = 0 \quad ,$$

where the exchange parameter J_{ij} determines the strength of the interaction between the ith and jth spins (and is related to the exchange integral above). Positive parameters favour parallel alignment of the spins, and there is a spontaneous magnetization (ferromagnetism) as long as thermal fluctuations do not overwhelm the magnetic order. Alternatively, negative parameters favour anti-parallel or anti-ferromagnetic alignment of the spins.

In the exact mean-field theory of ferromagnetism, the individual J_{ij} are assumed to be of infinite range, and are replaced by an average exchange bond $\overline{J_0}/N$, where N is the number of spins in the system. Only spin components ($S_{iz} \equiv S_i$) along the field direction are considered so that the magnetic energy is described by an Ising Hamiltonian

$$\mathcal{H} = -\frac{\overline{J_0}}{2N}\sum_{i,j} S_i S_j - h\sum_i S_i \quad ,$$

where $h = -g\mu_B H_0$. The magnetization (or net dipole moment per volume V) of the system is obtained by evaluating the partition function and ensemble averaging the spins, over the thermal fluctuations, in the thermodynamic limit ($N \to \infty$). The result is a transcendental equation which, for arbitrary quantum

spin $\vec{S}$ (i.e., $-S \leq S_i \leq S$), is

$$\langle S_i \rangle_T \equiv m = S B_S\Big[S\beta\left(\overline{J_0} m + h\right)\Big] \quad ; \quad \beta = \frac{1}{k_B T} \quad . \tag{1.1}$$

The local magnetization m is related to the bulk value of $M = Ng\mu_B m$. For $S_i = \pm 1/2$, the Brillouin function (equation 1.56) simplifies to $B_{1/2}[x] = \tanh[x]$. As can be seen in Figure 1.1, there is good agreement between experimental results and mean-field theory calculations, despite the simple nature of the model. For temperatures $T \rightarrow 0$ the magnetization reaches its saturation value of $M_{sat} = Ng\mu_B S$. As T is increased, thermal fluctuations gradually overcome the ferromagnetic order, until the spontaneous magnetization $M_0 = M(0,T)$ disappears at the Curie temperature T_c. The zero-field susceptibility $\chi_0 = \left(\frac{\partial M}{\partial H_0}\right)_{H_0=0}$ in the paramagnetic region ($T > T_c$) is predicted by mean-field theory to obey a Curie-Weiss law:

$$\chi_0 = \frac{C}{(T - T_c)} \quad \text{where} \quad C = \frac{Ng^2\mu_B^2 S(S+1)}{3Vk_B} \quad . \tag{1.2}$$

Experiments have shown this to be valid for large temperatures, but incorrect for temperatures close to T_c. The Curie temperatures tend to be quite large, with $T_c = 1043$K for Iron, and 627K for Nickel (after Kittel, 1976).

The Ehrenfest Criterion

The transition between paramagnetism and ferromagnetism is a phase change in the traditional thermodynamic sense. Consider the following expression for the

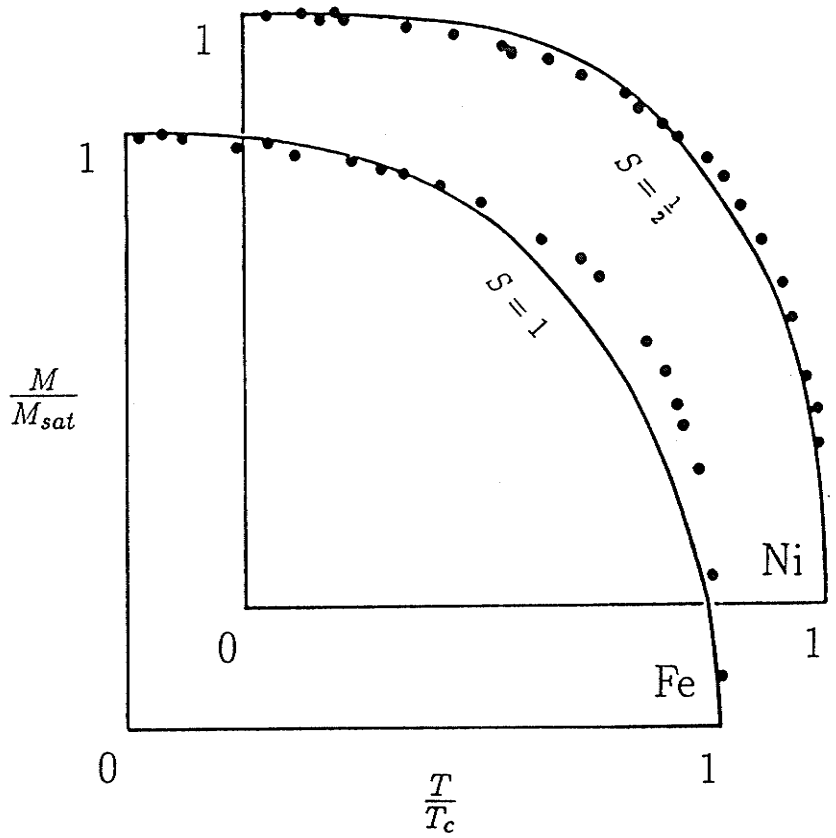

Figure 1.1: A comparison between the exact mean-field theory of ferromagnetism (for spin $S = 1$ and $S = 1/2$) and experimental magnetization measurements (•) on pure Fe and Ni (after Stanley, 1971).

differential Gibbs free energy of a magnetic system:

$$dg = -S\,dT - M\,dH \quad ,$$

where S is the entropy. The isothermal susceptibility is defined as (Ausloos and Elliott, 1983)

$$\chi = \left(\frac{\partial M}{\partial H}\right)_T = -\left(\frac{\partial^2 g}{\partial H^2}\right)_T \quad , \tag{1.3}$$

while the specific heat is given by

$$C_H = -T\left(\frac{\partial^2 g}{\partial T^2}\right)_H \quad . \tag{1.4}$$

By the Ehrenfest criterion, a phase transition occurs whenever there is a discontinuity in a derivative of the Gibbs function, with the order of the transition defined by the lowest order derivative in which the discontinuity occurs. In this regard, the ferromagnets display second-order phase changes since their susceptibilities and specific heats, evaluated in zero field and as a function of T, diverge as the Curie temperature is approached. (We shall ignore, for the present time, the effects of magnetic domains and sample demagnetization, etc., which can artificially suppress the singular behavior of experimental systems.)

Critical Phenomena

In ferromagnetic systems, the zero-field (spontaneous) magnetization plays the part of an *order parameter*, and indicates the breaking of symmetry that occurs in going from the high-symmetry paramagnetic state to the low-symmetry

ferromagnetically ordered state. Also, the transition is an example of a *critical phenomenon* because of the characteristic way in which various thermodynamic functions behave as the Curie (or critical) temperature is approached from above and below.

A simplified physical interpretation of critical phenomena (in ferromagnetic systems) is as follows. For $T \gg T_c$, the direct exchange interactions (between the spins of the system) are completely overwhelmed by thermal agitation of the spins, and there is no spontaneous magnetic order. However, for lower temperatures $T > T_c$ the fluctuations are weakened enough to allow short range local ordering in isolated parts of the system. That is, small islands of ferromagnetic order begin to develop, but the net magnetization is still zero since the islands are too far apart to affect one-another. As $T \rightarrow T_c$, the islands grow in size and their moments start to interact and align along a common direction. Finally, when $T = T_c$ the islands link together to form a network of long-range ferromagnetic order which extends throughout the system. Hence, the spontaneous magnetization develops suddenly (but continuously) at T_c. The Curie-Weiss law (equation 1.2) is incorrect close to T_c because the mean-field theory does not allow for the occurrence of short-range order.

Critical behavior (not only in magnetic systems) is classified according to how the appropriate order parameter, susceptibility, and specific heat vary near the critical point. For a ferromagnet in zero-field we write the following power laws (after Ausloos and Elliott, 1983):

$$M(H = 0, t < 0) \sim (-t)^{\beta}$$

$$\begin{aligned} \chi(H=0,t<0) &\sim (-t)^{-\gamma'} \\ \chi(H=0,t>0) &\sim (t)^{-\gamma} \\ C_H(H=0,t<0) &\sim (-t)^{-\alpha'} \\ C_H(H=0,t<0) &\sim (t)^{-\alpha} \quad , \end{aligned} \tag{1.5}$$

where we have introduced the reduced temperature $t = (T - T_c)/T_c$ and assumed the limit $t \rightarrow 0$. Additionally, the field dependence along the critical isotherm $T = T_c$ is given by

$$M(H, t=0) \sim H^{1/\delta} \quad . \tag{1.6}$$

Critical systems are grouped into *universality classes* according to the values of the critical indices, and in the most general cases the exponents are related to one-another through inequalities. For ferromagnets, however, the free energy is a homogenous function such that (after Ausloos and Elliott, 1983)

$$f(a^x H, a^y t) = a\, f(H,t) \quad , \tag{1.7}$$

where a is arbitrary. The critical exponents (α, β, etc.) can be extracted from x and y by performing the appropriate derivatives, so that (after Stanley, 1971)

$$\begin{aligned} \beta &= (1-x)/y \quad , \\ \gamma = \gamma' &= (2x-1)/y \quad , \\ \alpha = \alpha' &= (2y-1)/y \quad , \\ \delta &= x/(1-x) \quad . \end{aligned}$$

They are related to one-another through equalities such as the Widom relationship (Ausloos and Elliott, 1983)

$$\gamma = \beta(\delta - 1) \quad . \tag{1.8}$$

For example, the mean-field Ising model predictions are $\beta = \frac{1}{2}$, $\gamma = 1$, and $\delta = 3$.

The critical behavior can consequently be described using *static scaling functions*. For instance, differentiating both sides of equation 1.7 with respect to H yields:

$$\begin{aligned} \frac{\partial f\left(a^x H, a^y t\right)}{\partial\left(a^x H\right)} \frac{\partial\left(a^x H\right)}{\partial H} &= a \frac{\partial f(H,t)}{\partial H} \\ a^x M\left(a^x H, a^y t\right) &= a M(H,t) \quad , \end{aligned} \tag{1.9}$$

where $M = -\partial f / \partial H$ has been used. Furthermore, a value of $a = |t|^{-1/y}$ may be chosen so that equation 1.9 becomes

$$M(H,t) = |t|^{(1-x)/y} M\left(\frac{H}{|t|^{x/y}}, \pm 1\right) \quad .$$

This expression can be rewritten in terms of critical exponents and a scaling function $F_{\pm}\left(H \,/ |t|^{x/y}\right) = M\left(H \,/ |t|^{x/y}, \pm 1\right)$ (after Stanley, 1971):

$$|t|^{-\beta} M(H,t) = F_{\pm}\left(\frac{H}{|t|^{\gamma+\beta}}\right) \quad . \tag{1.10}$$

The left-hand-side is called the scaled magnetization M, while the argument of the scaling function is the scaled field H. Figure 1.2 portrays a scaled Arrott plot

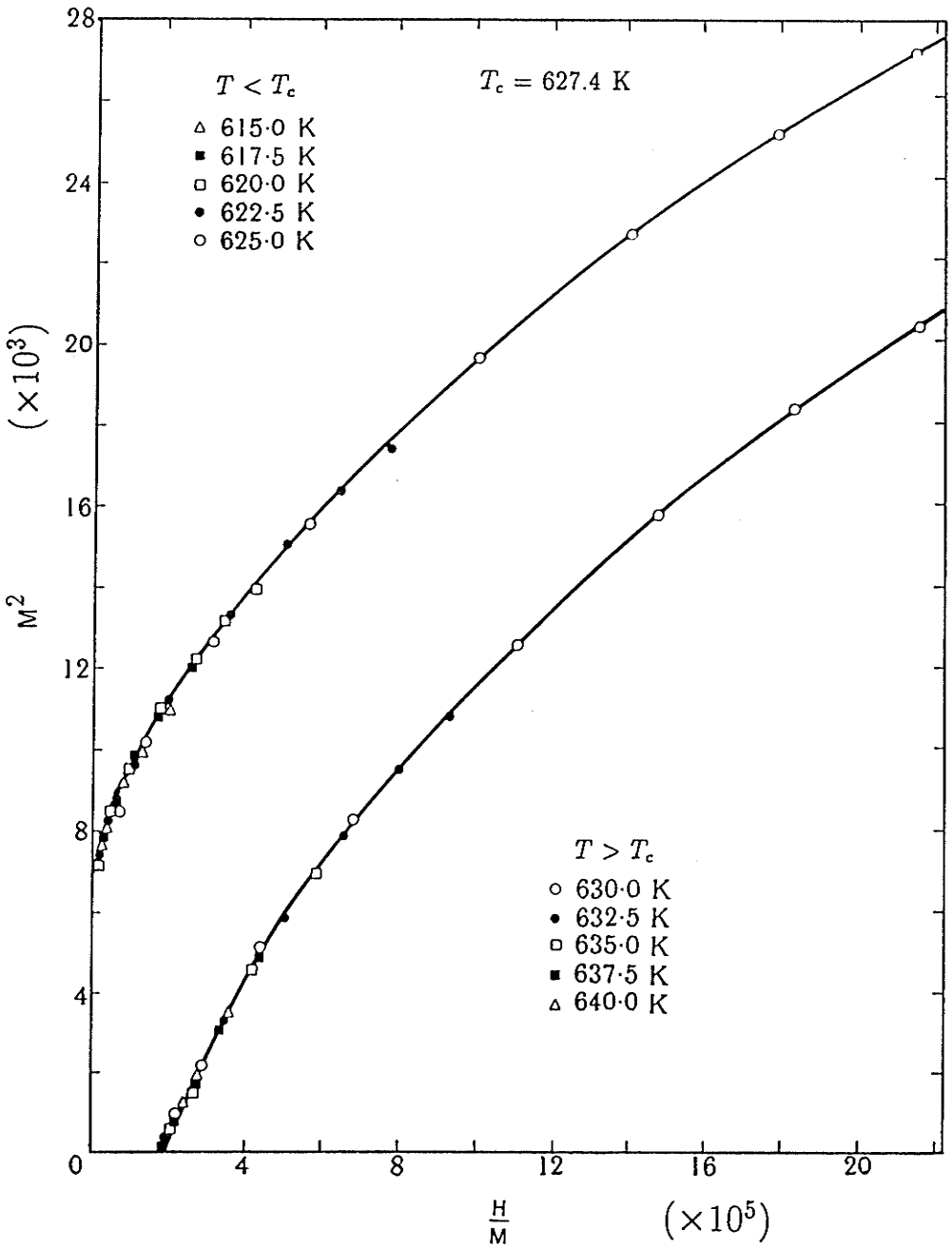

Figure 1.2: A scaling plot for Nickel. The superpositioning of the data points, along the two curves corresponding to $T > T_c$ and $T < T_c$, implies that a critical phase transition occurs at T_c (after Stanley, 1971).

of M^2 versus H/M for Nickel. Notice that all the points for $T > T_c$ fall along a common curve, as do those for $T < T_c$.

A similar equation of state can also be derived for the susceptibility (after Yeung et al., 1987):

$$\chi(H,t) = \chi(0,t) \; - |t|^{-\gamma} \, G_{\pm} \left(\frac{H^2}{|t|^{2\gamma+2\beta}} \right) \quad . \tag{1.11}$$

The term involving $G_{\pm}$ describes the non-linear field dependence of the susceptibility, while the zero-field term represents the linear susceptibility. The leading critical divergence of ferromagnetic systems occurs in the linear term, such that $\chi(0,t) \sim t^{-\gamma}$. This is important from an experimental point of view, since the non-linear response is typically much weaker, and hence more difficult to analyse, than the linear response.

Thus, critical scaling provides an indication of whether an experimental system undergoes a thermodynamic phase transition. Also, the values of the critical exponents are indicative of the universality class to which the system belongs (for example, both metallic Iron and Nickel belong to the same class).

Domain Wall Effects

The presence of a spontaneous magnetization in real ferromagnets is generally not observable at a macroscopic scale, unless an external magnetic field has been applied to the system. In explanation, it is understood that below T_c the specimen is broken up into *magnetic domains* which are separated by thin *domain walls.* Within each domain the spins are near-perfectly aligned (aside from thermal

fluctuations), but to minimize energy, the domain orientations are such that the bulk magnetization of the sample is approximately zero. With the application of a weak field, the regions with favourable magnetization directions tend to grow in size at the expense of others and the sample, as a whole, gains a net magnetization. The associated domain wall displacements may be reversed by applying a field of equal strength but opposite direction. Domain growth is, however, hindered by the pinning of domain walls along point defects or impurities in the metal lattice. With large enough fields, the walls may overcome these obstacles, but the process is irreversible and leads to magnetic hysteresis and a remanent (zero field) bulk magnetization. Still larger fields may rotate the domain magnetizations into favourable directions, despite any magnetic anisotropy in the sample, so that the bulk magnetization can saturate.

Another manifestation of domains is the observed slow (non-exponential) drifting of the magnetization, after a change in the applied field has upset the stability of the domain structure. This relaxation is explained in terms of thermal activation processes which enable the domain walls to eventually overcome pinning obstacles, and hence allow the system to reorganize into a low-energy domain configuration. Typically, the magnetization has a logarithmic time dependence,

$$M(t) = M_0 - S \ln(t) \quad , \tag{1.12}$$

where $S = S(H,T)$ is the magnetic viscosity, and M_0 is the initial magnetization.

1.1.2 Magnetic Interactions in Dilute Alloys

Dilute magnetic alloys are solid solutions formed by substituting magnetic impurity atoms (Fe, Mn, Co, Ni, etc.) randomly throughout the lattice sites of a non-magnetic host metal (such as Au, Cu, Ag, Pd, Pt, etc.). In this context, the hosts may be strongly paramagnetic, but metals with spontaneous magnetic moments are generally excluded. The solute atoms tend to maintain their magnetic moments even while in solution, and varying their concentration effectively allows adjustment of their average separation distance. Moreover, since the impurity-impurity exchange bonds have spatial dependence, the magnetic ordering of randomly-dilute magnetic systems is highly concentration dependent, and displays greater complexity than is found for pure metals. Before introducing the specific experimental properties of these systems, it is helpful to first discuss the magnetic interactions which are thought to be responsible for their magnetic behavior.

Ferromagnetic Ordering in Dilute Systems

Alloys with high concentrations of ferromagnetic impurities tend to behave ferromagnetically, with the Curie temperature roughly proportional to the concentration (Figure 1.3). That is, the relatively close proximity of the magnetic atoms allows positive coupling via direct exchange. The ferromagnetic properties become less pronounced and ultimately disappear upon decreasing the concentration.

Magnetically, the noble metals provide the simplest hosts. Their conduction electrons have weak paramagnetic susceptibilities, and hence are influenced relatively little by the introduction of magnetic atoms into the noble matrix. A

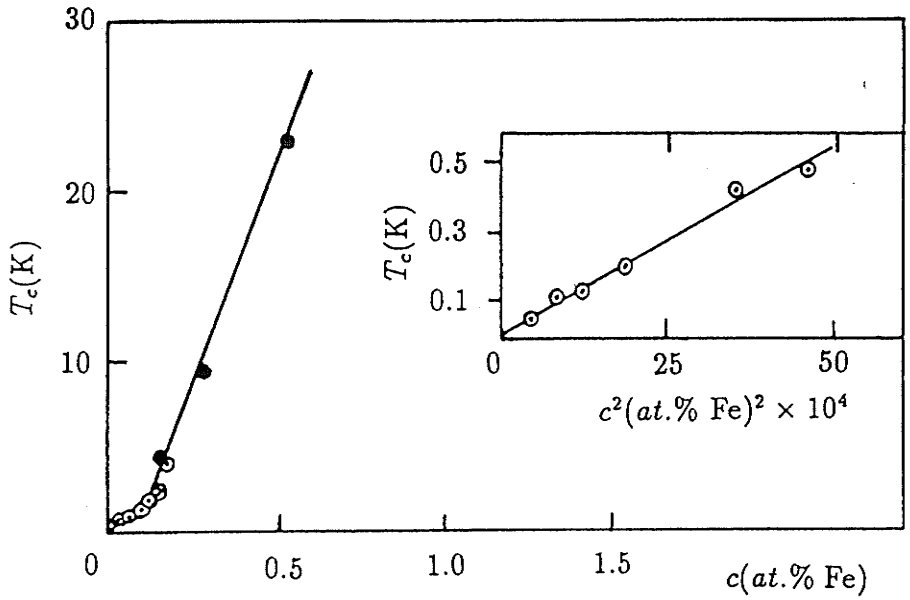

Figure 1.3: Dependence of the Curie temperature of PdFe on the Fe concentration. A change from a c to a c^2 dependence occurs as the concentration is lowered (after Chouteau et al., 1971).

typical example of a binary alloy with an noble metal host is **Au**Fe, which remains predominantly ferromagnetic down to a concentration of 16 *at.*% Fe (Nieuwenhuys et al., 1979).

More interestingly, alloys based on transition metal hosts, such as Pd or Pt, have much lower ferromagnetic percolation limits. Though not quite ferromagnetic, the $4d$ conduction electron band in Pd (and to a lesser extent, the $5d$ band in Pt) has a very large paramagnetic susceptibility. This can be understood in terms of Stoner's band theory of magnetism, where the susceptibility is enhanced by roughly an order of magnitude because of exchange interactions between the electrons within the band (section 1.2.1). These highly-susceptible electrons are itinerant, and the introduction of localized moments (such as Fe atoms) into the Pd matrix induces positive spin polarization of the electrons surrounding each impurity atom. That is, a large spherical *polarization cloud* is formed around each magnetic atom, with the polarization along the direction of the impurity moment. In the case of **Pd**Fe, studies indicate that *giant moments* of up to $10\mu_B$ (Crangle and Scott, 1965) are associated with each cloud (as opposed to about $3\mu_B$ for an Fe atom in a noble host). Furthermore, neutron diffraction experiments by Low and Holden (1966) have shown that the clouds extend $\sim 10\mathring{A}$ from an impurity site and may encompass $\sim$ 200 Pd atoms. The overlap of the clouds effectively enables their giant moments to couple ferromagnetically down to extremely low impurity concentrations. According to Chouteau and Tournier (1971), the ferromagnetic percolation limit of **Pd**Fe is $\sim$ 0.1 *at.*% Fe, at which point the Fe atoms are (on average) 15 to 20 Å apart. Below this limit, the ferromagnetism gradually disappears; the separation distances become too large to allow direct exchange

and it is no longer possible to have, as a ground state, an extensive network of ferromagnetically ordered spins.

Quenched Disorder, Frustration, and Spin Glass Ordering

According to RKKY theory (section 1.2.1), the magnetic polarization of the host's conduction electrons, due to the presence of a localized magnetic impurity moment, is oscillatory in nature so that both the sign and the strength of the polarization varies with the distance from the impurity atom. Consequently, the moment of a second magnetic atom can be influenced by these polarized electrons; hence the impurity spins are indirectly coupled. Because of the long-range characteristics of this indirect exchange, it dominates the magnetic ordering of systems in which the magnetic atoms (or polarization clouds, as the case may be) are too far apart to interact via direct exchange.

The random positioning of the magnetic impurities within such a solid solution is known as *quenched disorder*, as it occurs in addition to, but independent of, the more usual temperature-induced thermal disorder. Theoretically, the combination of quenched disorder and the oscillating RKKY interaction provides a *frustration mechanism.* Each of the impurity moments receives instructions from all the other impurity moments (by means of RKKY exchange bonds) as to which direction it should point. However, because the individual exchange bonds are either ferromagnetic or anti-ferromagnetic, depending on the distance between the atoms, there is random conflict between the types of order. Since no simple parallel or anti-parallel arrangements will simultaneously satisfy all the required exchange couplings, the spins are said to be frustrated, and they must *coopera-*

tively determine a configuration which satisfies the random exchanges. Infinitely many stable solutions are possible, but they are all characterized by freezing of the impurity spins into random orientations. There is no long range magnetic order in the usual sense, and hence no spontaneous magnetization. As in ferromagnetic systems, this frozen order must compete with thermal fluctuations, and gives way to the more usual paramagnetic ordering above some freezing temperature T_{SG}. The term *spin glass* is commonly used to denote the ground state of such systems.

A great deal of experimental and theoretical research has been aimed towards identifying spin glass systems, and characterizing the spin glass/paramagnetic transition in terms of critical phenomena. Apparently, **Pd**Fe alloys are spin glasses only up to 0.01 *at.*% Fe (Peters et al., 1984) since the large spatial extent of the polarization clouds enables some long-ranged ferromagnetic coupling to occur, even at extremely low concentrations. Also, the paramagnetic/spin glass transition temperature is given by $T_{SG} \simeq 0.83 \frac{K}{at.\%Fe} X$, where X is the Fe concentration.

The situation in **Au**Fe is more complex (Coles et al., 1978), due to metallurgical considerations. Without exchange enhancement, the spin glass ordering begins at a much higher concentration, and it is statistically more likely that some short-ranged ferromagnetic ordering will occur randomly throughout the system. Below 8 *at.*% Fe, the system is an archetypical spin glass. However, from 8 to 24 *at.*% Fe, it condenses into clusters of ferromagnetically ordered spins which grow in size with increasing concentration. The clusters interact via the the RKKY mechanism so that their moments are frustrated and have *cluster glass* order (Figure 1.4).

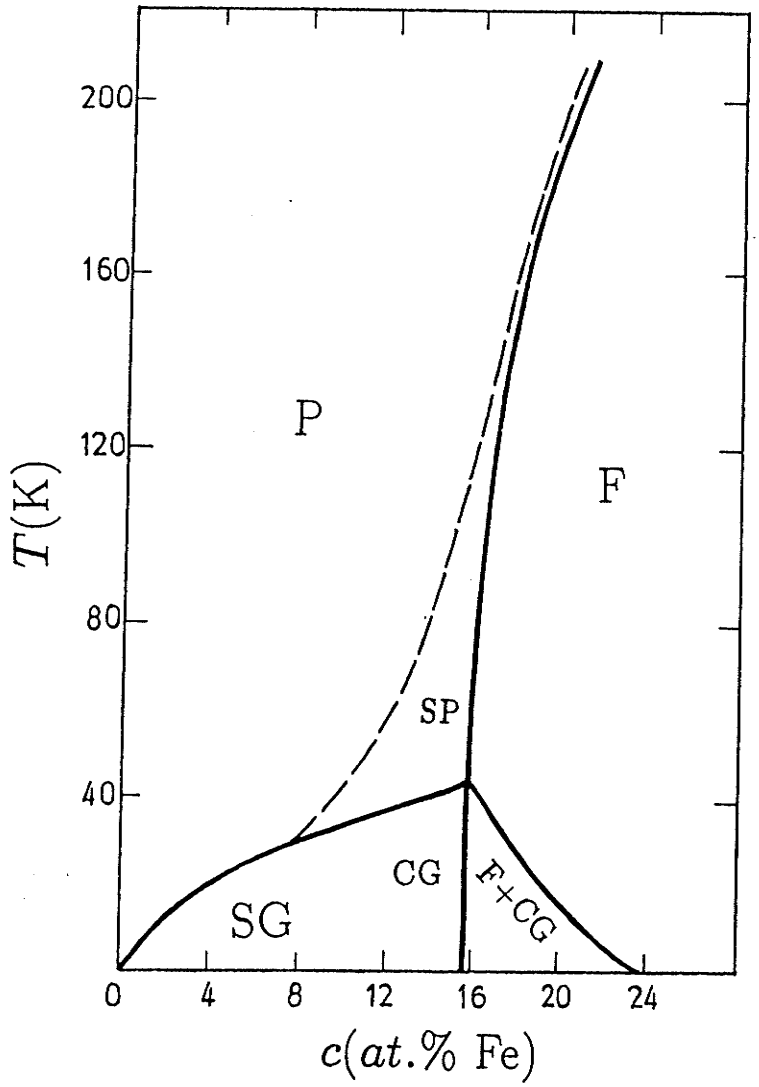

Figure 1.4: The magnetic phase diagram of AuFe. The various regimes are paramagnetic (P), ferromagnetic (F), super-paramagnetic (SP), spin glass (SG), and cluster glass (CG) (after Coles et al., 1978).

Re-entrant Ferromagnets

Alloys with impurity concentrations between those required for a spin glass or a ferromagnetic ground state are predicted, by some mean-field models (particularly the Sherrington-Kirkpatrick model of section 1.2.3), to yield behavior which is a combination of the two. That is, the average separation distance between the magnetic impurities is such that the direct exchange and RKKY interactions are competitive in some way. These systems have the potential to display *re-entrant behavior*, which is defined as a set of sequential transitions, from paramagnetic to ferromagnetic to some sort of spin glass ordering, as the temperature is lowered from above the Curie temperature. For example, **Au**Fe seems to be re-entrant within the concentration range $16 < at.\%\text{Fe} < 24$ (Nieuwenhuys et al., 1979), while the hypothetical range for **Pd**Fe is about $0.01 < at.\%\text{Fe} < 0.10$. Figure 1.3 shows that, within the proposed re-entrant region, the Curie temperature for **Pd**Fe varies as the square of the concentration. Much of the current interest in dilute magnetic alloys is focused on understanding the nature of such systems; moreover, the very existence of the re-entrant spin glass transition is the subject of theoretical and experimental controversy.

Frustration in Alloys with Anti-ferromagnetic Impurities

The concentration dependence of the magnetic order can be complicated further by choosing magnetic impurity atoms (such as Manganese) which couple anti-ferromagnetically through direct exchange. For example, **Pd**Mn is a giant moment ferromagnet ($\sim 7.5\mu_B$ per Mn atom) for Mn concentrations from about 0.1 to 2.5 *at.*% (see Figure 1.5). However, above 5 *at.*% there is a significantly

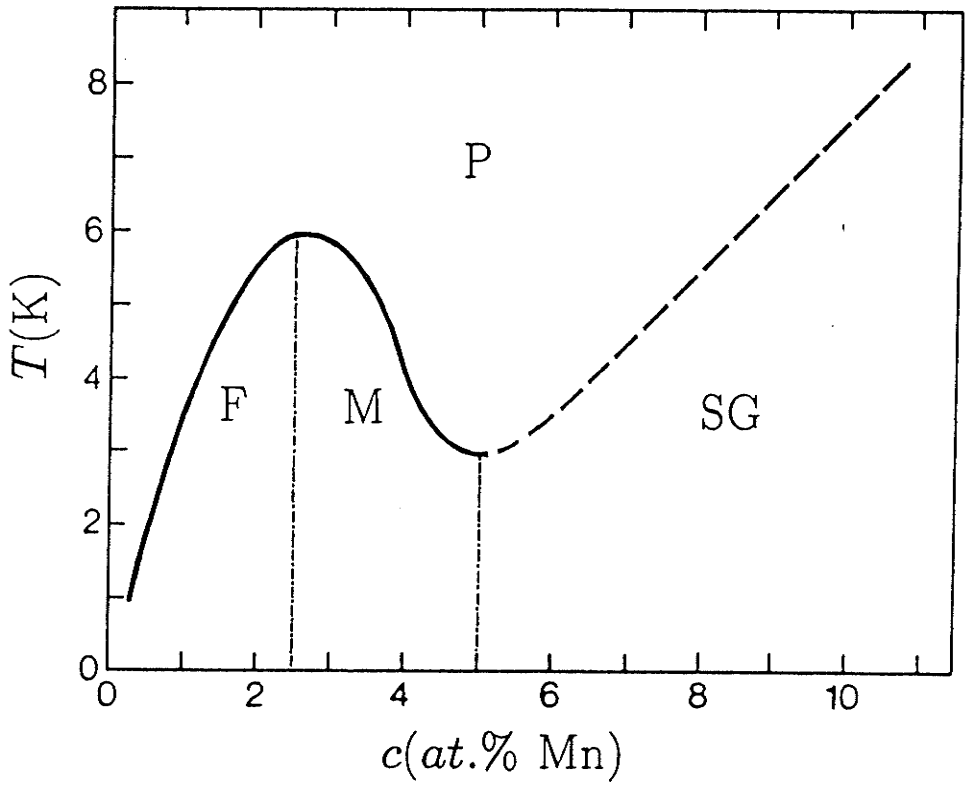

Figure 1.5: The magnetic phase diagram of **Pd**Mn. The bold solid line indicates the Curie temperature, while the bold dashed line indicates the paramagnetic/spin glass transition temperature. The region denoted by M is re-entrant. Not shown are the secondary spin glass and re-entrant regimes at $c < 0.1$ (after Zastre et al., 1985).

increased probability that Mn atoms will be first, second, and third nearest-neighbors, enabling direct anti-ferromagnetic coupling between them. The conflict, between the short-ranged anti-ferromagnetic (Mn-Mn) exchange and the longer-ranged ferromagnetic (giant moment-giant moment) exchange, provides a frustration mechanism which leads to a spin glass ground state. Experiments indicate that more conventional RKKY-induced spin glass ordering is possible below 0.06 *at.*% (Thomson and Thompson, 1979). Hence, two concentration regimes are expected to yield re-entrant behavior in **Pd**Mn; 2.5 to 5 *at.*%, and 0.06 to 0.1 *at.*% (Ho et al., 1981, and Zastre et al., 1985).

1.1.3 Experimental Properties of Very Dilute Alloys

Since the early 1970's there has been a great deal of interest in the study of very dilute magnetic alloys, due largely to the exceptional magnetic behavior of spin glass and (potentially) re-entrant systems. The central question is whether or not the low temperature anomalies, observed in only some of their properties, are due to thermodynamic phase transitions into spin-glass-like states.

Experimentally, spin glasses are characterized by apparently contradictory results for their A.C. susceptibility and specific heat measurments as a function of temperature. There is generally a cusp found in the low field susceptibility at some temperature T_{SG}, perhaps indicating a thermodynamic phase transition from a paramagnetic state to a spin glass state. Seemingly contrary to the Ehrenfest criterion, the specific heat measurements typically show nothing more than a broad maximum with no obvious correlation to T_{SG}. Furthermore, resistivity measurements generally do not reveal clear anomalies as evidence of a sudden phase change at T_{SG}, and the history-dependent effects which spin glass systems possess could be construed as non-equilibrium behavior.

On the other hand, experiments involving neutron diffraction and Mössbauer spectroscopy tend to support the existence of frozen disordered states. Analyses of the spin glass transition within the frame-work of non-linear critical phenomena have also been very successful in recent years (Bouchiat 1986, for example). As a result, the present experimental consensus generally supports the existence of the paramagnetic/spin glass transition, though it is clearly higher than second-order in the Ehrenfest sense, and therefore more subtle than the familiar ferromagnetic transition. (For comprehensive reviews of spin glass properties, see Binder and

Young 1986, and Huang 1985.) The importance of understanding spin glasses is fuelled by the increasingly large number of systems which display spin-glass-like behavior. Initial efforts focused on archetypical systems such as **Au**Fe, though the list has since expanded to include amorphous and insulating systems, for which the frustration mechanisms are somewhat different than in dilute alloys.

During the past decade, similar controversy has developed over ferromagnetic re-entrant systems. They are unique because they show evidence of a high-temperature paramagnetic/ferromagnetic transition, as well as a low-temperature transition from one spontaneously ordered magnetic state to another (i.e., from ferromagnetic to spin glass ordering). However, their analysis is more challenging since ferromagnetic domain wall effects complicate the magnetic behavior for temperatures $T < T_c$. The following sections introduce the salient features of susceptibility measurements on re-entrant systems, as well as dynamical effects in spin glass systems.

Susceptibility Measurements on Re-entrant Systems

As mentioned in section 1.1.2, the magnetic impurity concentration of a dilute alloy is crucial in determining the magnetic ordering of the system. This dependence is indicated most obviously by the temperature dependent low-field A.C. susceptibility. In this respect, the ternary alloy (**Pd**Fe)Mn has been well represented in the literature.

Like **Pd**Mn, (**Pd**Fe)Mn is expected to have concentration regions which yield re-entrant behavior. With a concentration of 0.35 *at.*% Fe, **Pd**Fe is a strong giant-moment ferromagnet with $T_c \approx 8.7\,K$. Adding Mn to the **Pd**Fe matrix

introduces anti-ferromagnetic exchange bonds to the system; hence there is a frustration mechanism that depends on the relative amounts of Fe and Mn (Figure 1.6).

Verbeek et al.(1978) studied $(\mathbf{Pd}_{0.9965}\mathrm{Fe}_{0.0035})_{1-x}\,\mathrm{Mn}_x$ for Mn concentrations of $x = 0.01$, 0.05, and 0.065, and their zero-field susceptibility measurements are shown in Figure 1.7. Curve (a) represents a transition from paramagnetism to ferromagnetism, but the susceptibility has not been corrected for the shape-dependent demagnetizing factor D, which is appreciable since they used spherical samples. (That is, the impurity spins are partially shielded from the applied field H_a by means of a diamagnetic component to the sample magnetization; the resulting effective internal field is $H_i = H_a - DM$, where M is the magnetization component in the direction of H_a.) They attempted to compensate for the effects of D by means of the following relation (after Verbeek et al., 1978):

$$\chi_{true} = \frac{\chi_{measured}}{1 - D\chi_{measured}} \quad . \tag{1.13}$$

At the Curie temperature T_c, χ_{true} diverges to infinity, while $\chi_{measured} = 1/D$. They estimated a value of $T_c \approx 13\,K$ by locating the point on the knee of the curve where $d\,\chi_{measured}/dT$ is a maximum.

Curve (c) displays typical spin glass characteristics, with a sharp cusp observed at the spin glass freezing temperature $T_{SG} \approx 4.7\,K$. The decrease in χ as the temperature is lowered through T_{SG} is symptomatic of the freezing of the impurity moments into random orientations as $T \rightarrow 0$.

Curve (b) potentially shows re-entrant ferromagnetic behavior. As temperature is lowered, a change from paramagnetism to ferromagnetic ordering seems to

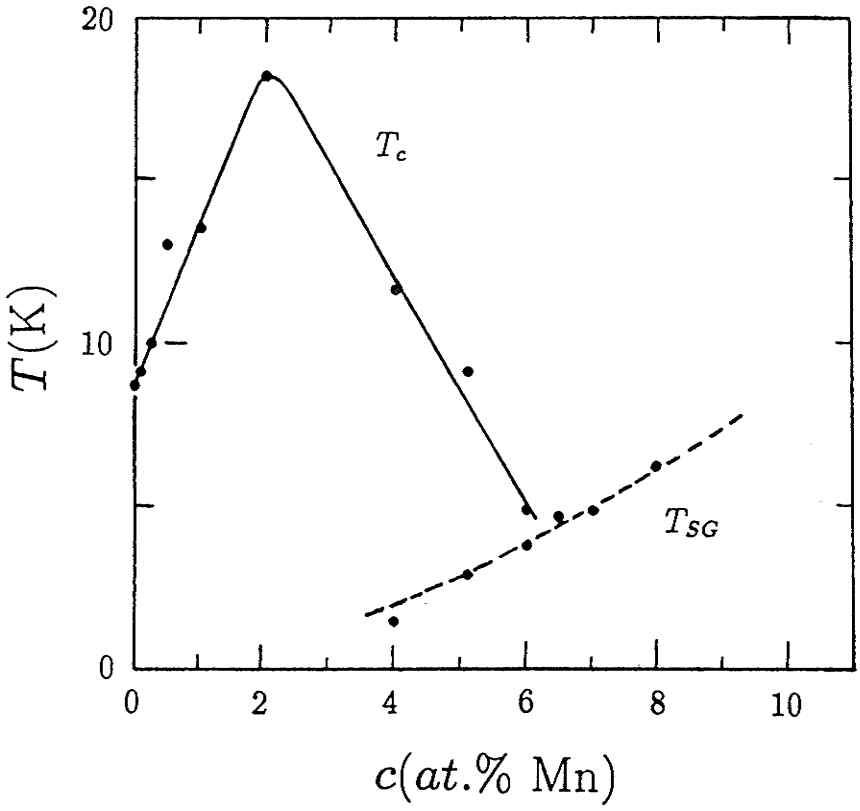

Figure 1.6: The magnetic phase diagram of $(Pd_{0.9965}Fe_{0.0035}) + c$ *at.*% Mn. The region $3 \leq c \leq 6$ is re-entrant (after Huang, 1985).

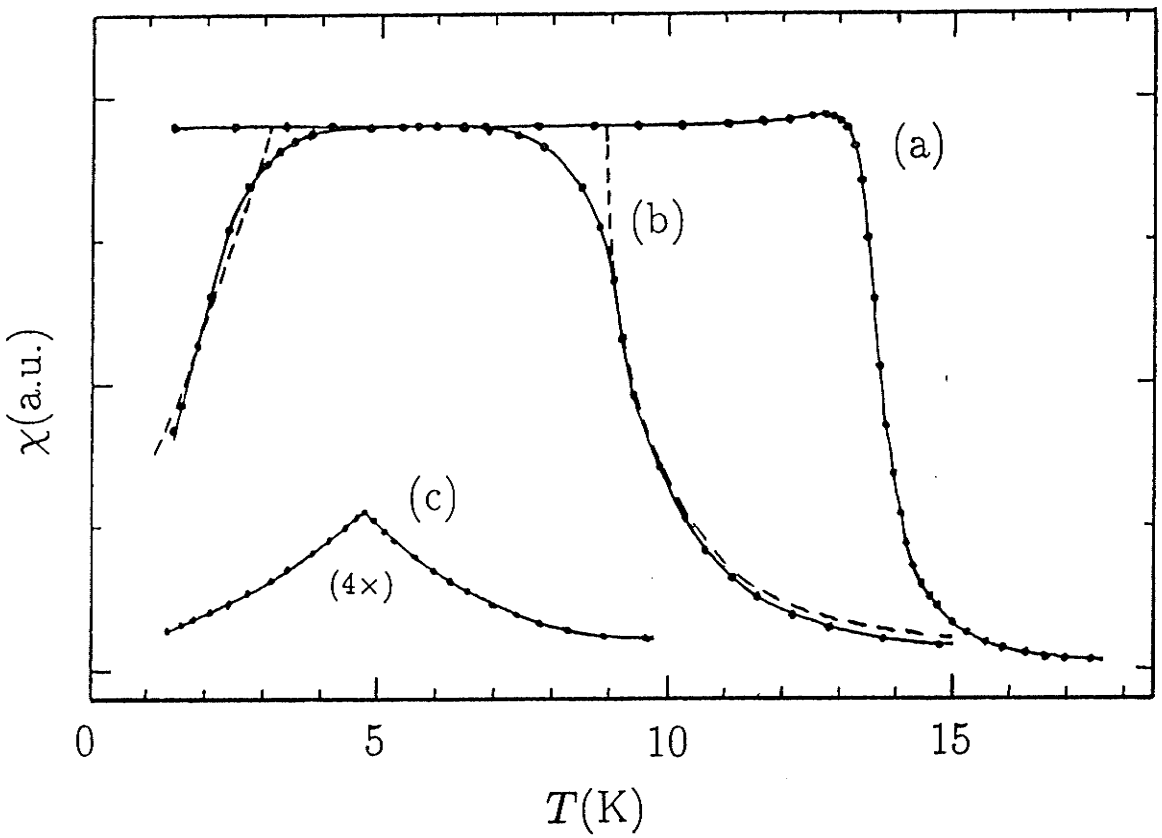

Figure 1.7: Zero-field A.C. susceptibility measurements (using a driving field of 0.1 Gauss and 210 Hz) on several $(\mathbf{Pd}_{0.9965}\mathrm{Fe}_{0.0035}) + c$ *at.*% Mn alloys:
(a) ferromagnet ($c = 6.5$),
(b) re-entrant ($c = 5$),
(c) spin glass ($c = 1$).
The dashed line represents a theoretical re-entrant calculation (from the Sherrington-Kirkpatrick model) which has been artificially demagnetization limited (after Verbeek et al., 1978).

occur at $T_c \approx 9\,K$. Note that the knee is much broader than for curve (a), indicating perhaps that the ferromagnetic ordering is not as well defined in the re-entrant case. The system displays ferromagnetic characteristics down to about $T = 5\,K$, at which point a reversed knee and then a rapid decrease in χ are encountered. Verbeek et al. associated this decrease with the onset of spin glass ordering. They also compared their results with predictions made by the Sherrington-Kirkpatrick model (section 1.2.3), with good qualitative agreement—they did, however, artificially introduce demagnetization limiting to the theoretical susceptibility curve. The similarity is significant because the model predicts the existence of a spin glass/ferromagnetic phase transition. They studied other concentrations as well, and found similar re-entrant-like behavior throughout the concentration range $3 \leq at.\%\ \mathrm{Mn} \leq 6$. For the sake of comparison, Figure 1.8 shows the susceptibility of several **Au**Fe alloys which display spin glass and re-entrant characteristics.

Nieuwenhuys et al. (1978) investigated the effects of applying D.C. biasing fields, along the direction of the A.C. probing field, to (**Pd**Fe)Mn alloys of various Mn concentrations. Figure 1.9(a) shows a typical spin glass case with 8 $at.\%$ Mn. The movement of the cusp to lower temperatures with increasing field is characteristic of spin glass systems, and is also duplicated by the Sherrington-Kirkpatrick solutions.

Figure 1.9(b) shows the possibly re-entrant 5 $at.\%$ Mn case. In a finite biasing field, the susceptibility clearly develops two peaks around the proposed transition temperatures T_{SG} and T_c. While the upper peak moves to higher temperatures as the field is increased, the field dependence of the lower peak is much like that of the paramagnetic/spin glass cusp, thus lending support to

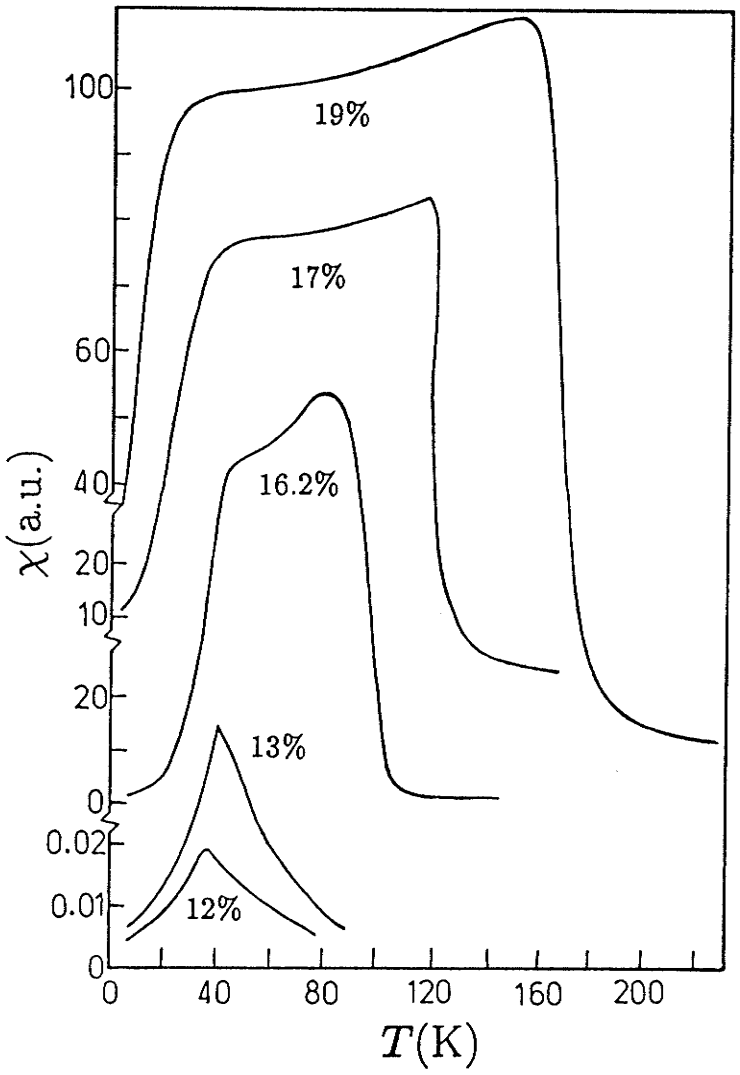

Figure 1.8: Zero-field A.C. susceptibility measurements ($\sim$ 0.5 G, 210 Hz) on AuFe alloys of various Fe concentrations. The 12 *at.*% and 13 *at.*% Fe curves show typical spin glass characteristics, while the remaining curves are re-entrant (after Coles et al., 1978).

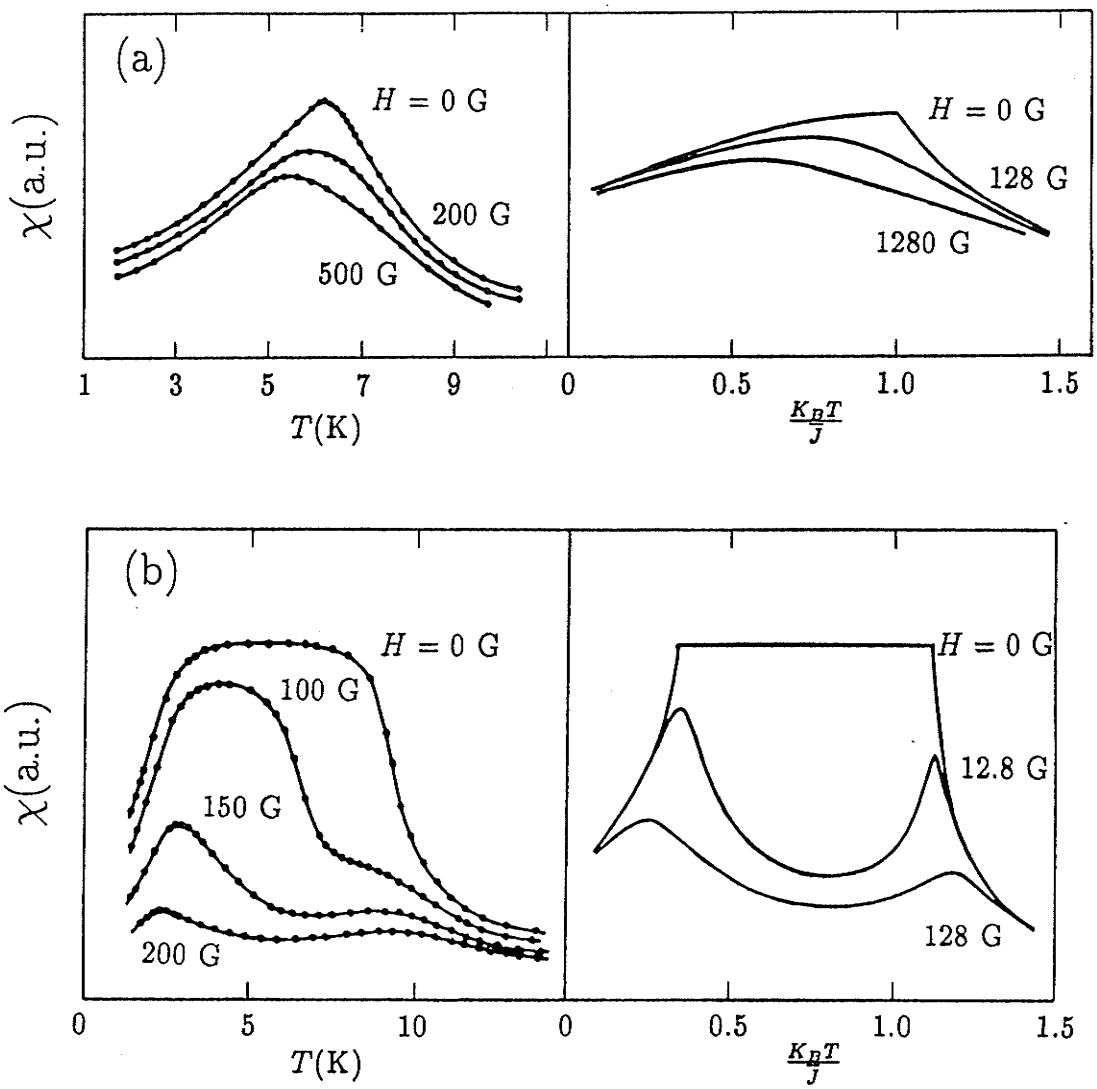

Figure 1.9: In figure (a), the left hand curves represent the A.C. susceptibility of the $(\mathbf{Pd}_{0.9965}\mathrm{Fe}_{0.0035})$ + 8 *at.*% Mn spin glass in various D.C. biasing fields H [Gauss]. The right-hand curves are theoretical calculations based on the Sherrington-Kirkpatrick model. As explained in section 1.2.3, the value of $\overline{J_0}/\overline{J} = 0.5$ used for the calculations places them within the spin glass region of the theoretical phase diagram.

In figure (b), the left-hand curves represent the susceptibility of the $(\mathbf{Pd}_{0.9965}\mathrm{Fe}_{0.0035})$ + 5 *at.*% Mn re-entrant alloy in various biasing fields, while the right-hand curves illustrate theoretical re-entrant calculations with $\overline{J_0}/\overline{J} = 1.1$. As before, the theoretical zero-field curve has been artificially demagnetization limited (after Nieuwenhuys et al., 1978).

the notion of a re-entrant spin glass phase. Nieuwenhuys et al. also compared the field dependence of their re-entrant system to predictions of the Sherrington-Kirkpatrick model, and once again a good qualitative agreement is observed.

Unfortunately, the above qualitative analysis does not preclude the possibility that non-critical ferromagnetic domain wall effects are responsible for the low temperature re-entrant-like behavior. Additionally, the method of obtaining T_c and T_{SG} from the zero-field susceptibility is somewhat questionable, as the positions of the knees are presumably functions of the demagnetizing factor.

Re-entrant Critical Behavior?

More recently, Kunkel and Williams (1988) studied the $(\mathbf{Pd}_{0.9965}\mathrm{Fe}_{0.0035})$ + 5 *at.*% Mn re-entrant system in much greater detail, and attempted to characterize both the upper and lower transitions in terms of linear and non-linear critical phenomena. Their susceptibility measurements were not demagnetization limited, as the geometric shapes of their samples were chosen to minimize such effects. Even so, their temperature-dependent zero-field susceptibility curve displayed an intermediate plateau structure similar to the results of Verbeek et al. (1978). This implies that the plateau is not simply a manifestation of the limits imposed by demagnetization, but is instead an intrinsic property of the experimental system. The formation of magnetic domains between T_{SG} and T_c is conjectured to be the underlying cause.

To investigate critical behavior, Kunkel and Williams carefully measured the effects of applying various D.C. biasing fields, and obtained the typical double-peaked structure for the susceptibility. They analysed the field dependence of the

high temperature peak (centered near $\sim$ 9 K) in terms of the usual ferromagnetic static scaling law (equation 1.11), which can be rewritten in the form

$$\chi(H,t) = H^{(1/\delta)-1}\, G_{\pm}\left(\frac{H}{t^{\gamma+\beta}}\right) \quad , \tag{1.14}$$

where $t = \left|\frac{T-T_c}{T_c}\right|$ is the reduced temperature. Moreover, they were able to extract a self-consistent set of critical parameters such that the exponents satisfy the Widom relationship (equation 1.8). The quality of the corresponding scaling plot (Figure 1.10) illustrates that the upper transition is a well-defined paramagnetic/ferromagnetic phase change.

Characterizing the lower temperature ($\sim$ 4 K) transition within the framework of critical phenomena is more difficult. Solutions of the Sherrington-Kirkpatrick coupled equations (1.51 and 1.52) obtained analytically through expansions of the Brillouin function, indicate that the critical behavior at the *direct* paramagnetic/spin glass transition is apparent only in the non-linear susceptibility (Yeung et al. 1987, Roshko et al. 1985). In other words, the theory predicts a linear susceptibility which is finite and continuous for all temperatures (including T_{SG}). Since the non-linear magnetic response is typically much weaker than the linear response, the corresponding critical behavior is not easy to observe experimentally. Even so, several experimental investigations have apparently been successful in critically scaling spin glass data in terms of the theoretical predictions (Bouchiat 1986, and Yeung 1988, for instance). The appropriate scaling equation shares the same basic form as equation 1.11. However, as the scaling function must be an even function of the field H (otherwise the corresponding

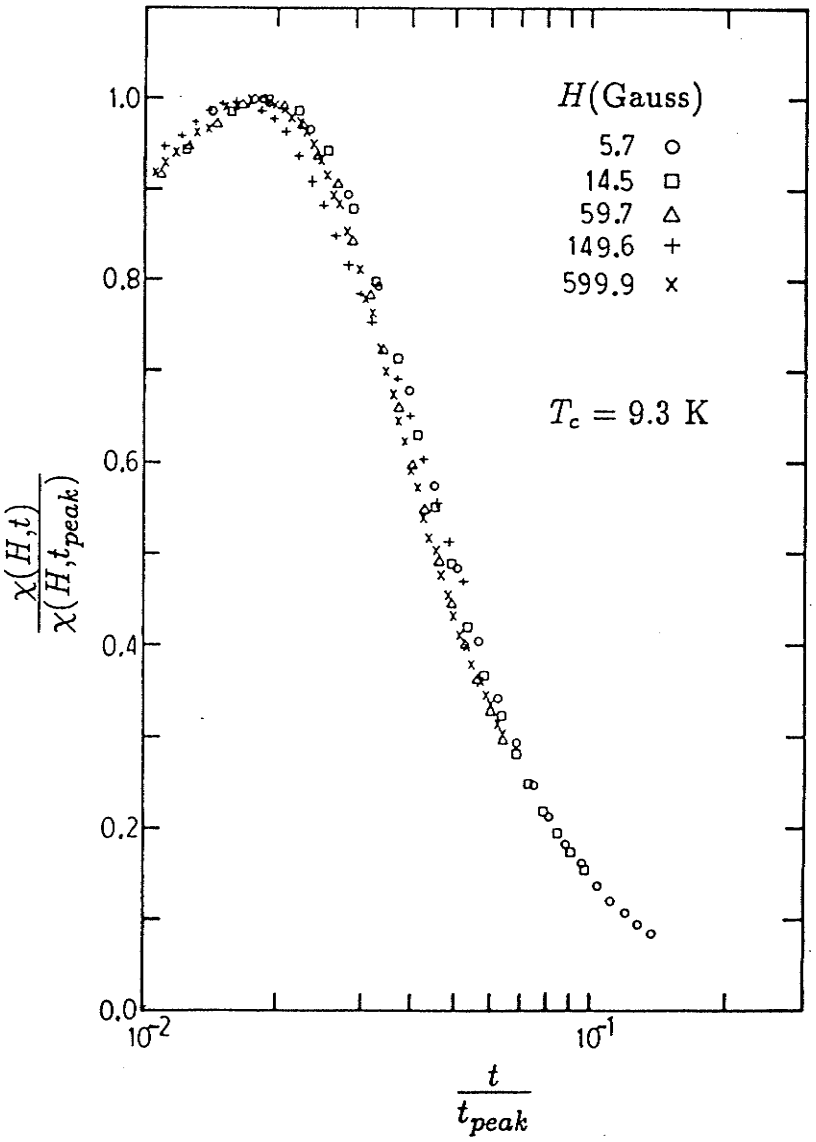

Figure 1.10: A scaling plot for the potentially re-entrant $(\mathbf{Pd}_{0.9965}\mathrm{Fe}_{0.0035})$ + 5 *at.*% Mn system. Various internal fields are indicated, and the temperatures all lie above 9.3 K. The reduced temperature t_{peak} represents the location of the high temperature peak in $\chi(t)$ for a particular field. The quality of the scaling illustrates that a well defined paramagnetic/ferromagnetic transition occurs at $T_c = 9.3$ K (after Kunkel et al., 1988).

magnetic response would contain diamagnetic components), it can be expanded as (Kunkel et al. 1988)

$$\begin{aligned} \chi(H,t) &= \chi(0,t) - t^{-\gamma'} G_{\pm}\left(\frac{H^2}{t^{2\gamma'+2\beta'}}\right) \\ &= \chi(0,t) - a_2(t)\,H^2 + a_4(t)\,H^4 - \cdots \quad . \end{aligned} \tag{1.15}$$

The primes are used to distinguish the spin glass critical exponents from those of the ferromagnetic case, and the reduced temperature is redefined as $t = \left|\frac{T-T_{SG}}{T_{SG}}\right|$.

In analogy to the spin glass studies, Kunkel and Williams used their data from around the lower transition to check for a divergence in the coefficient $a_2(t)$ of the leading non-linear term. (As an aside, it should be noted that valid expansions of the aforementioned coupled equations are not possible to perform within the re-entrant region, and hence no critical predictions for the re-entrant transition can be derived analytically. However, the detailed numerical solutions explored in Chapter 3 of this thesis do verify that the non-linear critical behavior theoretically extends to the re-entrant transition as well.) In particular, they plotted $\chi(H,t)$ versus H^2 for temperatures both above and below their final choice of T_{SG}. At low fields these plots are linear since the H^2 term dominates the expansion. Hence, the initial slopes of the isotherms yield the the values of the coefficient at each temperature. These are plotted versus temperature in Figure 1.11. Though not divergent, the distinct anomaly at 4.07 K is highly suggestive of a phase transition, and Kunkel and Williams used it to identify T_{SG}. The lack of a divergence could be due partly to an underestimate of the coefficient values for temperatures near T_{SG}. As $t \rightarrow 0$, the initial linear portions of the isotherms (in the χ versus

H^2 plots) become confined to lower and lower fields, and it is experimentally difficult to ensure that the measured data represent the true initial slope. Kunkel and Williams also propose that dynamical effects, related to the onset of critical slowing down as $T \rightarrow T_{SG}$, together with the use of a probing field of finite (as opposed to zero) frequency, are to blame. Nevertheless, their analysis shows intriguing evidence of critical re-entrant behavior.

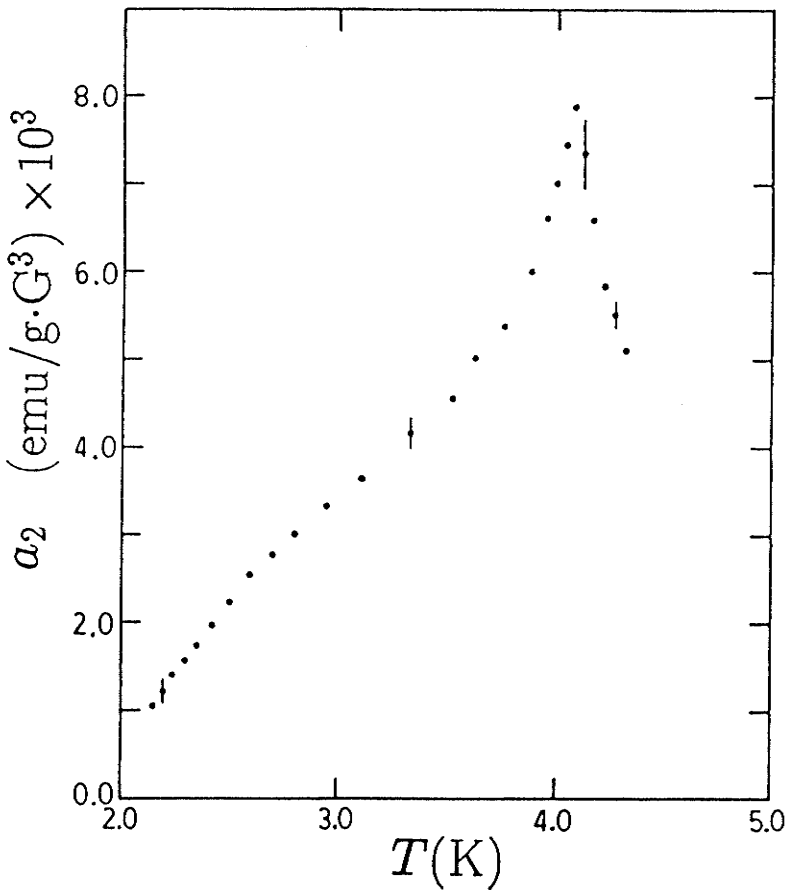

Figure 1.11: A peak in the quadratic field coefficient of the $(\mathbf{Pd}_{0.9965}\mathrm{Fe}_{0.0035}) + 5$ *at.*% Mn susceptibility apparently occurs near 4.07 K. The anomaly is suggestive of critical re-entrant behavior, and is used to identify the re-entrant transition temperature T_{SG} (after Kunkel et al., 1988).

Dynamical and History-Dependent Properties of Spin Glasses

Spin glasses have unique dynamical and history dependent properties which characteristically set in near the paramagnetic/spin glass transition temperature T_{SG}. These are manifest in many ways, such as the differences between *field-cooled* (FC) and *zero-field-cooled* (ZFC) magnetization measurements (as a function of temperature). The ZFC magnetization curve is obtained by cooling the spin glass specimen in zero applied field, from a temperature $T > T_{SG}$ to the lowest desired measuring temperature $T_m < T_{SG}$, at which point a small D.C. field H is applied. Similarly, the FC magnetization is obtained by cooling in the specimen down to $T_m < T_{SG}$ in the same finite field used above. In both cases, successive measurements are obtained by incrementing the temperature and stabilizing at each of the desired T_m values, until the highest required temperature is reached.

As shown in Figure 1.12, the FC and ZFC curves are identical down to some well defined temperature, below which their behavior differs dramatically. Experimentalists often identify this point of departure with T_{SG}, and we shall adopt this approach. The FC curve is roughly temperature independent below T_{SG}, while the ZFC shows a cusp at T_{SG}. Significantly, below T_{SG} the ZFC magnetization slowly relaxes (quasi-logarithmically) with time towards the FC state, which it is expected to reach as time $t \rightarrow \infty$. On the other hand, only extremely weak time effects have been observed for the FC case (Lundgren et al., 1982). Note that the ZFC magnetization is similar in nature to low frequency A.C. susceptibility measurements, though the time effects in the A.C. case appear also as a frequency dependence of the cusp.

As shown in Figure 1.13 the ZFC and FC curves for re-entrant systems

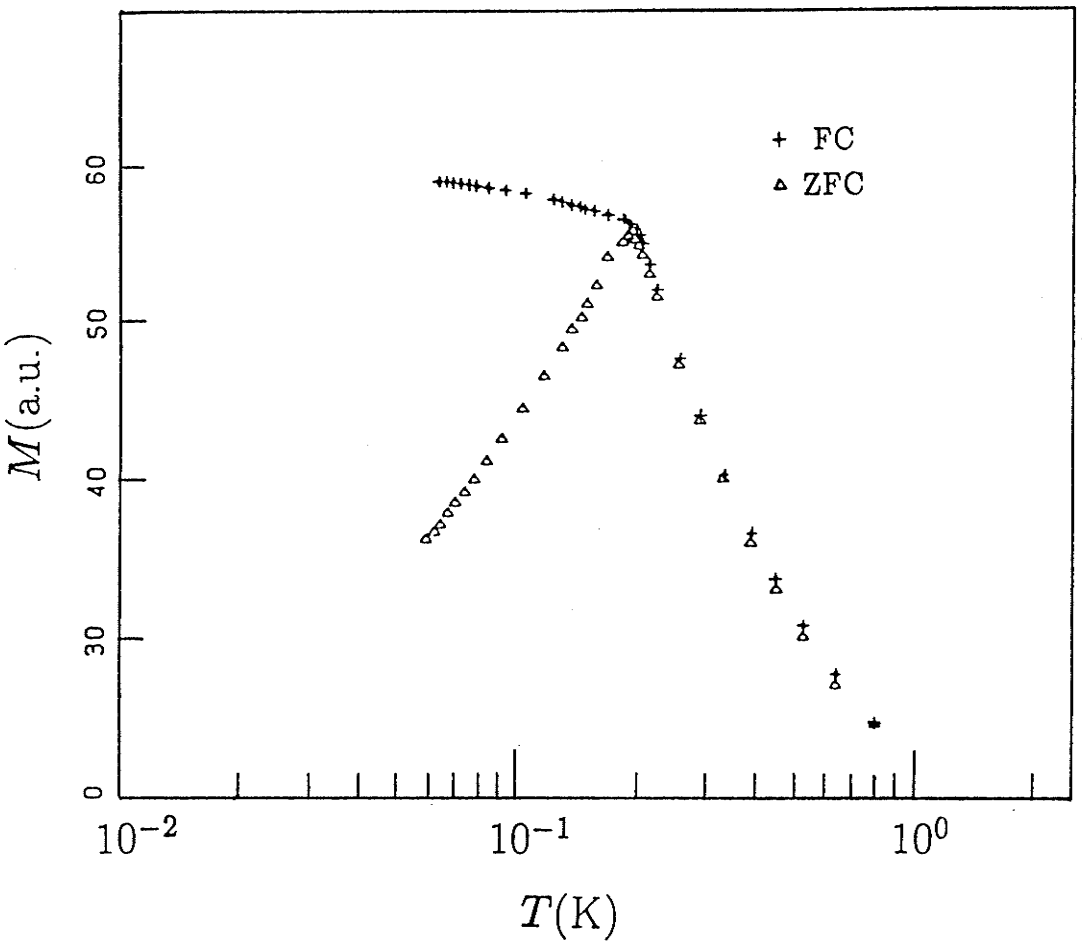

Figure 1.12: The FC and ZFC magnetization of the **Pt** + 2400 ppm Mn spin glass, using an applied field of 2 Gauss. The peak in the ZFC curve is associated with $T_{SG} \approx 200$ mK (after Yeung, 1988).

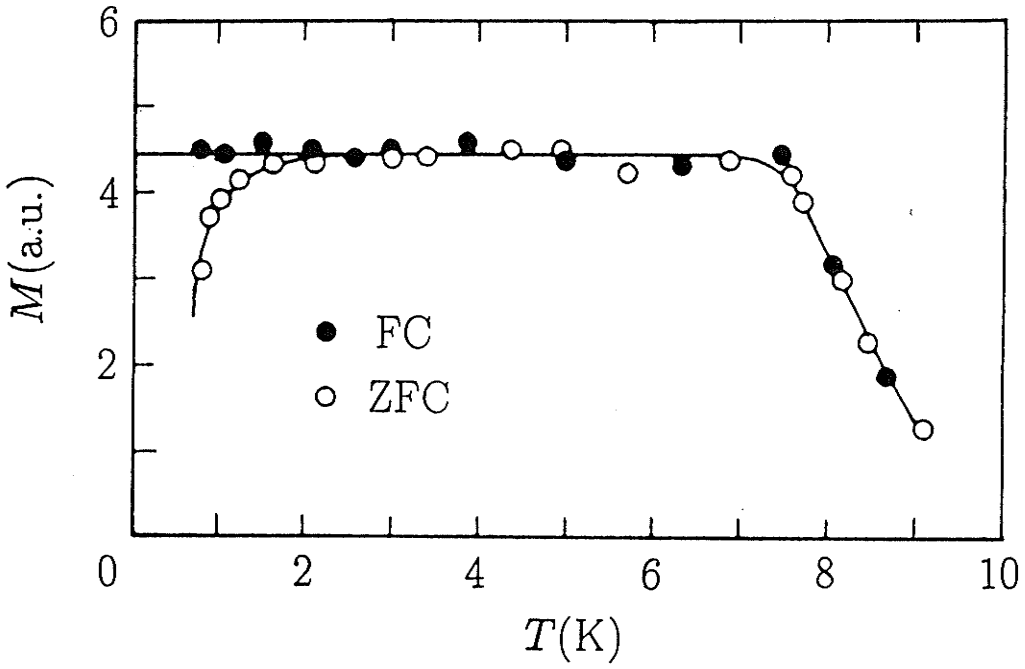

Figure 1.13: The FC and ZFC magnetization curves for the $(\mathbf{Pd}_{0.9965}\mathrm{Fe}_{0.0035})$ + 5 *at.*% Mn re-entrant system, using an applied field of 0.1 Gauss (after Carnegie et al., 1979).

display features similar to those found for spin glasses. However, analysis is hindered by time effects (induced by ferromagnetic domain wall motion) which occur in the ZFC curve below the Curie temperature. These tend to obscure the (possible) lower temperature transition into the spin glass state. For this reason, the remainder of this discussion deals with the simpler dynamics of typical spin glass systems.

Upon zero-field-cooling a spin glass to a temperature $T_m < T_{SG}$, one might intuitively expect the system to quickly reach equilibrium if no field is ever applied. Lundgren et al. (1983) studied a **Cu**Mn spin glass ($T_{SG} = 26K$) for fixed H and T_m. They found that the rate of relaxation is a function of the time t_w that one waits at constant T_m before the field H is turned on. Hence, the ZFC state must evolve over time, even without the influence of an external field.

Analogous behavior occurs after cooling to T_m in a field, and then turning the field off after a time t_w has elapsed since passing through T_{SG}. This is called the *thermo-remanent magnetization* (σ_{trm}). Chamberlin (1984, 1985) studied several **Ag**Mn and **Cu**Mn spin glasses and determined that σ_{trm} is a function of t_w. Thus, even the FC state cannot be in equilibrium (at least over finite observation times). Moreover, he found that for all $T_m < T_{SG}$, σ_{trm} relaxes with time ($5 < t[\text{seconds}] < 10^3$) according to a *stretched-exponential* function (Chamberlin, 1985)

$$\sigma_{trm} = \sigma_0 \exp\left[-\left(\frac{t}{\tau_p}\right)^{1-n}\right] \quad . \tag{1.16}$$

The exponent n and prefactor σ_0 are functions of T_m, where $n < 1$. Hoogerbeets et al. (1985,1986) also discovered a temperature dependence for the relaxation rate

such that $\tau_p \simeq 10^3 \exp\left[\frac{2.5 T_{SG}}{T_m}\right]$ seconds. In addition, τ_p increases exponentially with the wait time t_w. Figure 1.14 illustrates the appropriate log-log plot required to yield a straight-line with slope $-n$. The deviations for times $t < 5$ seconds were attributed to eddy-current effects and ignored.

Hoogerbeets et al. (1986) attempted to show that the stretched-exponential relaxation is an intrinsic property of a spin glass perturbed from equilibrium. Their argument was based on comparisons to a dynamical mean-field Ising model which predicts that many different thermodynamic equilibrium states (each with a different configuration of randomly-oriented, frozen spins) are available to the system below T_{SG}. The stability of each state is a function of applied field and T_m. Some of the states are more stable than others and upon changing the field, the system will relax from state to state until (as $t \rightarrow \infty$) it reaches true equilibrium in the most stable configuration. Remarkably, the relaxation is predicted to follow a stretched-exponential dependence. Hoogerbeets et al. argued that this agreement between theory and experiment is significant.

The above comparison is controversial, and Nordblad et al. (1986) allege that the stretched-exponential form is not an intrinsic property of the spin glass state. They looked at σ_{trm} over a wide range of times ($1 < t[\text{seconds}] < 10^4$) and discovered that the quality of the stretched-exponential fit is misleading, and adequate only in the interval $5 < t[\text{seconds}] < 10^3$. The deviations for $t < 5$ seconds, which Chamberlin had discarded on the basis of eddy-current effects, were considered by Nordblad et al. to be real.

They proposed that the spin glass equilibrium state is dynamic in nature, and characterized by a purely logarithmic relaxation. Figure 1.15 shows plots of

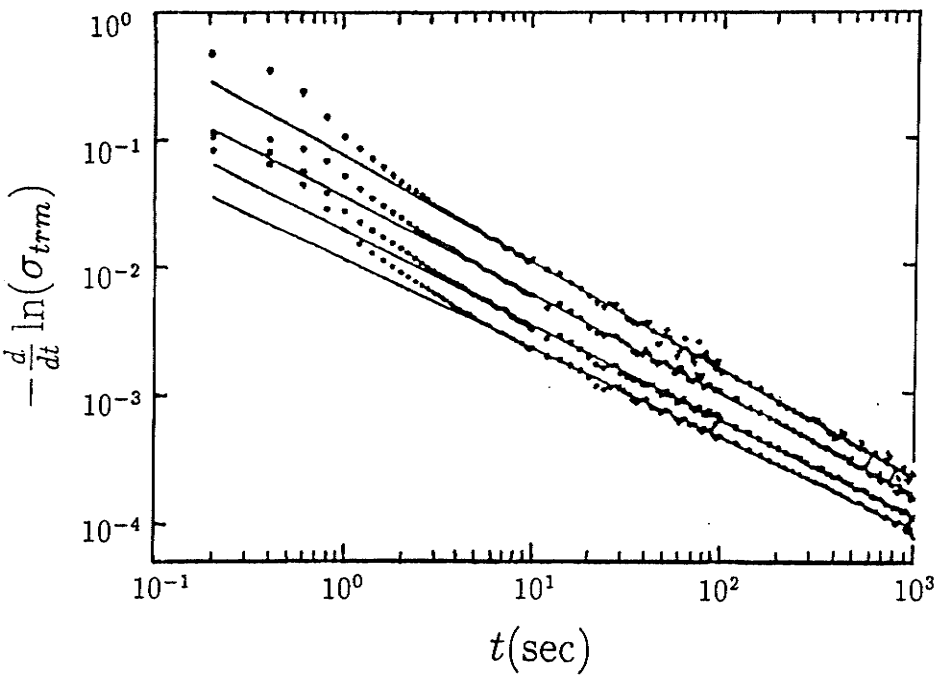

Figure 1.14: Several stretched-exponential fits to the σ_{trm} decay of the (Ag+2.6 *at.*% Mn) + 0.46 *at.*% Sb spin glass system are shown. From top to bottom, the dotted lines represent temperatures of T/T_{SG}=0.966, 0.897, 0.856, and 0.771. The straight lines indicate best fits to the experimental data, while their slopes equal the exponent $-n$ (after Chamberlin, 1985).

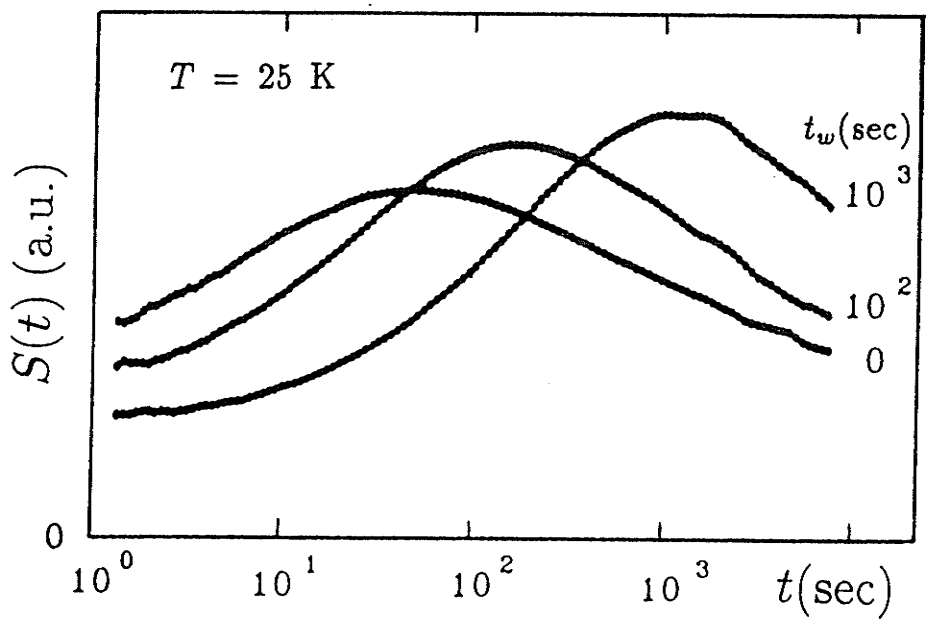

Figure 1.15: A plot of the relaxation rate $S(t) = \frac{1}{H}\frac{\partial \sigma_{irm}}{\partial \ln t}$ for the Cu + 5 *at.*% Mn spin glass (T_{SG} = 28K). There is clearly deviation from logarithmic decay, and the wait time t_w is apparently related to the location of the peak in each curve (after Nordblad et al., 1986).

the total relaxation rate, $S(t) = \frac{1}{H}\frac{\partial \sigma_{trm}}{\partial \ln(t)}$, for fixed temperature $T_m < T_{SG}$ and various wait times t_w. Clearly there is deviation from logarithmic decay, especially at times $t \simeq t_w$. In explanation, they introduced a time-dependent *aging* of the spin glass state, which is superimposed upon the logarithmic relaxation and follows a stretched-exponential form. There exists recent theoretical evidence (Lundgren, 1988) that the aging effect could be related to the growth of spin glass domains, within which the spins are in dynamic equilibrium. Therefore, the total relaxation is described by (Nordblad et al., 1986)

$$\sigma_{trm} = \sigma_0 + \sigma_{equil} H \ln(t) + \sigma_{age}(t_w) \exp\left[-\left(\frac{t}{t_w}\right)^{1-n}\right] \quad , \qquad (1.17)$$

where $\sigma_0 = S(t = 1\text{sec})$, σ_{equil} is the relaxation rate at dynamic equilibrium, and the last term characterizes the influence of aging. Figure 1.16 shows a plot of σ_{trm} versus t. Indeed, the aging scheme fits the data over a wider range of times than the stretched-exponential alone.

Hypothetically, the relaxation of a re-entrant system might be expected to follow a form similar to equation 1.16 or 1.17, but with an additional term to represent the effects of ferromagnetic domain wall motion. In any case, the stretched exponential relaxation may provide a means of identifying magnetic systems which have some degree of spin glass ordering.

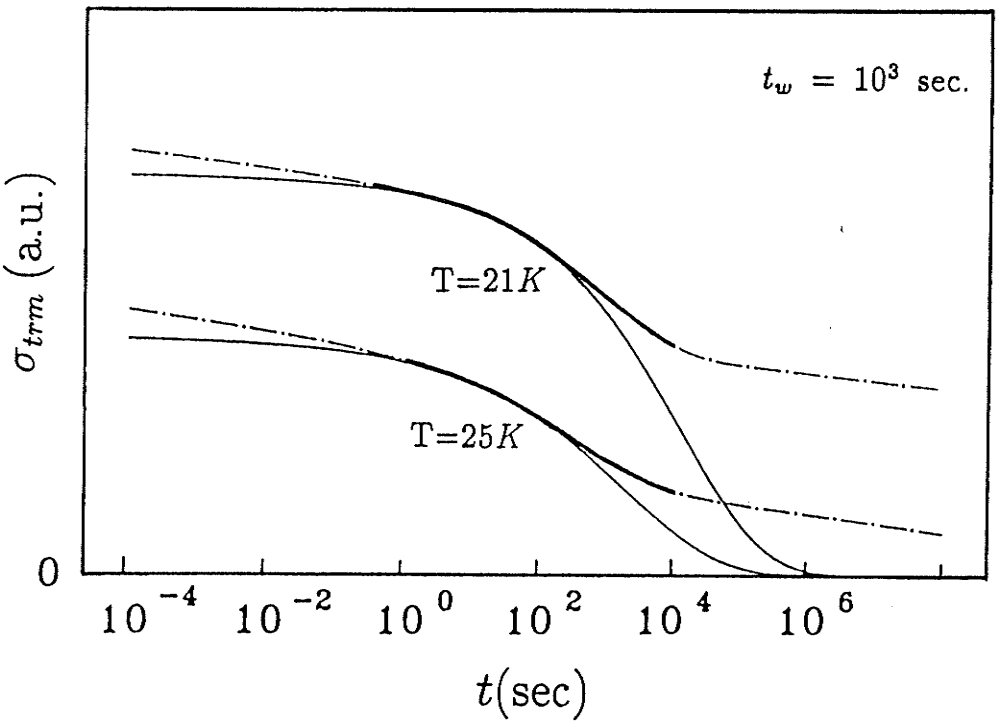

Figure 1.16: A typical comparison between the σ_{trm} decay of the Cu + 5 *at.*% Mn spin glass (bold line), the aging scheme(dashed line) and the stretched-exponential function (thin line). The aging scheme provides the superior functional description (after Nordblad et al., 1986).

1.2 Models of Disordered Magnets

1.2.1 The RKKY Indirect Exchange Interaction

The RKKY (Ruderman, Kittel, Kasuya, Yosida) interaction is an indirect exchange mechanism which provides long-ranged coupling between the magnetic atoms in very dilute alloys, through intermediate interactions with the host's conduction electrons. The interaction oscillates spatially and, when combined with quenched disorder, may cause frustration of the spin orientations and spin glass ordering. The following is a derivation of the RKKY functional form, based on White (1970) and Kittel (1968).

Consider a magnetization $\vec{M}(\vec{r})$ and a static magnetic field $\vec{H}(\vec{r})$. We can write these spatial functions in terms of Fourier series as follows (after White, 1970):

$$\vec{M}(\vec{r}) = \frac{1}{V}\sum_{\vec{k}} \vec{M}\left(\vec{k}\right) e^{i\vec{k}\cdot\vec{r}} \quad , \tag{1.18}$$

$$\vec{H}(\vec{r}) = \frac{1}{V}\sum_{\vec{q}} \vec{H}(\vec{q})\, e^{i\vec{q}\cdot\vec{r}} \quad , \tag{1.19}$$

where $\vec{k}$ and $\vec{q}$ are wavevectors, $\vec{M}\left(\vec{k}\right)$ and $\vec{H}(\vec{q})$ are Fourier components, and the volume of the specimen is V. The response of the magnetization to the magnetic field is given by a general susceptibility χ such that (after White, 1970)

$$\vec{M}\left(\vec{k}\right) = \sum_{\vec{q}} \chi\left(\vec{k},\vec{q}\right)\vec{H}(\vec{q}) \quad . \tag{1.20}$$

By substituting equation 1.20 into equation 1.18 and introducing the identity

$$1 = \frac{1}{V} \int_V d\vec{r'}\, e^{i\vec{q}\cdot\left(\vec{r'}-\vec{r'}\right)}\, e^{i\vec{k}\cdot\left(\vec{r'}-\vec{r'}\right)} \quad ,$$

we get

$$\vec{M}\left(\vec{r}\right) = \frac{1}{V^2} \int_V d\vec{r'} \left\{ \sum_{\vec{k}} \sum_{\vec{q}} \chi\left(\vec{k},\vec{q}\right) \vec{H}\left(\vec{q}\right)\, e^{i\vec{k}\cdot\left(\vec{r}-\vec{r'}\right)}\, e^{i\left(\vec{k}-\vec{q}\right)\cdot\vec{r'}}\, e^{i\vec{q}\cdot\vec{r'}} \right\} \quad .$$

Furthermore, assuming that the susceptibility is translationally invariant (implying $\vec{q} = \vec{k}$ and $\chi\left(\vec{k},\vec{q}\right) \rightarrow \chi\left(\vec{q}\right)$) and independent of the field, it follows that (after Kittel, 1968)

$$\vec{M}\left(\vec{r}\right) = \int_V d\vec{r'}\, \chi\left(\vec{r}-\vec{r'}\right) \vec{H}\left(\vec{r'}\right) \quad , \tag{1.21}$$

where

$$\chi\left(\vec{r}-\vec{r'}\right) = \frac{1}{V} \sum_{\vec{q}} \chi\left(\vec{q}\right)\, e^{i\vec{q}\cdot\left(\vec{r}-\vec{r'}\right)} \quad .$$

Equation 1.21 can also be written in terms of Fourier components:

$$\vec{M}\left(\vec{r}\right) = \frac{1}{V} \sum_{\vec{q}} \chi\left(\vec{q}\right) \vec{H}\left(\vec{q}\right) e^{i\vec{q}\cdot\vec{r}} \quad , \tag{1.22}$$

with

$$\vec{M}\left(\vec{q}\right) = \chi\left(\vec{q}\right) \vec{H}\left(\vec{q}\right) \quad .$$

Of course, the susceptibility depends on the nature of the specimen, and the form

of the applied magnetic field must be known to determine the magnetic response of the system.

To evaluate the functional form of the RKKY interaction, the response of a sea of conduction electrons to the presence of a single magnetic impurity atom (which is immersed in the sea) is determined. The simplest approximation is to use a free electron gas at a temperature of absolute zero. However, to describe the conduction electrons within the narrow $d-$bands of exchange-enhanced hosts such as Palladium or Platinum, it is necessary to include the effects of exchange interactions between the electrons. We shall only consider the former case in detail, since the basic oscillating properties are common to both schemes, though the latter develops giant moments about the impurity atoms.

The first step is to find the susceptibility of the free electron gas. This is related to the change in energy caused by the application of an arbitrary, *non-uniform* field $\vec{H}(\vec{q})\cos(\vec{q}\cdot\vec{r}_i)$. The appropriate Hamiltonian (including kinetic energy) is

$$\mathcal{H} = \sum_i \frac{p_i^2}{2m_e} + \Delta\mathcal{H} \quad , \tag{1.23}$$

where

$$\Delta\mathcal{H} = g\mu_B \sum_i \vec{\sigma}_i \cdot \vec{H}(\vec{q})\cos(\vec{q}\cdot\vec{r}_i)$$

is the perturbation Hamiltonian due to the field. To avoid redistribution of electrons between spin-up and spin-down states, the field is applied perpendicular to the direction of quantization. In particular, $\vec{H}(\vec{q}) = H(\vec{q})\,\hat{x}$ so that (after Kittel,

1968)

$$\vec{\sigma}_i \cdot \vec{H}(\vec{q}) = H(\vec{q}) \left(\frac{\sigma_i^+ + \sigma_i^-}{2} \right) \quad ,$$

and

$$\Delta\mathcal{H} = \frac{1}{4} g\mu_B H(\vec{q}) \sum_i \left(\sigma_i^+ + \sigma_i^- \right) \left(e^{i\vec{q}\cdot\vec{r}_i} + e^{-i\vec{q}\cdot\vec{r}_i} \right) \quad .$$

The unperturbed free electron eigenstates with energy $E_{\vec{k}}$ are denoted as $\left|\vec{k},\sigma\right\rangle = \left|\vec{k}\right\rangle|\sigma\rangle$, where $|\sigma\rangle = |\uparrow\rangle$ is spin up and $|\sigma\rangle = |\downarrow\rangle$ is spin down. Kittel used perturbation theory, along with the identities

$$\left\langle \vec{k}' \right| e^{\pm i\vec{q}\cdot\vec{r}_i} \left| \vec{k} \right\rangle = V\Delta_{\vec{k}',\vec{k}\pm\vec{q}}$$

$$\text{and} \qquad \langle\downarrow|\sigma^-|\uparrow\rangle\langle\uparrow|\sigma^+|\downarrow\rangle = 4$$

to obtain the total second-order energy correction

$$\Delta E = -\frac{1}{4}\left[g\mu_B H(\vec{q})\right]^2 \sum_{\vec{k}} \frac{\eta_{\vec{k}} - \eta_{\vec{k}+\vec{q}}}{E_{\vec{k}+\vec{q}} - E_{\vec{k}}} \quad .$$

The Fermi-Dirac function,

$$\eta_{\vec{k}} = \left\{ \exp\left[\frac{E_{\vec{k}} - E_F}{k_B T} \right] + 1 \right\}^{-1} \quad ,$$

is the probability that the state $\left|\vec{k}\right\rangle$ is occupied (at absolute zero), and E_F is the Fermi energy.

The electron gas susceptibility is given by (after Kittel, 1968)

$$\chi(\vec{q}) = -2\frac{\partial^2(\Delta E)}{(\partial H(\vec{q}))^2} = g^2\mu_B^2 \sum_{\vec{k}} \frac{\eta_{\vec{k}} - \eta_{\vec{k}+\vec{q}}}{E_{\vec{k}+\vec{q}} - E_{\vec{k}}} \quad .$$

By converting the sum to an integration, it can be shown that (after Kittel, 1968)

$$\chi(\vec{q}) = \frac{1}{4}\left[\frac{3Ng^2\mu_B^2}{2E_F}\right]\left\{\frac{1}{2} + \left(\frac{4k_F^2 - q^2}{8k_F q}\right)\log\left|\frac{2k_F + q}{2k_F - q}\right|\right\} \quad , \qquad (1.24)$$

where N is the number of electrons per unit volume, $E_F = \frac{\hbar^2 k_F^2}{2m_e}$, and the factor inside the brackets [ ] is the Pauli paramagnetic susceptibility for a uniform field.

The next step is to represent the field produced by the magnetic impurity atom. Assuming that the impurity spin is localized, then the Heisenberg exchange Hamiltonian (after White, 1970)

$$-J\sum_i \vec{S_\alpha} \cdot \vec{\sigma_i}\,\delta(\vec{r_i}) \qquad (1.25)$$

describes the interaction between the conduction electron spins $\vec{\sigma_i}$ (located at $\vec{r_i}$) and the impurity spin $\vec{S_\alpha}$ (located at $r = 0$). The exchange parameter J describes the strengh of the interaction. We can rewrite equation 1.25 in the form

$$g\mu_B \sum_i \vec{H}(\vec{r_i}) \cdot \vec{\sigma_i} \quad .$$

Hence, due to the impurity atom, each electron is subject to an effective field

(after White, 1970)

$$\vec{H}(\vec{r_i}) = -\frac{J}{g\mu_B}\vec{S_\alpha}\,\delta(\vec{r_i}) \quad ,$$

with a Fourier transform of

$$\vec{H}(\vec{q}) = -\frac{J}{g\mu_B}\vec{S_\alpha} \quad . \qquad (1.26)$$

Substituting equations 1.24 and 1.26 into 1.22 gives the electron polarization $\vec{M}$ as a function of the distance r from the impurity atom. After converting the sum to an integral, it can be shown that (after White, 1970)

$$\vec{M}(r) = \left(-\frac{JNg\mu_B}{E_F k_F \pi}\right)\left(\frac{3}{128}\right)\left\{\frac{\sin 2k_F r - 2k_F r\cos 2k_F r}{r^4}\right\}\vec{S_\alpha} \quad .$$

This, in turn, plays the part of an effective-field acting on another magnetic atom with spin $\vec{S_\beta}$. The Heisenberg exchange interaction between spins $\vec{S_\alpha}$ and $\vec{S_\beta}$ (separated by distance r) is

$$\mathcal{H}_{RKKY} = -J_{RKKY}\,\vec{S_\alpha}\cdot\vec{S_\beta} \quad , \qquad (1.27)$$

where

$$J_{RKKY} = \frac{J^2 N}{E_F k_F \pi}\left(\frac{3}{128}\right)\left\{\frac{\sin 2k_F r - 2k_F r\cos 2k_F r}{r^4}\right\} \quad . \qquad (1.28)$$

The expression in braces { } is plotted in Figure 1.17, curve (a). Note the divergence as $r \to 0$. For larger separations, the interaction oscillates as a cosine with an r^{-3} envelope. It is the superpositioning of the many such interactions, between

all the magnetic impurities in a dilute alloy, which ultimately can lead to frustration effects and spin glass behavior. Since exchange interactions between the conduction electrons (of the host metal) have been ignored in the above derivation, it is only valid for non-exchange-enhanced hosts such as Gold or Copper.

For hosts such as Palladium or Platinum, the conduction d-band is quite narrow so that the effects of direct exchange interactions must be included. They may be estimated by replacing equation 1.24 with an enhanced susceptibility of the form (after Foner, 1976)

$$\chi_{enhanced}(\vec{q}) = \frac{\chi(\vec{q})}{1 - I\chi(\vec{q})} \quad .$$

The denominator is the Stoner enhancement factor, where I represents the strength of the conduction electron exchange interactions, and is generally a function of $\vec{q}$. In Pd, the susceptibility is enhanced by roughly an order of magnitude, and tends to suppress the positive-negative oscillations of the RKKY interaction out to $r \sim 10\mathring{A}$ (—see curve (b)). In other words, a large polarization cloud develops around each magnetic impurity, outside of which the RKKY oscillations resume.

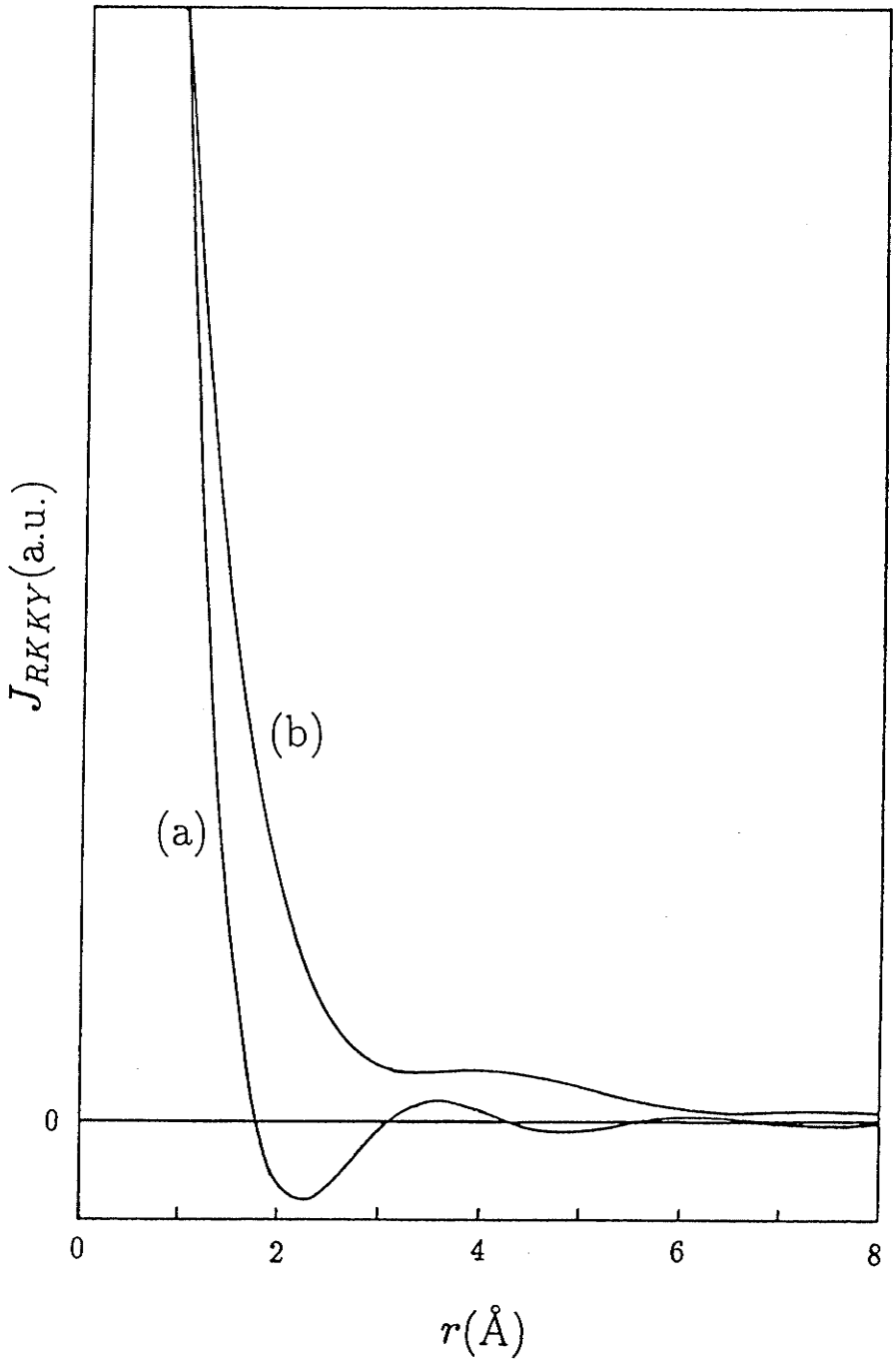

Figure 1.17: Curve (a) represents the functional form of the basic RKKY indirect exchange mechanism, while curve (b) includes the effects of exchange enhancement (after Foner, 1976).

1.2.2 The Edwards-Anderson Model

In 1975, Edwards and Anderson (E-A) developed a simple model which displays aspects of spin glass behavior. In particular, it successfully shows a cusp in the differential susceptibility at a temperature T_{SG}, separating the paramagnetic phase from the low temperature spin glass phase.

The model is based on a set of classical spins or magnetic dipoles $\vec{S}_i$, subject to an externally applied magnetic field $\vec{H}_0$, and interacting via the Heisenberg exchange Hamiltonian so that the total energy is

$$\mathcal{H} = -\frac{1}{2}\sum_{i,j} J_{ij}\vec{S}_i \cdot \vec{S}_j - \sum_i \vec{H}_0 \cdot \vec{S}_i \quad . \tag{1.29}$$

The exchange parameter J_{ij} between the ith and jth spins determines the strength of their interaction and whether they are coupled ferromagnetically ($J_{ij} > 0$) or antiferromagnetically ($J_{ij} < 0$). In our notation we require $J_{ij} = J_{ji}$ and $J_{ii} = 0$.

E-A postulated that a metallic spin glass can be thought of as a distribution of spins located randomly throughout a periodic lattice, and interacting with one another by means of a common (spatially oscillating) RKKY exchange parameter. Below some critical temperature T_{SG}, frustration causes a ground state to exist in which the spins freeze for all time in random orientations, and there is no long range magnetic order (in the usual sense). The spins settle into this ground state as temperature T approaches zero. Note that frustration can also occur in systems without RKKY interactions, as long as there exists a mechanism for random competition between ferromagnetic and anti-ferromagnetic exchange bonds.

Mathematically, it is cumbersome to deal with site disorder and complex

interactions in a direct manner. Instead, E-A chose to place a spin on *every* lattice site and independently distribute each parameter J_{ij} according to a Gaussian probability distribution (from Sherrington and Kirkpatrick, 1978)

$$\mathcal{P}(J_{ij}) = \frac{1}{J\sqrt{2\pi}} \exp\left(\frac{-J_{ij}^2}{2J^2}\right) \quad , \tag{1.30}$$

where J is the standard deviation. The distribution is centered about a mean exchange of zero, thus limiting the model to paramagnetic and spin glass behavior, since on average there is no net ferromagnetic exchange. Only nearest-neighbor interactions are considered.

In analogy to the magnetization in mean-field theories of ordered systems, E-A introduced a new order parameter q to characterize the onset of spin glass behavior. In particular, q is the probability (thermally averaged over all spins) that a spin $\vec{S}_i$ at time t_0 will point in the same direction at a much later time t. That is (after Binder and Young, 1986),

$$q = \left\langle \left\langle \vec{S}_i(t_0) \cdot \vec{S}_i(t) \right\rangle_T \right\rangle_i \quad ; \; t \gg t_0 \quad , \tag{1.31}$$

where the $\langle \langle \rangle_T \rangle_i$ denotes the thermal average and the average over all spins. For zero field and temperatures T *above* the spin glass temperature T_{SG}, $q = 0$ since the system is paramagnetic and the spins at different times are not correlated. However, for temperatures T *less* than T_{SG} the spins begin to freeze, so there is correlation and $q \neq 0$. As $T \rightarrow 0$ the thermal fluctuations decrease and $q \rightarrow 1$ (assuming unit spins). Note that in zero field the magnetization is zero for all temperatures, providing no indication of a phase change. In contrast, the order

parameter q *does* indicate the transition into a spin glass regime.

To evaluate the equilibrium properties of the model, E-A sought to minimize the quenched free energy. The free energy of a spin glass system with a particular random configuration of exchange bonds between N spins is $-k_B T \ln z$, where z is the partition function of the system. Since an infinite variety of random configurations are possible, the free energy must be averaged over all of them. Therefore

$$f = -k_B T \langle \ln z \rangle \quad , \tag{1.32}$$

where $\langle\rangle$ denotes an average over all possible exchange configurations. Introducing the identity (from Sherrington and Kirkpatrick, 1975)

$$\ln x = \lim_{n \to 0} \left(\frac{x^n - 1}{n} \right) \quad , \tag{1.33}$$

we have

$$f = \lim_{n \to 0} \frac{-k_B T}{n} \left(\langle z^n \rangle - 1 \right) \quad . \tag{1.34}$$

To evaluate $\langle z^n \rangle$, E-A introduced the concept of replicas. For integer n (from Sherrington and Kirkpatrick, 1978),

$$z^n = \prod_{\alpha=1}^{n} z_\alpha \quad , \tag{1.35}$$

where the set $\alpha = 1, \ldots, n$ represents n replica spin glass systems, all with the same free energy as the actual system, but with different exchange configurations. The average over the different configurations is no longer required, though we

must account for the individual J_{ij} distributions, so that (after Sherrington and Southern, 1975)

$$f = \lim_{n\to 0}\left(\frac{-k_BT}{n}\right)\left(\int \prod_{i,j}\left[\mathcal{P}(J_{ij})\,dJ_{ij}\right]\prod_{\alpha=1}^{n}\left[z_\alpha(J_{ij})\right]-1\right) \quad . \tag{1.36}$$

The classical partition function for replica α is

$$z_\alpha(J_{ij}) = \int\left[\prod_i d\vec{S}_i^{\alpha}\right]\exp\left\{\frac{-\mathcal{H}^\alpha}{k_BT}\right\} \tag{1.37}$$

and the Hamiltonian is

$$\mathcal{H}^\alpha = -\frac{1}{2}\sum_{i,j} J_{ij}\vec{S}_i^{\alpha}\cdot\vec{S}_j^{\alpha} - \sum_i \vec{H}_0\cdot\vec{S}_i^{\alpha} \quad . \tag{1.38}$$

Substituting equations 1.30, 1.37, and 1.38 into equation 1.36 and evaluating the integrals over the J_{ij} yields

$$\begin{aligned} f \;=\; \lim_{n\to 0}\left(\frac{-k_BT}{n}\right)\Bigg\{\int\left[\prod_\alpha\prod_i d\vec{S}_i^{\alpha}\right]\exp\Bigg[\sum_{i,j}\Bigg\{\frac{J^2}{4\,(k_BT)^2}\left(\sum_\alpha \vec{S}_i^{\alpha}\cdot\vec{S}_j^{\alpha}\right)\left(\sum_\beta \vec{S}_i^{\beta}\cdot\vec{S}_j^{\beta}\right)\Bigg\} \\ + \frac{1}{k_BT}\sum_\alpha\sum_i \vec{H}_0\cdot\vec{S}_i^{\alpha}\Bigg] - 1\Bigg\} \quad . \end{aligned} \tag{1.39}$$

Hence, the spins in replica α and replica β effectively interact with one another. This lead E-A to redefine their order parameter as (Edwards and Anderson, 1975)

$$q = \lim_{n\to 0}\left\langle \vec{S}_i^{\alpha}\cdot\vec{S}_i^{\beta}\right\rangle_T \quad ;\; \alpha\neq\beta \quad , \tag{1.40}$$

That is, replicas are used to represent the actual spin glass system at different times. E-A assumed the value of q is independent of the choice of replicas so that $q = \left\langle \left\langle \vec{S}_i \right\rangle_T^2 \right\rangle_J$.

After writing the free energy in terms of q, E-A were able to minimize it with respect to q and obtain the susceptibility and the specific heat. They found the zero-field susceptibility to be (from Edwards and Anderson, 1975)

$$\chi = \chi_c (1 - q) \quad , \tag{1.41}$$

where $\chi_c = C/T$ is the usual paramagnetic susceptibility with Curie constant C.

For $T > T_{SG}$, $q = 0$ and the susceptibility is paramagnetic. Also, for $T < T_{SG}$ and near T_{SG} they found

$$q = -\frac{1}{2}\left[1 - \left(\frac{T_{SG}}{T}\right)^2\right] \quad , \tag{1.42}$$

so that

$$\chi = \frac{C}{T_{SG}} - \mathcal{O}\left(T_{SG} - T\right)^2 \quad . \tag{1.43}$$

Hence, the susceptibility shows a cusp at temperature T_{SG} (which becomes rounded with the application of an external field) and is qualitatively similar to experimental results. As $T \rightarrow 0$, the susceptibility approaches a constant value of

$$\chi = \frac{C}{T_{SG}}\left(\frac{2}{3\pi}\right)^{1/2} \quad . \tag{1.44}$$

Contrary to experimental observations, the specific heat also displays a

cusp around T_{SG}. Furthermore, the E-A order parameter is now considered to be too simple, as mentioned in section 1.2.5. Despite these drawbacks, the model provides a basis for more sophisticated investigations of spin glass behavior.

1.2.3 The Sherrington-Kirkpatrick Model

Sherrington and Kirkpatrick (S-K) introduced a model of disordered magnets in 1975, based on the Edwards-Anderson replica technique. The model is more sophisticated in that it adopts a quantum mechanical approach and allows for competition between ferromagnetic and spin glass ordering. Furthermore, (in analogy to the *exact* mean-field theory of ferromagnets) the system is evaluated in the thermodynamic limit, using infinitely ranged exchanges that are scaled with the number of spins.

The model involves a lattice of N Ising spins ($S_i = \pm 1$), subject to an external field H_0 (applied in the direction of quantization), and interacting via the Ising Hamiltonian so that the total Hamiltonian is

$$\mathcal{H} = -\frac{1}{2}\sum_{i,j} J_{ij} S_i S_j - h\sum_i S_i \quad , \tag{1.45}$$

where $h = -g\mu_B H_0$. The exchange parameters are independently distributed using a Gaussian function

$$\mathcal{P}(J_{ij}) = \frac{1}{J\sqrt{2\pi}} \exp\left(\frac{-[J_{ij} - J_0]^2}{2J^2}\right) \quad , \tag{1.46}$$

where J is the standard deviation. Ferromagnetic ordering is allowed to exist by centering the distribution about a non-zero mean ($J_0 > 0$).

To scale J and J_0 with the number of spins N (and prevent infinite energy in the thermodynamic limit), the intensive variables $\overline{J}$ and $\overline{J_0}$ are introduced such

that

$$J_0 = \frac{\overline{J_0}}{N} \quad \text{and} \quad J = \frac{\overline{J}}{N^{1/2}} \quad .$$

The ratio $\overline{J_0}/\overline{J}$ is important in determining the properties of the system, and is related to the fractional concentration of magnetic impurity atoms in a dilute magnetic alloy.

Following the Edwards-Anderson replication procedure, the thermodynamic limit of the free energy per spin is obtained by modifying equation 1.36 such that

$$f = \lim_{N\to\infty}\lim_{n\to 0}\left(\frac{-k_BT}{Nn}\right)\left(\int\prod_{i,j}\left[\mathcal{P}(J_{ij})\,dJ_{ij}\right]\prod_{\alpha=1}^{n}\left[z_\alpha(J_{ij})\right]-1\right) \quad . \tag{1.47}$$

Also, the quantum mechanical partition function for replica α is given by

$$z_\alpha(J_{ij}) = \mathrm{Tr}\,\exp\left\{\frac{-\mathcal{H}^\alpha}{k_BT}\right\} \quad , \tag{1.48}$$

where $\mathcal{H}^\alpha$ is the Hamiltonian and the trace is over all the spins of the replica. Substituting equations 1.46 and 1.48 into equation 1.47 and evaluating the integrals over the J_{ij} yields (after Sherrington and Kirkpatrick, 1975 and 1978)

$$\begin{aligned} f \;=\; & \lim_{N\to\infty}\lim_{n\to 0}\left(\frac{-k_BT}{Nn}\right)\left\{\mathrm{Tr}_n\,\exp\left[\sum_{i,j}\left\{\frac{J^2}{4\,(k_BT)^2}\left(\sum_\alpha S_i^\alpha S_j^\alpha\right)\left(\sum_\beta S_i^\beta S_j^\beta\right)\right.\right.\right. \\ & \left.\left.\left. +\;\frac{J_0}{2k_BT}\sum_\alpha S_i^\alpha S_j^\alpha\right\}+\frac{1}{k_BT}\sum_\alpha\sum_i hS_i^\alpha\right]-1\right\} \quad , \end{aligned} \tag{1.49}$$

where the trace is over all the spins of the n replicas. Hence, as in the Edwards-Anderson model, there is an effective interaction between the spins in any two

replicas α and β. The identity (from Sherrington and Kirkpatrick, 1978)

$$\exp(\lambda a^2) = \frac{1}{\sqrt{2\pi}} \int dx \, \exp\left[-\frac{1}{2}x^2 + (2\lambda)^{1/2} a x\right]$$

is used to convert the problem to a trace over n replicas at a *single* spin site. Employing a method of steepest-descent to perform the integrals and minimize the free energy, S-K eventually obtained the following expression (from Sherrington and Kirkpatrick, 1975):

$$f = \frac{\overline{J}_0 m^2}{2} - \frac{\overline{J}^2 (1-q)^2}{4 k_B T} - \frac{k_B T}{\sqrt{2\pi}} \int_{-\infty}^{+\infty} d\omega \, \exp\left(\frac{-\omega^2}{2}\right) \ln(2 \cosh \Xi) \quad , \qquad (1.50)$$

where $\Xi \equiv \left(\overline{J}_0 m + \overline{J}\sqrt{q}\,\omega + h\right)/k_B T$. The m and q are defined by the coupled equations

$$m \equiv \langle \langle S_i \rangle_T \rangle_J = \frac{1}{\sqrt{2\pi}} \int_{-\infty}^{+\infty} d\omega \, \exp\left(\frac{-\omega^2}{2}\right) \tanh \Xi \qquad (1.51)$$

$$q \equiv \left\langle \langle S_i \rangle_T^2 \right\rangle_J = \frac{1}{\sqrt{2\pi}} \int_{-\infty}^{+\infty} d\omega \, \exp\left(\frac{-\omega^2}{2}\right) \tanh^2 \Xi \quad , \qquad (1.52)$$

where $\langle \langle \rangle_T \rangle_J$ denotes the thermal and exchange bond averages.

Equation 1.51 is simply a generalization of the transcendental equation obtained from the mean-field theory of ferromagnetism (equation 1.1). The relationship is made obvious by setting $\overline{J} = 0$. Physically, m represents the local magnetization (or magnetization per spin site) and is a measure of the ferromagnetic order of the system. On the other hand, q represents an Edwards-Anderson-like order parameter and is a measure of the *frozen* order of the system, whether it be

ferromagnetic or spin glass in nature.

Solving the coupled equations, as a function of temperature T and the ratio $\eta = \overline{J}_0 / \overline{J}$, yields the zero-field magnetic phase diagram of Figure 1.18. The paramagnetic region is that portion of the phase diagram for which both m and q are zero. In other regions, the ferromagnetic order competes with the spin glass order and the resulting phase is determined by whichever is dominant. The ferromagnetic region has non-zero values for both m and q, whereas the spin glass phase is defined as the region for which q is non-zero but m is zero. All three phases are separated by abrupt second-order phase transitions, though these become less well defined in finite fields (for which m and q are always non-zero).

For $\eta \geq 1.25$, the paramagnetic region gives way to ferromagnetic ordering below a temperature $T_c = \overline{J}_0 / k_B$. Similarly, for $\eta \leq 1$ there is a transition from paramagnetic to spin glass ordering at a temperature $T_{SG} = \overline{J} / k_B$. Lastly, the region $1 < \eta < 1.25$ is *re-entrant*, with sequential transitions from paramagnetic to ferromagnetic to spin glass ordering as the temperature is lowered through the phase boundaries. The solutions for $m(T)$ and $q^{1/2}(T)$ that were obtained by S-K (using numerical methods) are portrayed in Figure 1.19. Note that for $\eta \rightarrow \infty$, $m = q^{1/2}$, indicating that the spin glass order has disappeared and the frozen order is entirely ferromagnetic.

Evaluating $\partial m / \partial h$ and letting $h \rightarrow 0$ yields the zero-field differential susceptibility (from Sherrington and Kirkpatrick, 1978)

$$\chi(T) = \frac{1 - q(T)}{k_B T - \overline{J}_0 [1 - q(T)]} \quad , \tag{1.53}$$

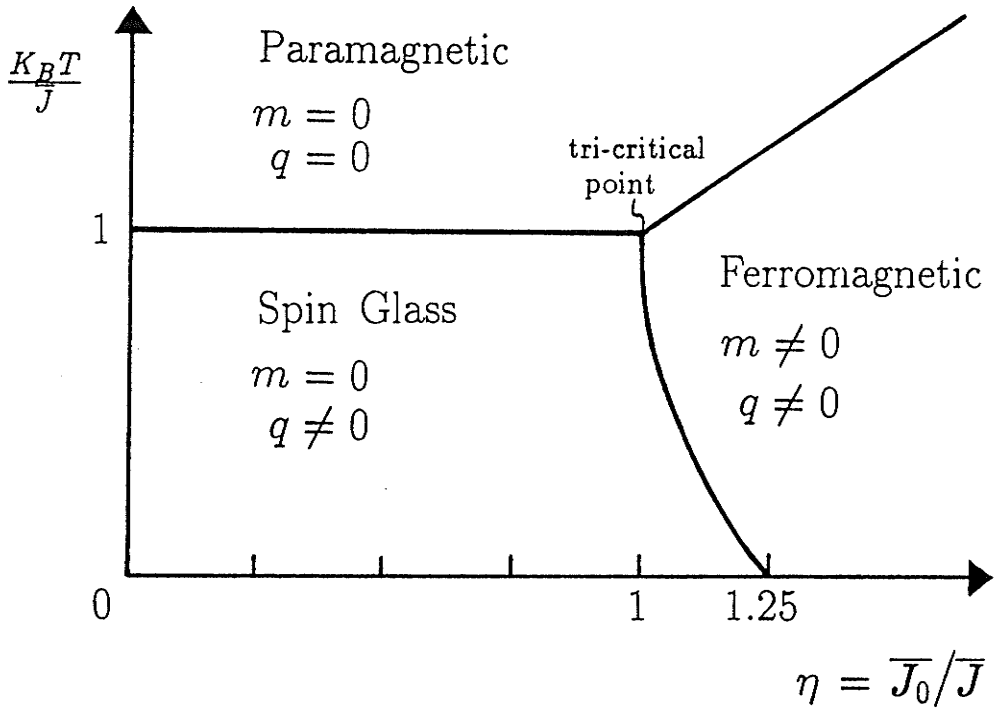

Figure 1.18: The zero-field magnetic phase diagram of the Sherrington-Kirkpatrick model. The region $1 < \eta < 1.25$ is re-entrant (after Sherrington et al., 1975).

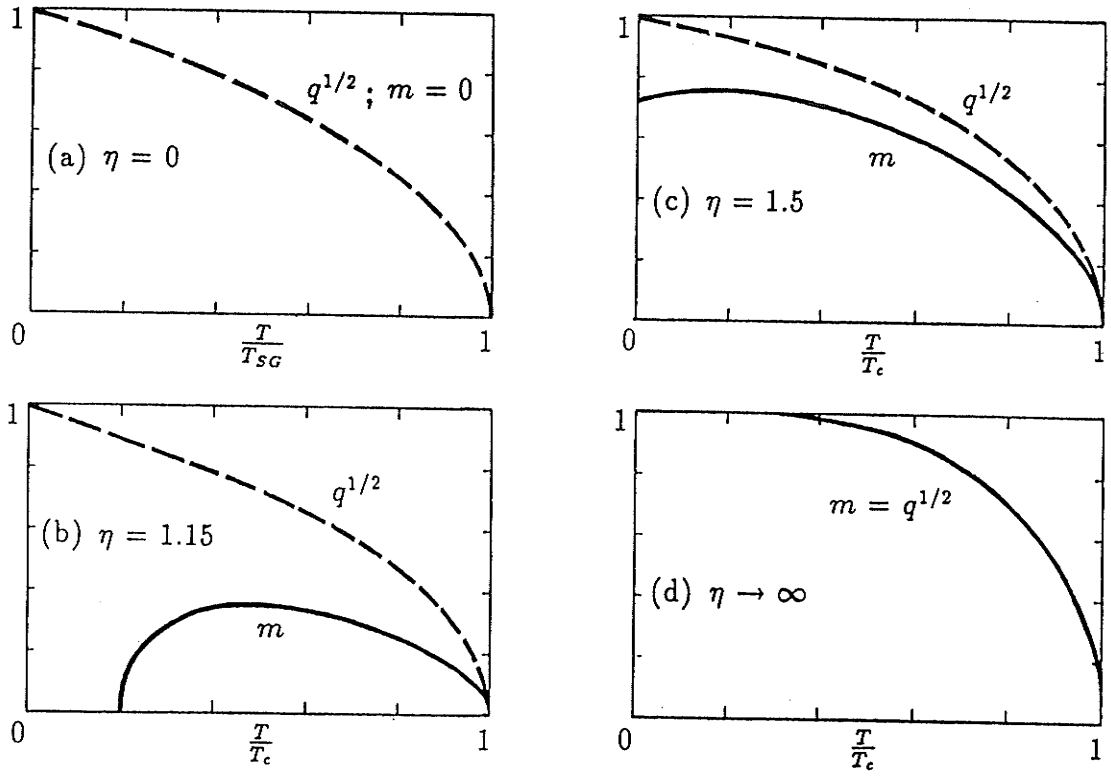

Figure 1.19: Numerical solutions of the S-K coupled equations for various values of $\eta = \overline{J_0}/\overline{J}$:
(a) pure spin glass,
(b) re-entrant,
(c) disordered ferromagnet,
(d) pure ferromagnet.
(After Sherrington et al., 1978)

for the spin glass region $\eta < 1$. There is a cusp at the paramagnetic to spin glass ordering temperature, above which $q = 0$ and a Curie-Weiss law is obeyed. The cusp becomes rounded with the application of a finite field, as shown in Figure 1.20.

Though χ is qualitatively similar to experimental results, there are difficulties with other thermodynamic functions. Contrary to experiment (but like the Edwards-Anderson model) the specific heat shows a cusp at the paramagnetic to spin glass transition temperature. At all the other transition temperatures (including the re-entrant ferromagnetic to spin glass transition) the specific heat is step-discontinuous.

In addition, the entropy of the system becomes unphysical (i.e. negative) as $T \rightarrow 0$, indicating problems with the replica technique at low temperatures. Further investigations by other groups have revealed instabilities in the S-K solutions for the low temperature spin glass and ferromagnetic regions —see section 1.2.5 for a discussion of the consequences. Nonetheless, the S-K solutions display some desirable features (especially in regards to re-entrant systems) and remain a popular interpretation of the magnetic behavior of dilute alloys.

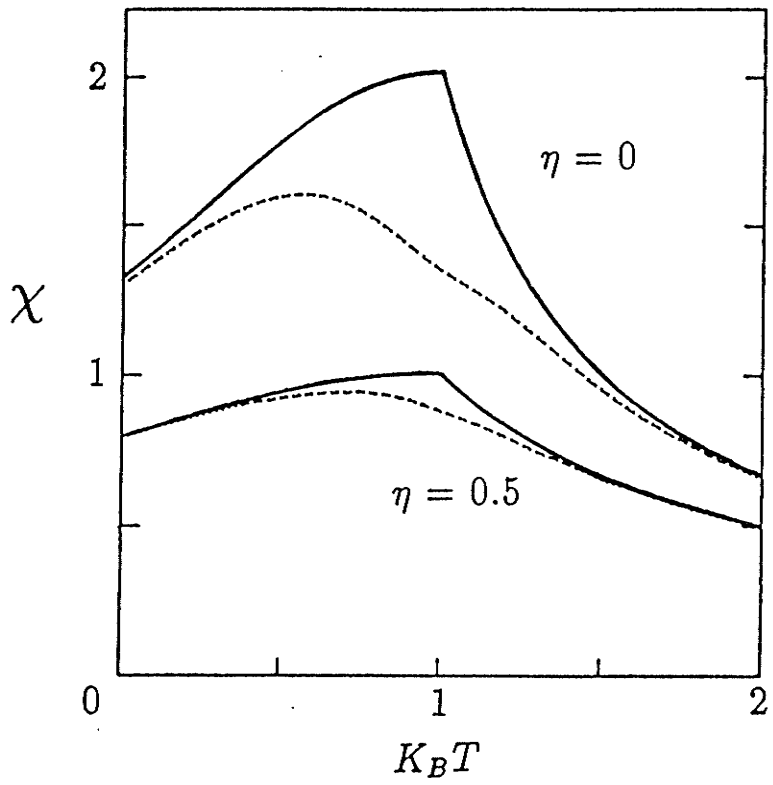

Figure 1.20: Differential susceptibilities of two spin glasses, as calculated by the S-K model. The solid curves are for zero field, while the dashed curves represent $h = 0.1\overline{J_0}$ (after Sherrington et al., 1975).

1.2.4 The Effective Field Model for Arbitrary Spin

In 1976, Southern introduced an effective field theory of disordered magnets, based on the $S_i = \pm 1$ Ising Hamiltonian used by Sherrington and Kirkpatrick (S-K). The technique does not use replicas and allows discussion of different quenched systems by varying the nature of the exchange bond distributions. In particular, the model can be used to obtain the Sherrington-Kirkpatrick (S-K) coupled equations, but avoids the low-temperature negative entropy problems associated with the S-K replica method.

The following is a derivation of the S-K-like coupled equations for a system with arbitrary spin, and is based on Southern's work (Southern, 1976). For comparison, equations corresponding to a spherical model (i.e., a system with a continuous spin-space of infinite dimensionality) are also developed.

The Ising Hamiltonian for arbitrary spin quantum number S is

$$\mathcal{H} = -\frac{1}{2}\sum_{i,j} J_{ij} S_i S_j - h\sum_i S_i \quad , \tag{1.54}$$

where each S_i has $2S+1$ components (i.e., $-S \leq S_i \leq S$). After Mühlschlegal and Zittartz (1963), the following exact relation can be derived (Roshko and Williams, 1984):

$$\langle S_i \rangle_T = \langle S B_S[S\beta(h + H_i)] \rangle_T \quad , \tag{1.55}$$

where the thermal average of an operator A is given by

$$\langle A \rangle_T = \frac{\mathrm{Tr}\, A e^{-\beta\mathcal{H}}}{\mathrm{Tr}\, e^{-\beta\mathcal{H}}} \quad ; \beta = \frac{1}{k_B T} \quad .$$

The *effective field* acting on spin S_i due to all other spins is $H_i = \sum_j J_{ij} S_j$, and h is related to the magnetic field H_0 (applied in the direction of quantization) by $h = -g\mu_B H_0$. Also, the Brillouin function is defined as

$$B_S[x] = \frac{2S+1}{2S} \coth\left(\frac{(2S+1)x}{2S}\right) - \frac{1}{2S} \coth\left(\frac{x}{2S}\right) \quad . \tag{1.56}$$

By averaging equation 1.55 over the exchange bonds, expressions involving the local magnetization m and the correlation function q can be written as

$$m \equiv \langle\langle S_i \rangle_T \rangle_J = \int_{-\infty}^{+\infty} d\omega \, S B_S[S\beta\omega] \, \overline{\rho}_i(\omega) \quad , \tag{1.57}$$

$$q \equiv \left\langle \langle S_i \rangle_T^2 \right\rangle_J = \int_{-\infty}^{+\infty} d\omega \, S^2 B_S^2[S\beta\omega] \, \overline{\rho}_i(\omega) \quad , \tag{1.58}$$

where

$$\overline{\rho}_i(\omega) = -\frac{1}{\pi} \Im \lim_{\delta \to 0^+} \left\langle \left\langle \frac{1}{\omega + i\delta - h - H_i} \right\rangle_T \right\rangle_J \quad . \tag{1.59}$$

(The symbol $\Im$ indicates the imaginary part of the expression.) Aside from the averaging over $\langle\langle\rangle_T\rangle_J$, equation 1.59 is similar to a δ-function. The averaging serves to introduce thermal and exchange fluctuations in the fields H_i which depend on the particular distribution schemes chosen.

In evaluating the thermal average, the simplest scheme is the *Weiss mean-field approximation* which involves no fluctuations and corresponds to replacing $\langle H_i^n \rangle_T$ with $\langle H_i \rangle_T^n$ (where n is a positive integer). Thus

$$\overline{\rho_i}(\omega) = -\frac{1}{\pi} \Im \lim_{\delta \to 0^+} \left\langle \frac{1}{\omega + i\delta - h - x_i} \right\rangle_J \quad , \tag{1.60}$$

where $x_i = \langle H_i \rangle_T$ is the *mean field*, or thermally averaged effective field acting on spin S_i.

To calculate the average of the mean fields over the exchanges, a better approximation scheme is used which includes the effects of fluctuations and yields a Gaussian distribution for $\overline{\rho_i}(\omega)$. That is, letting (after Southern, 1976)

$$\left\langle (x_i - \overline{x}_i)^{2n} \right\rangle_J \approx (2n-1)!! \, \overline{\sigma_i}^{2n} \quad , \tag{1.61}$$

$$\left\langle (x_i - \overline{x}_i)^{2n+1} \right\rangle_J \approx 0 \quad , \tag{1.62}$$

yields

$$\overline{\rho_i}(\omega) = \frac{1}{\sqrt{2\pi \overline{\sigma_i}^2}} \exp\left(\frac{-[\omega - h - \overline{x_i}]^2}{2\overline{\sigma_i}^2} \right) \quad , \tag{1.63}$$

where the variables are introduced below.

Define an average, $\overline{x_i}$, such that (after Southern, 1976)

$$\begin{aligned} \overline{x_i} &= \langle x_i \rangle_J \\ &= \left\langle \sum_j J_{ij} \langle S_j \rangle_T \right\rangle_J \\ &\approx \left\langle \langle S_j \rangle_T \right\rangle_J \left(\sum_j \langle J_{ij} \rangle_J \right) \quad , \end{aligned} \tag{1.64}$$

where a mean-field approximation has been used so that

$$\overline{x_i} \approx m \overline{J_0} \qquad \text{with} \qquad \overline{J_0} = \sum_j \langle J_{ij} \rangle_J \quad . \tag{1.65}$$

Also define a variance

$$\overline{\sigma}_i^2 = \left\langle x_i^2 \right\rangle_J - \langle x_i \rangle_J^2 \quad . \tag{1.66}$$

Once again using a mean-field approximation it can be shown that (after Southern, 1976)

$$\begin{aligned} \left\langle x_i^2 \right\rangle_J &= \left\langle \sum_{j,k_{j\neq k}} J_{ij} J_{ik} \langle S_j \rangle_T \langle S_k \rangle_T \right\rangle_J + \left\langle \sum_j J_{ij}^2 \langle S_j \rangle_T^2 \right\rangle_J \\ &\approx m^2 \overline{J_0}^2 + q\overline{J}^2 \quad , \end{aligned} \tag{1.67}$$

with

$$\overline{J}^2 = \sum_j \left\{ \left\langle J_{ij}^2 \right\rangle_J - \langle J_{ij} \rangle_J^2 \right\} \quad .$$

Equations 1.65, 1.66, and 1.67 give

$$\overline{\sigma_i}^2 = q\overline{J}^2 \quad . \tag{1.68}$$

The variables $\overline{x_i}$ and $\overline{\sigma_i}^2$ describe the distribution of mean fields x_i. Note that $\overline{J_0}$ and $\overline{J}$ are related to the mean exchange J_0 and the deviation J of the corresponding exchange bond distribution in the S-K model by

$$J_0 = \frac{\overline{J_0}}{N} \quad \text{and} \quad J = \frac{\overline{J}}{N^{1/2}} \quad ,$$

where N is the number of spins.

Returning to equation 1.63, set $\alpha = (\omega - h - \overline{x_i})/\overline{\sigma_i}$. Thus equations 1.57

and 1.58 become (Roshko and Williams, 1984)

$$m = \frac{1}{\sqrt{2\pi}} \int_{-\infty}^{+\infty} d\alpha \, \exp\left(\frac{-\alpha^2}{2}\right) \, S B_S\left[S\beta\left(\overline{J_0} m + \overline{J}\sqrt{q}\,\alpha + h\right)\right] \quad , \quad (1.69)$$

$$q = \frac{1}{\sqrt{2\pi}} \int_{-\infty}^{+\infty} d\alpha \, \exp\left(\frac{-\alpha^2}{2}\right) \, S^2 B_S^2\left[S\beta\left(\overline{J_0} m + \overline{J}\sqrt{q}\,\alpha + h\right)\right] \quad . \quad (1.70)$$

Equations 1.69 and 1.70 for arbitrary spin are analagous to the S-K coupled equations for $S_i = \pm 1$. To recover the S-K and Southern results, set $S = 1$ and replace $B_S[x]$ with $\tanh(x)$. The phase diagram which Southern obtained is identical to that of S-K (Figure 1.18). For arbitrary spin S, the transitions between paramagnetism and ferromagnetic or spin glass ordering occur, respectively, at the temperatures

$$T_c = \frac{S(S+1)\overline{J_0}}{3k_B} \quad (1.71)$$

and

$$T_{SG} = \frac{S(S+1)\overline{J}}{3k_B} \quad . \quad (1.72)$$

Furthermore, there exists a *re-entrant* region ($1 < \overline{J_0}/\overline{J} < 1.25$) with any one of the three magnetic phases possible, depending on the temperature. The phase diagram is, however, sensitive to the type of exchange bond distribution used.

A similar phase diagram is obtained for the $S = 1$ spherical model, where $\sum_i S_i^2 = N$ is the only constraint on the spins of the system. Equations 1.61 and 1.62 are replaced by the following exchange fluctuation approximations:

$$\left\langle x_i^{2n} \right\rangle_J \approx \left\langle x_i^2 \right\rangle_J^n \quad , \quad (1.73)$$

$$\left\langle x_i^{2n+1} \right\rangle_J \approx \left\langle x_i^2 \right\rangle_J^n \langle x_i \rangle_J = \left\langle x_i^2 \right\rangle_J^n \overline{x_i} \quad . \tag{1.74}$$

As a result, equation 1.63 becomes a double δ-function distribution (Southern, 1976),

$$\begin{aligned} \overline{\rho_i}(\omega) &= \frac{1}{2}\left(1 + \frac{\overline{x_i}}{\sqrt{\langle x_i^2 \rangle_J}}\right) \delta\left(\omega - h - \sqrt{\langle x_i^2 \rangle_J}\right) \\ &\quad + \frac{1}{2}\left(1 - \frac{\overline{x_i}}{\sqrt{\langle x_i^2 \rangle_J}}\right) \delta\left(\omega - h + \sqrt{\langle x_i^2 \rangle_J}\right) \quad . \end{aligned} \tag{1.75}$$

Substituting equation 1.75 into equations 1.57 and 1.58 and setting $h = 0$ yields the coupled equations (Southern, 1976)

$$m = \frac{\overline{x_i}}{\sqrt{\langle x_i^2 \rangle_J}} \tanh\left[\beta\sqrt{\langle x_i^2 \rangle_J}\right] \quad , \tag{1.76}$$

$$q = \tanh^2\left[\beta\sqrt{\langle x_i^2 \rangle_J}\right] \quad . \tag{1.77}$$

The spherical model phase diagram differs from the S-K results in that a re-entrant region does not appear at all. Instead, a vertical transition line at $\overline{J_0}/\overline{J} = 1$ joins the tri-critical point to the horizontal axis.

1.2.5 Instabilities and Replica-Symmetry-Breaking

A-T Lines

The negative entropy of the Sherrington-Kirkpatrick (S-K) solutions to the mean-field model of disordered magnets (section 1.2.3) indicates problems with the replica procedure at low temperatures. Implicit in their method of steepest-descent is the evaluation of the free energy f at the saddle-point (Binder and Young, 1986)

$$\frac{\partial f}{\partial q_{\alpha\beta}} = \frac{\partial f}{\partial m_\alpha} = 0 \quad , \tag{1.78}$$

where $q_{\alpha\beta} = \lim_{n\to 0} \left\langle S_i^\alpha S_i^\beta \right\rangle_T$ and $m_\alpha = \lim_{n\to 0} \langle S_i^\alpha \rangle_T$. In using the Edwards-Anderson replica method, one assumes that $q_{\alpha\beta}$ is invariant (symmetric) under permutation of the replicas ($q_{EA} = q_{\alpha\beta}$ for all $\alpha \neq \beta$), and that the saddle-point conditions minimize the free energy.

De Almeida and Thouless (1978) scrutinized these assumptions and discovered low-temperature regions of the phase diagram for which the replica-symmetric solutions do not represent the ground state of the system, but are *unstable*. Their argument is based on the following inequality (after de Almeida and Thouless, 1978):

$$\left(\frac{k_B T}{\overline{J}}\right)^2 > \frac{1}{\sqrt{2\pi}} \int_{-\infty}^{+\infty} d\alpha \, \exp\left(\frac{-\alpha^2}{2}\right) \operatorname{sech}^4\left[\beta\left(\overline{J_0} m + \overline{J}\sqrt{q}\,\alpha + h\right)\right] \quad . \tag{1.79}$$

Stable solutions correspond to areas of the phase diagram which satisfy the inequality, while so-called A-T instability lines, separating stable and unstable regions, are calculated by converting to an equality. Various instability lines for

both zero and non-zero field are displayed in Figure 1.21. Notice that for zero field the entire spin glass region has unstable solutions and the S-K re-entrant transition line, between ferromagnetic and spin glass ordering, is lost. However, increasing the field strength pushes the instability region to lower temperatures, and for high enough fields the solutions around the re-entrant line are stable. This is important, as it implies that manifestations of the zero-field re-entrant transition can be discerned from the stable S-K solutions in finite field. A-T suggested that the instabilities can be removed by *breaking the symmetry* between replicas, but they were unable to offer an appropriate solution.

Parisi's Broken-Replica-Symmetry Solutions

Parisi (1979, 1980) developed a popular scheme to break the symmetry, such that (in the unstable S-K regions) the Edwards-Anderson order parameter q_{EA} is replaced by a function $q(x)$ which represents the order parameters of infinitely many pairs of replicas. The effective order parameter is then an integration over all x:

$$q_{eff} = \int_{x=0}^{x=1} q(x)\, dx \quad .$$

Each value of x corresponds to a set containing all the pairs of replicas with the same parameter $q(x)$. Parisi proposed a complex hierarchial structure to choose the $q(x)$, with $0 \leq x \leq 1$ and $q(1) = q_{EA}$.

According to Binder and Young (1986), this structure implies the existence of a free energy hypersurface $f(m, q)$ with a complicated landscape of valleys within valleys. Each point on the hypersurface represents a particular spin configuration, while the valley bottoms denote the various (stable or meta-stable)

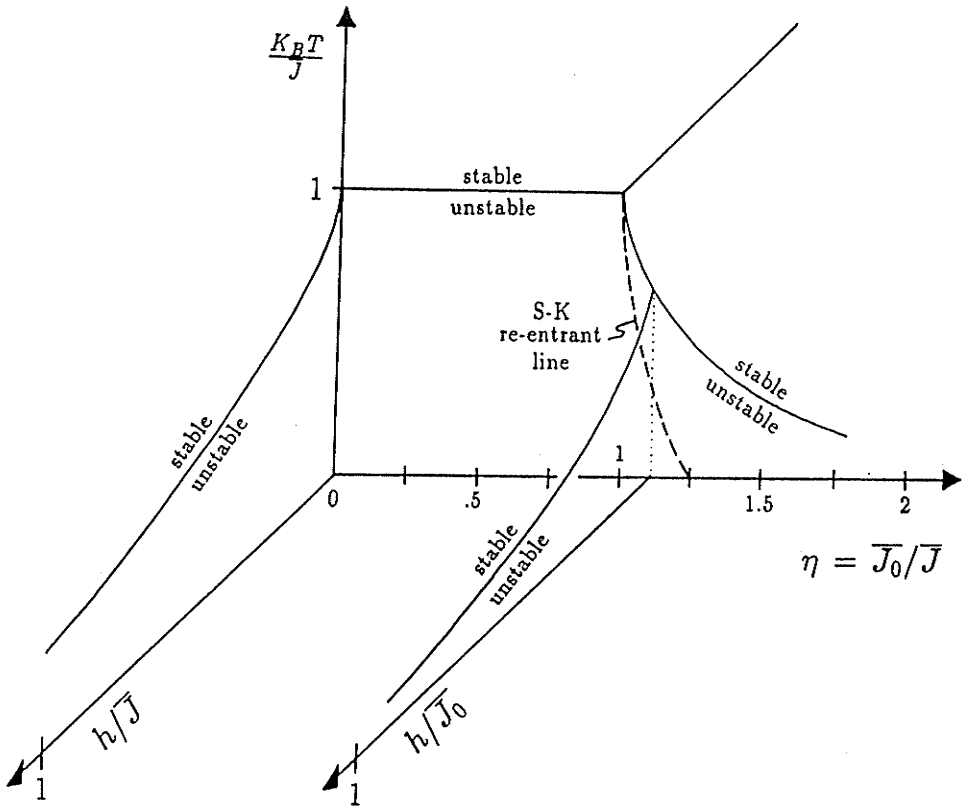

Figure 1.21: The A-T instability lines of the Sherrington-Kirkpatrick (Ising spin) phase diagram. The unstable regions represent broken replica-symmetry.

thermodynamic states available to the system. Upon decreasing the temperature, increasingly many configurations gain stability so that the landscape gradually develops new valleys.

Grest et al. (1983) further suggest that valleys are destroyed with increasing temperature, while both destruction and creation occur for even small changes in applied field. Whenever the system finds itself in an unstable configuration (i.e., along the wall of a valley), it will rapidly reconfigure itself until it sits in the nearest local minimum. Once there, however, it may eventually relax into a more stable state by hopping over free energy barriers (via thermal activation), or be forced into a new configuration by evolution of the landscape with temperature or field changes. Since the destruction of energy minima implies irreversibility, while minima-hopping implies slow relaxation, Grest et al. deem it reasonable to associate the onset of replica-symmetry-breaking with the onset of hysteresis, remanence, and time effects.

In this context, the original S-K solutions correspond to a time during which the system is caught within one of the meta-stable valleys that satisfy the symmetric saddle-point condition (equation 1.78). Such a state is not considered to be in true equilibrium, as the system has not sampled the other thermodynamic states to find the most stable configuration. The S-K solutions presumably correspond to a hypothetical zero-field-cooled (ZFC) magnetization curve which has not had a chance to evolve with time towards the field-cooled (FC) values, though this non-evolved curve is impossible to obtain experimentally. Even so, since the ZFC magnetization is closely related to the A.C. susceptibility, this notion is supported by the strong qualitative agreement between the S-K predictions and (**Pd**Fe)Mn

susceptibility measurements (section 1.1.3), in both the spin glass and re-entrant regimes.

Continuing with the mean-field model, it has been proposed that the free energy barriers between states actually diverge in the thermodynamic limit, as do the times for the system to relax from one valley to another (i.e., the system is essentially non-ergodic). Nevertheless, in the limit of long times, the system has a chance to sample the thermodynamic states according to a statistical probability distribution, and eventually reaches true equilibrium in a stable valley. This sampling of different states is facilitated in the Parisi theory by a probability distribution $\mathcal{P}(q) = dx/dq$ such that (after Binder and Young, 1986)

$$q_{eff} = \int q\,\mathcal{P}(q)\,dq \quad .$$

The distribution represents the amount of degeneracy or overlap between the various valleys. However, $\mathcal{P}(q)$ depends on the exchange configurations of the valleys in question, and so is itself represented by a distribution of some sort. Above the A-T lines, there is only a single ground state configuration available to the system so that $\mathcal{P}(q) = \delta(q - q_{EA})$ and $q_{eff} = q_{EA}$.

Since FC magnetization measurements tend to display only very weak time effects (section 1.1.3), they may be near true equilibrium and hence comparable to results obtained by the Parisi theory. This notion is supported with the susceptibility obtained by Parisi for the pure spin glass case ($\eta = 0$). The zero-field susceptibility levels off to a constant maximum value for all temperatures below T_{SG}, and this behavior is at least vaguely reminiscent of the FC magnetization curves (which essentially represent the static susceptibility M/H) obtained

through experiment (Figure 1.12).

The PaT Hypothesis

The Parisi scheme is generally considered to yield exact solutions to the mean-field model, but evaluation is hindered by the lack of a functional form for $q(x)$ (except near T_{SG}). In 1980, Parisi and Toulouse (PaT) introduced a *projection* scheme to derive some of the properties of the spin glass region (for $\eta = 0$ and $h \neq 0$) from the stable solutions along the A-T line. In doing so, they hypothesized that the following expressions are valid in the unstable region (after Parisi, 1981):

$$\frac{\partial S}{\partial h} = \frac{\partial m_\alpha}{\partial T} = \frac{\partial q_{EA}}{\partial h} = 0 \quad ,$$

where S is the entropy. The terms involving h imply that the macroscopic behavior of the system is insensitive to changes of applied field. That is, upon changing the field, there are many different microscopic states available to the system, but they are all nearly degenerate with the original state, and have roughly the same macroscopic properties. The magnetization is assumed to be completely independent of temperature, though this is also an approximation. They discovered weak jumps in the specific heat and susceptibility across the instability line, suggesting some sort of *third*-order phase change. Later that year, Toulouse determined that the PaT hypothesis is also valid for $\eta \neq 0$. He derived the $\eta \neq 0$ case by adding the term $-\overline{J_0}\frac{m^2}{2}$ to the free energy for $\eta = 0$. A transition line at $\eta = 1$ was also found (similar to that of Southern's spherical model—see section 1.2.4). However, a description as to the nature of the phases was not provided.

G-T Lines

A possible answer came in 1981, when Gabay and Toulouse (G-T) investigated a S-K-like system with classical m-component Heisenberg spins (as opposed to the usual mean-field model with $m = 1$, or the spherical model with $m \to \infty$). Using Cartesian components ($m = 3$) and a field in the direction $\mu = 1$, the appropriate Hamiltonian is (after Toulouse and Gabay, 1981)

$$\mathcal{H} = -\frac{1}{2}\sum_{i,j} J_{ij} \sum_{\mu} S_{i\mu} S_{j\mu} - h \sum_{i} S_{i1} \quad , \tag{1.80}$$

where i and j are site labels, $\mu = 1, \ldots, m$ denotes the spin components, and $\sum_{\mu=1}^{m} S_{i\mu}^2 = m$. For convenience, k_B and $\overline{J}$ are set to unity, so that $\eta = \overline{J_0}$.

As in the $m = 1$ case, there is an order parameter

$$q_1 = \left\langle \langle S_{i1} \rangle_T^2 \right\rangle_J \quad ,$$

which describes the longitudinal order (i.e., along the field direction). It follows that another order parameter

$$q_t = \left\langle \langle S_{i\mu} \rangle_T^2 \right\rangle_J \quad ; \; \mu \neq 1$$

exists to indicate ordering in directions transverse to the applied field.

They obtained two different types of transition lines for the phase diagram. The lines for $h \neq 0$ and $\overline{J_0} = 0$ (i.e., no ferromagnetic ordering possible) are shown in Figure 1.22. Line (a) is a so-called G-T line, and separates the paramagnetic phase ($q_t = 0$) from a lower temperature phase in which the transverse spin

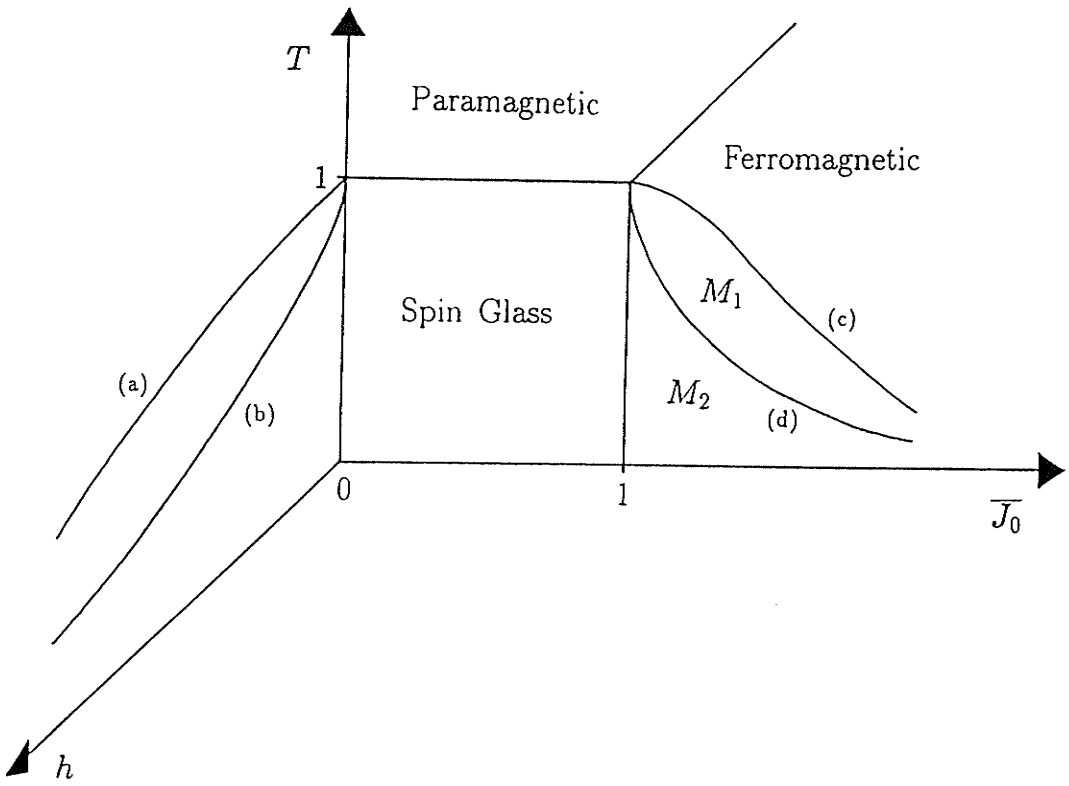

Figure 1.22: The magnetic phase diagram of the classical Sherrington-Kirkpatrick-like model with 3-dimensional Heisenberg spins. Curves (a) and (c) are G-T lines, while curves (b) and (d) are A-T lines. The mixed phase M_1 is a canted ferromagnetic phase with spin glass ordering of the transverse spin components. Phase M_2 is similar, but possesses broken replica symmetry.

components are frozen into random directions (so that $q_t \neq 0$). Since the field is finite, there is some polarization along the field direction and q_l is non-zero on both sides of the transition. Upon lowering the temperature further, line (b) is encountered. It is the m-component analogue of the A-T line, and corresponds to replica symmetry breaking.

They also obtained the transition lines for $h = 0$ and $\overline{J_0} \neq 0$ (i.e., ferromagnetic ordering possible). These are also shown in Figure 1.22. Line (c) is another G-T line, and separates the ferromagnetic region (with $q_t = 0$ and $q_l \neq 0$) from a lower temperature *mixed* phase, M_1 (with q_t and q_l both non-zero). That is, the collinear ferromagnetic region (with no transverse ordering) gives way to a *canted* ferromagnetic phase in which the transverse spin components are spin glass ordered. Line (d) is another A-T line, and indicates the transition into a mixed phase M_2 with broken replica symmetry. There is an additional line at $\overline{J_0} = 1$, separating the mixed phase M_2 from an unmixed phase in which all the spin components have spin glass order. It should be noted that the G-T model is presently incapable of providing detailed quantitative predictions, so that its relationship to experimental systems (particularly those which display re-entrant characteristics) is not yet clear.

To add more experimentally accessible elements to the G-T model, Cragg, Sherrington, and Gabay (1982) suggested that the breaking of replica symmetry occurs immediately upon entering regions with transverse spin glass order. As a result, the mixed phase M_1 is associated (supposedly) with weak irreversibility of the longitudinal spin components, while the phase M_2 corresponds to strong irreversibility of these components. Strong irreversibility of the transverse degrees

of freedom is associated with all the phases with broken symmetry. These effects are, however, particularly difficult to analyse in experimental re-entrant systems, due to the non-critical domain wall dynamics which complicate the magnetic behavior below the Curie temperature.

To summarize, the instabilities of the low temperature S-K solutions (due to the breaking of replica symmetry) were studied by several groups. The original phase diagram has been modified to include canted ferromagnetic phases with spin glass ordering of the transverse spin components. Moreover, these mixed phases seem to exist at the expense of the simple S-K re-entrant transition (from the collinear ferromagnetic state to the unmixed spin glass state) which, theoretically, is no longer thought to occur. The phases with broken symmetry are conjectured to be associated with irreversibilities and time effects, so that the properties of the system are intrinsically history dependent in those regions. However, because of the observed complexity of actual experimental systems, as well as the rather esoteric nature of the popular mean-field model descriptions (aside from the S-K solutions), the relevant connections between experiment and theory are not yet well understood. Indeed, the S-K solutions are presently the only ones capable of providing detailed quantitative predictions which can be tested experimentally. Furthermore, the excellent qualitative agreement between the S-K predictions and experiment indicates that the replica-symmetric solutions are worthy of further study.

Chapter 2

Apparatus and Sample Preparation

2.1 Apparatus for Magnetization and Susceptibility Measurements

2.1.1 The Theory and Operation of the RF SQUID

Superconducting QUantum Interference Devices (or SQUIDs) provide an extemely sensitive means of measuring changes in magnetic fields. They are ideal for studying very dilute magnetic alloys, which often create much weaker magnetic signals than can be detected effectively using more conventional techniques.

There are basically two types of SQUIDs. The D.C. SQUID uses a toroid of superconducting metal, with two Josephson junctions introduced into the loop. On the other hand, the RF SQUID is more common since it requires the use of only a single Josephson junction, and hence is easier to fabricate. As our SQUID systems were obtained commercially from the S.H.E. Corporation of San Diego and are of the RF variety, the following discussion pertains largely to these systems.

Superconductivity:

Cooper Pairs and the Meissner Effect

The electrical resistivity of normal electrical conductors arises from the scattering of conduction electron wavefunctions by the positively charged lattice ions. In between scattering events, the wavefunction is a plane-wave characterized by a particular phase angle $\alpha(\vec{r}) = \vec{p} \cdot \vec{r}$, where $\vec{p}$ is the electron momentum, and $\vec{r}$ is its position vector. Each time an interaction with the lattice occurs, the phase angle is changed and the coherence of the wavefunction (relative to its phase before the interaction) is lost. The average distance that the electrons can move through the lattice without losing coherence is known as the mean-free-path. However, if the lattice were perfectly periodic with no imperfections, impurities, or thermal vibrations, it can be shown that the mean-free-path of the electrons would become infinite and the electrical resistance would be zero. The above criteria cannot be fulfilled in real systems. Even so, many metals display a low temperature phase transition into a superconducting (that is, a zero resistivity) state.

When superconducting materials are cooled below some critical temperature T_c, their conduction electrons interact with the lattice in such a way that two electrons may experience a net mutual attraction, despite their strong Coulombic repulsion. As a result, some fraction of the electrons are forced to occupy electronic states in pairs, with the number of such pairs increasing as temperature approaches zero. These so-called *Cooper pairs* have zero net spin, and therefore behave as bosons of mass $m = 2m_e$ and charge $q = -2q_e$. Most importantly, the coherence of the pair wavefunction is preserved over laboratory-scale dimensions, so that a single well-defined phase angle $\theta(\vec{r})$ may be used to characterize

the pairs as they travel through the specimen. Hence, the pairs play the role of superconducting charge-carriers. As shown below, the coherence is very sensitive to applied magnetic fields, and leads to macroscopically observable quantum interference effects.

We may write the pair wavefunction as

$$\Psi = \rho^{1/2}\, e^{i\theta(\vec{r})} \quad ,$$

where $\rho = \Psi^{*}\Psi$ (assumed constant) is the number density of Cooper pairs, and $\vec{r}$ is the center of mass position of a pair. Under the influence of a magnetic field $\vec{B} = \vec{\nabla} \times \vec{A}$, the center of mass velocity of a pair (in CGS units) is given by

$$\vec{v} = \frac{1}{m}\left(-i\hbar\,\vec{\nabla} - \frac{q}{c}\vec{A}\right) \quad .$$

The super-current density is

$$\begin{aligned} \vec{j} &= q\Psi^{*}\vec{v}\Psi \\ &= \frac{\rho q}{m}\left(\hbar\,\vec{\nabla}\theta(\vec{r}) - \frac{q}{c}\vec{A}\right) \quad . \end{aligned} \tag{2.1}$$

Taking the curl of equation 2.1 yields the *second London equation*

$$\vec{\nabla} \times \vec{j} = -\frac{\rho q^2}{mc}\vec{B} \quad ,$$

which implies that within the superconducting specimen, the current density and magnetic field decrease exponentially with the distance from the surface. That

is,

$$\vec{B} = \vec{B_0}\, e^{-x/\lambda_L} \quad \text{and} \quad \vec{j} = \vec{j_0}\, e^{-x/\lambda_L} \quad ,$$

where $\lambda_L = \frac{c}{2q}\sqrt{\frac{m}{\rho\pi}}$ is the *London penetration depth.*

A strong superconductor has large ρ and small λ_L ($\sim .1\,\mu$m), so supercurrents circulate only within a thin surface layer of depth $\sim \lambda_L$. These currents spontaneously adjust so that the magnetic flux they create opposes and almost exactly cancels any other flux (from exterior sources) that is trapped deeper within the superconducting specimen. The expulsion of flux from the interior of a superconductor is known as the *Meissner effect.*

The Magnetic Flux through a Superconducting Toroid with a single Weak-link

A toroidal SQUID consists of a ring of strongly superconducting material ($T_c \simeq$ 4.2K) with a thin non-superconducting weak-link of length $2a$ and cross-sectional area σ. Consider a change in phase $\Delta\theta$ of the Cooper pairs as they travel around the ring along a contour C which, to avoid skin effects, is situated well below the surface. Using equation 2.1 gives (after Lounasmaa, 1974)

$$\begin{aligned} \Delta\theta &= \oint_C \vec{\nabla}\theta \cdot d\vec{l} \\ &= -\frac{m}{\hbar\rho\,|q|} \oint_C \vec{j} \cdot d\vec{l} - \frac{|q|}{\hbar c}\Phi \quad , \end{aligned} \tag{2.2}$$

where (by Stokes' theorem) the magnetic flux through the area enclosed by contour C is

$$\Phi = \oint_C \vec{A} \cdot d\vec{l} = \int_C \vec{B} \cdot d\vec{s} \quad .$$

Moreover, $\vec{B} = 0$ inside a superconductor and a is assumed very small, so that Φ effectively represents the flux through the hole in the toroid. As the wavefunction must remain single-valued, then $\Delta\theta = 2\pi n$ (n an integer). Rewriting equation 2.2 in terms of the *fluxon*, $\Phi_0 = \frac{2\pi\hbar c}{|q|} = 2.0678 \times 10^{-7}\text{Gauss} \cdot \text{cm}^2$, yields (after Lounasmaa, 1974)

$$\begin{aligned} \Delta\theta &= -\frac{m}{\hbar\rho\,|q|}\int_{-a}^{a} \vec{j} \cdot d\vec{l} - \frac{2\pi\Phi}{\Phi_0} \\ &= 2\pi n \quad , \end{aligned} \tag{2.3}$$

where $\vec{j} = 0$ has been used for deep within the superconductor.

Removing the weak-link by setting $a = 0$, we see that the flux Φ through the hole is then quantized in units of Φ_0. It is understood that Φ is made up of contributions from external magnetic field sources, as well as shielding super-currents which circulate (around the hole) along the inner surface of the toroid. That is,

$$\Phi = \Phi_{ext} + LI_S \quad , \tag{2.4}$$

where L is the self-inductance of the toroid, I_S is the shielding super-current, and Φ_{ext} is the external flux. The currents automatically compensate for changes in external flux to maintain Φ at an integer multiple of the fluxon. There is an upper limit to the magnitude of the shielding current, but it is only reached for external

fields greater than those encountered in normal SQUID operations.

On the other hand, when a very small non-zero value of a is chosen, the Cooper pairs may quantum tunnel through the non-superconducting barrier, giving a non-zero contribution to $\vec{j}$ along the contour C. Therefore, the weak-link plays the part of a Josephson junction and, as shown below, serves to substantially limit the maximum amount of super-current which can circulate around the ring.

The super-current through the weak-link is

$$\begin{aligned} I_S &= \sigma j \\ &= -\frac{|q|\,\hbar\sigma}{2mi}\left(\Psi^*_{wl}\,\vec{\nabla}\Psi_{wl} - \Psi_{wl}\,\vec{\nabla}\Psi^*_{wl}\right) \quad , \end{aligned}$$

where Ψ_{wl} is the Cooper pair wavefunction within the weak-link. To evaluate Ψ_{wl} we consider the tunneling of the wavefunctions

$$\begin{aligned} \Psi_1 &= \rho^{1/2}\, e^{i\theta_1} \\ \text{and} \quad \Psi_2 &= \rho^{1/2}\, e^{i\theta_2} \end{aligned}$$

(on either side of the weak-link) through the barrier. It is straight-forward to show that the wavefunctions decay exponentially upon entering the non-superconducting region, and (after Lounasmaa, 1974)

$$\Psi_{wl} = \rho^{1/2}\, e^{i\theta_1}\, \exp\left\{\frac{-(l+a)}{\lambda}\right\} + \rho^{1/2}\, e^{i\theta_2}\, \exp\left\{\frac{l-a}{\lambda}\right\} \quad .$$

(The constant λ is a characteristic of the weak-link.) Thus,

$$I_S = -\frac{|q|\,\hbar\sigma}{m}\frac{2\rho}{\lambda}\exp\left\{-\frac{2a}{\lambda}\right\}\left[\frac{e^{i(\theta_2-\theta_1)}-e^{-i(\theta_2-\theta_1)}}{2i}\right] \quad .$$

That is, the tunneling current depends periodically on the difference in the phases of the wavefunctions on either side of the weak-link. From equation 2.3 we can relate this quantum interference to the flux through the hole:

$$\Delta\theta = (\theta_2-\theta_1) - \frac{2\pi\Phi}{\Phi_0} = 2\pi n \quad .$$

Therefore (after Lounasmaa, 1974),

$$I_S = -I_c \sin\left\{\frac{2\pi\Phi}{\Phi_0}\right\} \tag{2.5}$$

$$\text{with} \quad I_c = \frac{2\,|q|\,\hbar\sigma\rho}{m\lambda}\exp\left\{-\frac{2a}{\lambda}\right\} \quad .$$

I_c is the maximum (or critical) super-current which can tunnel through the weak-link, and is typically $\sim$ 1 to 100 μA.

Equations 2.4 and 2.5 yield

$$\Phi = \Phi_{ext} - LI_c \sin\left\{\frac{2\pi\Phi}{\Phi_0}\right\} \quad .$$

The flux through the hole oscillates sinusoidally about the straight line $\Phi = \Phi_{ext}$, with an amplitude LI_c and period Φ_0. Though the period is common to all

SQUIDs, the slope is not (after Lounasmaa, 1974):

$$\frac{d\Phi}{d\Phi_{ext}} = \left[1 + \frac{2\pi L I_c}{\Phi_0} \cos\left\{\frac{2\pi\Phi}{\Phi_0}\right\}\right]^{-1} \quad .$$

For the strongly superconducting case, $\frac{2\pi L I_c}{\Phi_0} > 1$, unstable regions of negative slope occur. As shown in Figure 2.1, Φ initially increases slowly as Φ_{ext} is increased from zero, due to the strong shielding currents which begin to circulate around the ring. As the super-current approaches the weak-link critical value I_c, the shielding becomes less effective until, at point P (where $\frac{d\Phi}{d\Phi_{ext}} \rightarrow \infty$), Φ jumps discontinuously to point Q. In other words, since I_c cannot be exceeded, a flux jump occurs to reset I_S at a value well below I_c. Similar flux jumps occur as Φ_{ext} is decreased, though Φ then follows a different path. Practical RF SQUID systems exploit this hysteretical behavior to good effect.

The Staircase Pattern

Operationally, the SQUID toroid is coupled inductively (via the *RF coil* of inductance L_{RF}) to an LCR resonant circuit. This circuit is, in turn, loosely coupled (via a capacitor $C_{RF\,level}$) to an RF sinusoidal signal generator which drives the circuit at a resonant frequency of $19 \pm .5$ MHz (Figure 2.5). The tuning may be adjusted with the variable capacitor C_{tune}, while the amplitude (or RF level) of the RF oscillations is adjusted via a variable attenuator.

The SQUID toroid and resonant circuit are sealed within a S.H.E. model MFP multifunction cryogenic probe, which functions from 0 to 5K (optimally 4.2K). The RF signal generator is contained within a S.H.E. model 300 RF Head,

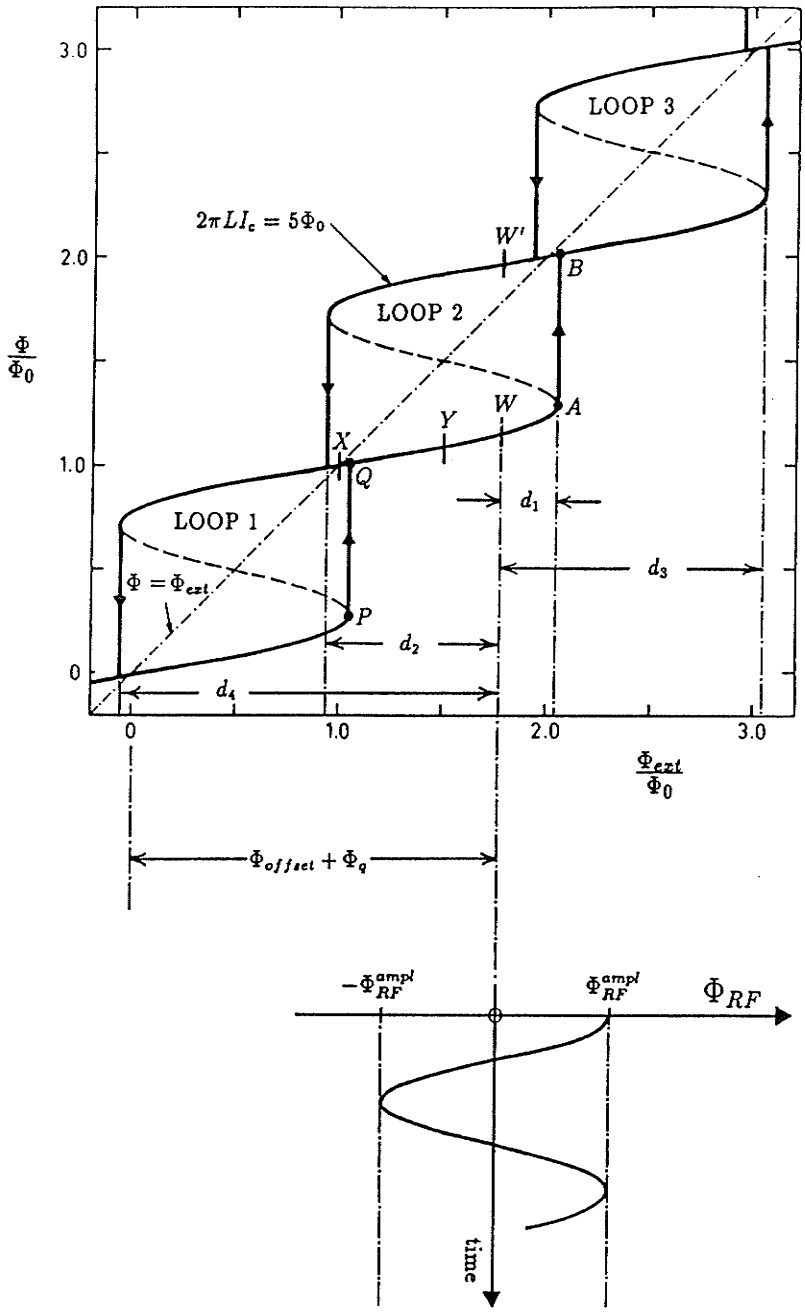

Figure 2.1: The dependence of the flux Φ, through the SQUID toroid, on the external flux Φ_{ext}. The sinusoidal flux oscillation Φ_{RF} is used to drive Φ around hysteresis loops, and Φ_q represents the flux due to the magnetic specimen to be studied.

while the tune and RF level are controlled from a S.H.E. model 30 SQUID control unit.

Now the external flux can be written as

$$\Phi_{ext} = \Phi_{offset} + \Phi_q + \Phi_{RF} \quad ,$$

where Φ_{RF} is the flux (through the hole) due to the RF signal, Φ_{offset} is a manually adjustable constant offset, and Φ_q is a quasi-static flux which changes very slowly relative to Φ_{RF}. Actually, Φ_q represents the flux created by the magnetic specimen to be studied, and is coupled into the SQUID via a *flux transformer*. The details of the sample arrangement are discussed later. Together, Φ_{offset} and Φ_q determine the *working point* W of the SQUID.

Consider an arbitrary working point W as shown in Figure 2.1. We may increase the amplitude Φ_{RF}^{ampl} of the Φ_{RF} oscillations by increasing the RF level. Several cases are of importance:

In the range $0 < \Phi_{RF}^{ampl} < d_1$, the flux Φ oscillates reversibly along the curve about the point W. However, when $d_1 \leq \Phi_{RF}^{ampl} < d_2$, a flux jump (from A to B) occurs, and the oscillations proceed reversibly about the new effective working point W'. The amplitude V_{RF}^{ampl}, of the RF voltage V_{RF} across the tuned circuit, increases linearly from 0 to $V_{RF}^{d_2}$ with the RF level (Figure 2.2).

When $d_2 \leq \Phi_{RF}^{ampl} < d_3$, Φ is driven counter-clockwise around a hysteresis loop (Loop 2). The corresponding energy absorbed from the tuned circuit is proportional to the area of the loop, and is manifest as a dramatic decrease in V_{RF} from its value of $V_{RF}^{d_2}$ just before the lossy cycle took place. At relatively low RF levels, the tuned circuit is weakly coupled to the RF signal generator, and

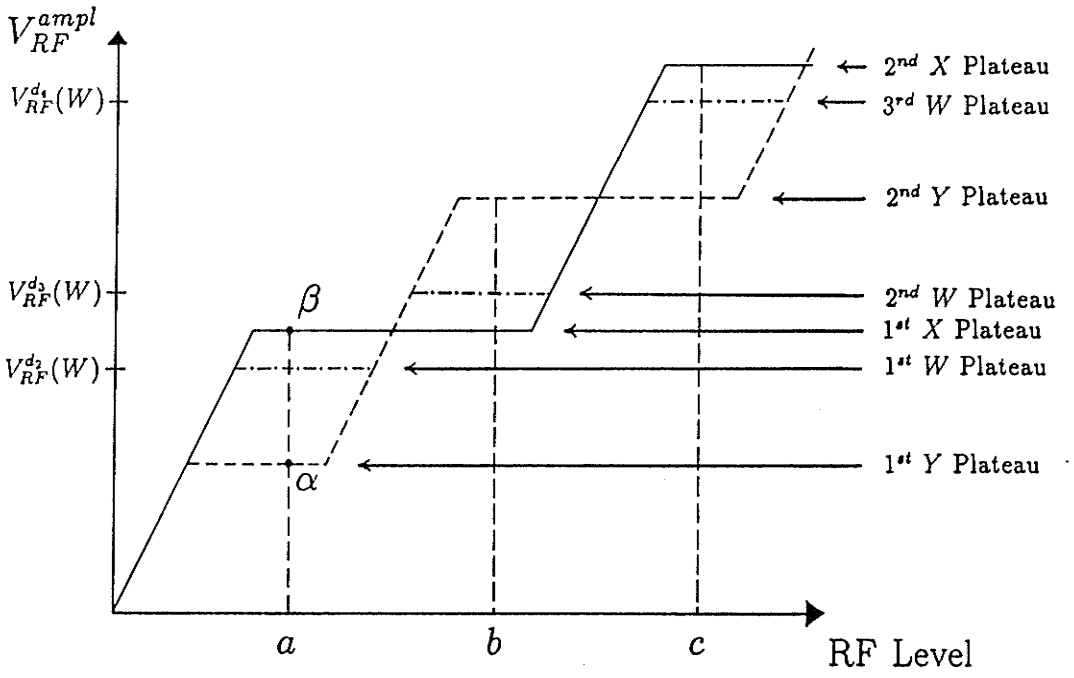

Figure 2.2: The staircase pattern. The RF levels a, b, and c optimize the amplitude of the triangle pattern of Figure 2.4.

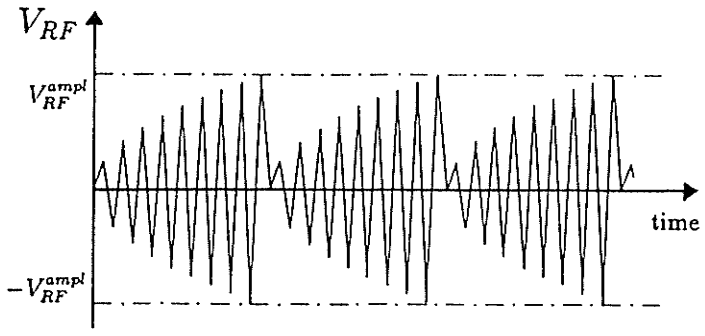

Figure 2.3: The modulation of V_{RF} with time. Whenever Φ is driven around a hysteresis loop, the amplitude decreases rapidly from V_{RF}^{ampl} to 0. The rate of the subsequent energy build-up depends on the RF level (after Lounasmaa, 1974).

a finite amount of time is required to overcome the damping of V_{RF} and gather enough energy for another lossy cycle to occur. Therefore, V_{RF} is modulated in time (Figure 2.3). The rate of energy build-up, and hence the frequency of the modulation, can be increased via the RF level. However, Φ_{RF}^{ampl} and V_{RF}^{ampl} will not exceed d_2 and $V_{RF}^{d_2}$, respectively, until the modulation frequency matches the RF frequency (that is, until one lossy cycle occurs for every V_{RF} oscillation — the maximum rate possible). Thus, the graph of V_{RF}^{ampl} versus RF level (Figure 2.2) shows a plateau of constant voltage $V_{RF}^{d_2}$. Once the RF level is high enough to completely compensate for the hysteretical losses, further increases enable V_{RF}^{ampl} to grow linearly from $V_{RF}^{d_2}$ to $V_{RF}^{d_3}$, and Φ_{RF}^{ampl} to vary from d_2 to d_3.

In the range $d_3 \leq \Phi_{RF}^{ampl} < d_4$ there occurs another plateau, corresponding to $V_{RF}^{ampl} = V_{RF}^{d_3}$. Here Φ is driven around <u>two</u> hysteresis loops (Loop 2 and Loop 3) during each lossy cycle. Once again the plateau ends when the RF level is high enough that the rate of hysteretical energy dissipation is matched by the rate of energy build-up in the tuned circuit. At the end of the plateau, V_{RF}^{ampl} rises linearly from $V_{RF}^{d_3}$ to $V_{RF}^{d_4}$.

Lastly, for $\Phi_{RF}^{ampl} \geq d_4$, plateaus occur ad infinitum, and correspond successively to transits of 3,4,5,... loops per lossy cycle. As illustrated in Figure 2.2, the result is a staircase-like pattern.

The location of the working point W (Figure 2.1) is such that the loop pattern is not symmetric about it. That is, $d_1 \neq d_2$ and $d_3 \neq d_4$, therefore two step heights (Figure 2.2) are associated with W. However, if we move the working point to position X or Y in Figure 2.1, then the symmetry of the loop pattern results in only one step height for the corresponding staircase pattern.

The plateaus for X correspond to transits of even numbers of hysteresis loops per lossy cycle, while those for Y correspond odd numbers of loops. The staircase patterns for all other working points fall between these two limiting cases.

The Triangle Pattern

Experimentally we are interested in measuring changes in the quasi-static flux Φ_q, which represents the magnetic signal of our dilute magnets. The variation of V_{RF}^{ampl} with the working point (for fixed RF level) must be determined.

Say we choose the RF level represented by the vertical line a in the middle of the first plateau region (Figure 2.2), and start at the working point X (Figure 2.1). Sliding the working point over from X to Y, the external flux Φ_{ext} increases by $\Phi_0/2$, and V_{RF}^{ampl} decreases linearly from point β to point α. Like-wise, by sliding the working point from Y to A, the external flux increases by $\Phi_0/2$, while V_{RF}^{ampl} increases linearly from point α to point β. Obviously, a plot of V_{RF}^{ampl} versus working point yields a triangular waveform with a period equal to the fluxon Φ_0 (Figure 2.4). This non-linear relation is the basis of all SQUID measurements.

The peak-to-peak amplitude V_Δ is a function of the RF level and is maximized ($V_\Delta \sim 60$ milli-Volts) around the lines a, b, c, etc. Any of these RF levels can be used, though the lowest RF level (line a) is most convenient and sometimes provides the best signal-to-noise ratio.

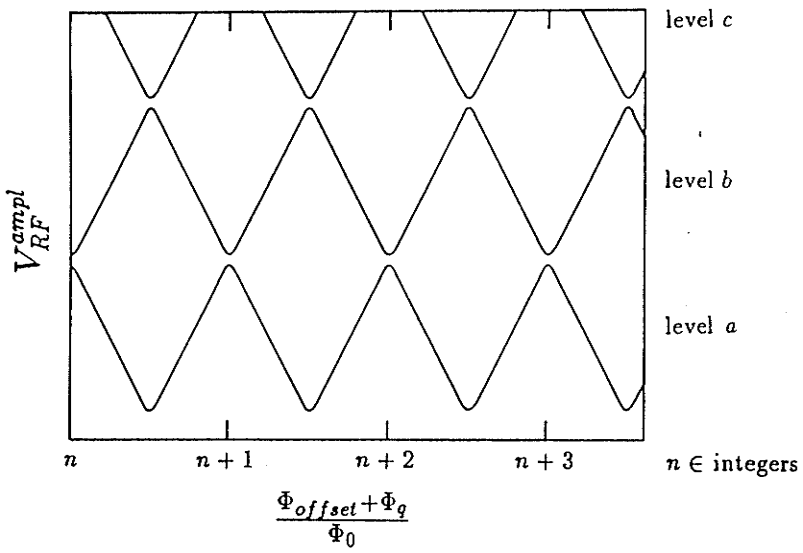

Figure 2.4: The triangle pattern.

The RF SQUID Magnetometer

The RF SQUID can be used directly for measuring the magnetization of a specimen, simply by noting the non-linear variation of V_{RF}^{ampl} as Φ_q changes with time. However, as this is awkward, a *Flux Locked Loop* is utilized to convert the signal into one which varies linearly with Φ_q. The components of the loop are contained within the model 30 SQUID control unit, and shown schematically in Figure 2.5.

The SQUID flux is oscillated about an average value (represented by the point W in Figure 2.1) by an audio (50 kHz) square wave with a peak-to-peak amplitude of $\frac{\Phi_0}{2}$. The amplitude is adjusted via the MOD control on the control unit. The idea is to *lock* the system into a particular triangle valley (the bottom of which is represented by the point V) by means of an appropriate feedback flux Φ_{fb}.

The error parameter $\delta\Phi$ indicates the flux difference between points W and V. Necessarily, $\delta\Phi < \frac{\Phi_0}{4}$, otherwise the audio flux oscillations will carry the system into another valley. As shown in Figure 2.6, the resulting time dependence of V_{RF}^{ampl}, for a particular value of $\delta\Phi$, is essentially an audio square wave $V_{AF}(t)$ with the same period as the flux oscillation. It can be shown that the peak-to-peak amplitude of $V_{AF}(t)$ is proportional to $\delta\Phi$. Of course, $V_{AF}(t)$ is modulated as $\delta\Phi$ changes with time, and an amplified version of this waveform is output from the detector D_1.

The phase difference between $V_{AF}(t)$ and the original flux oscillation is either 0 or π, depending on whether W is located to the right or left (respectively) of point V. Hence, the output of the phase sensitive detector D_2 is a positive or negative D.C. signal proportional to that required to return the average flux to

point V. After appropriate scaling and phase shifting (via an integrator), this signal is fed back into the SQUID by means of the RF coil. The resulting feedback flux Φ_{fb} cancels changes in Φ_q to within $\frac{\Phi_0}{4}$, and keeps the system locked within the chosen valley. The feedback voltage varies linearly with the magnetization of the sample, and is read via a Racal-Dana model 5003 digital voltmeter.

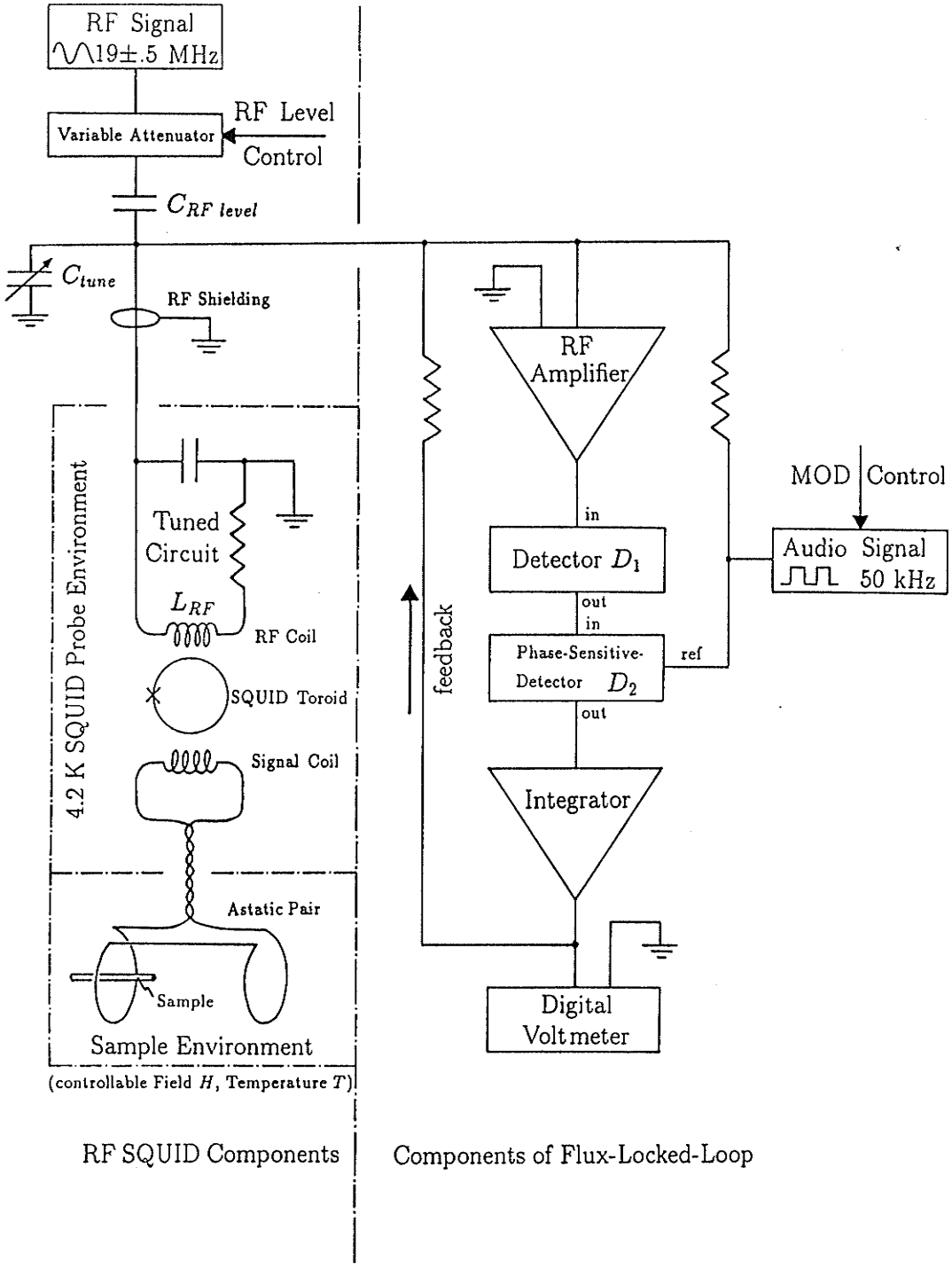

Figure 2.5: The RF SQUID Magnetometer.

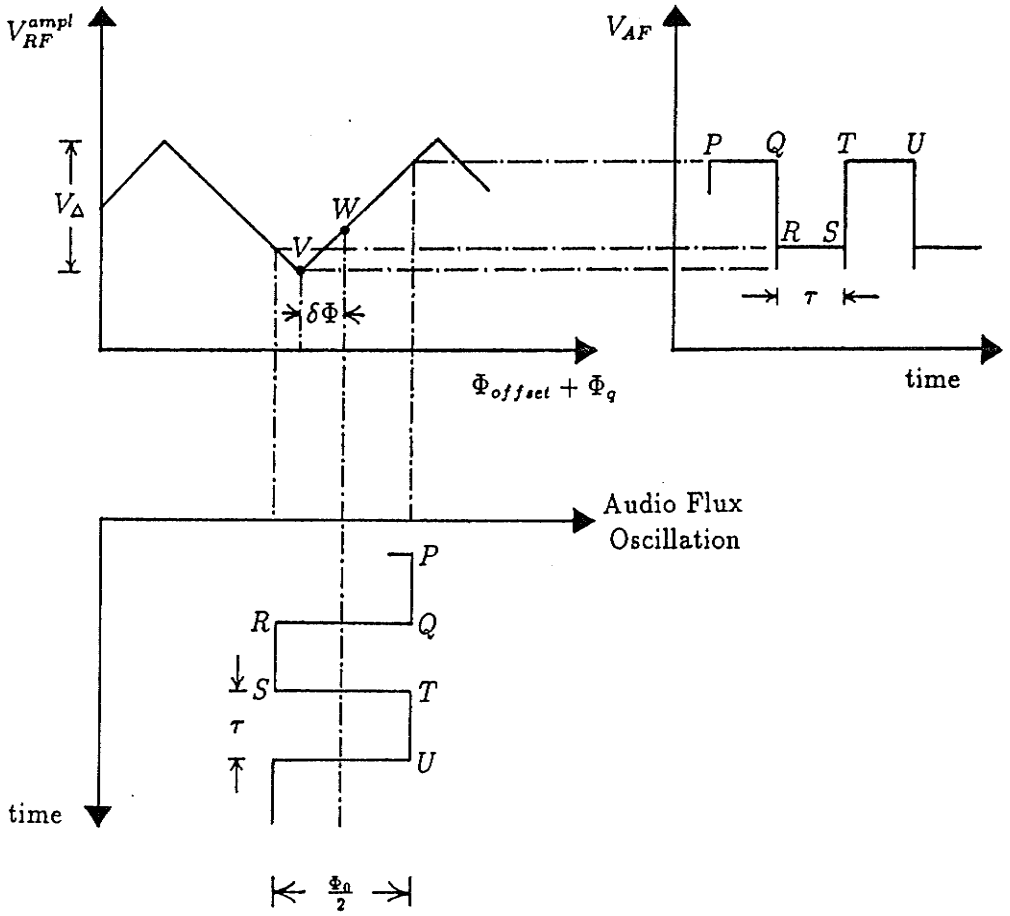

Figure 2.6: The Flux-Locked-Loop uses the phase difference between V_{AF} and the audio flux oscillation to lock the SQUID onto a particular triangle valley V.

The Flux Transformer

In utilizing the SQUID as a magnetometer, it is impractical to place the magnetic specimen directly within the superconducting toroid. The use of a *flux transformer* allows the specimen and the SQUID proper to be separated physically, and placed in different field and temperature environments. The latter is especially important since the SQUID probe will not function at temperatures above 5 K. A flux transformer generally has three basic components; the pickup coils, a signal coil, and the leads between them.

The pickup coils consist of two coils which are wound, with the same number of turns, on opposite ends of a cylindrical spool. The coils are wound in opposite directions, connected in series, and carefully constructed to have nearly identical dimensions. The two leads from the pickup coils are joined, by means of superconducting wire, to the leads of a superconducting signal coil which is coupled inductively to the SQUID toroid (Figure 2.5). To minimize the pickup of noise, the connecting wires are tightly twisted around each other, or enclosed in a superconducting tube.

The pickup coils form the arms of an astatic pair. When both arms are exposed to exactly the same magnetic field, the currents induced in each arm cancel each other exactly (assuming perfect coil geometry), and the net current through the circuit is zero. However, by placing a magnetic specimen within only one arm, a non-zero current (which varies linearly with the sample magnetization) is set up within the pair. This current also flows through the signal coil so that the magnetic signal of the sample is transferred into the SQUID, and measured as the quasi-static flux Φ_q.

Either a solenoid or a Helmholtz pair is used to apply a D.C. magnetic field to our samples. With proper coil geometry and positioning, the D.C. field is the same for both arms of the astatic pair and only the sample magnetization, not the D.C. field, is measured. Also, since our samples are maintained at cryogenic temperatures for the duration of the measurements, the use of superconducting pickup coils is made possible. Section 2.1.2 provides the design details for the D.C. field coils and pickup coils.

The RF SQUID A.C. Susceptometer

The electronic components of our susceptometer were obtained from the S.H.E. Corporation of San Diego, and consist of a model RBU Precision Low-level A.C. Impedence Bridge Unit, a model BPD Bi-Phase Detector, plus the components of the RF SQUID magnetometer. These are shown schematically in Figure 2.7.

In the susceptometer configuration, the pickup coils play the part of the secondary in a mutual inductor M. As usual, the sample is inserted into one arm of the astatic pair, and its temperature and D.C. magnetic field environment are adjusted as desired. The primary coil, which is wound co-axially about the secondary and close-coupled (through resistor R_M) to a sinusoidal signal generator, creates the driving field. The signal generator provides an A.C. voltage v_{excite} of selectable angular frequency ω. Like the D.C. field coils, the primary coil is designed and positioned such that the driving field itself is not detected by the astatic pair. The designs of the various coils are provided in Section 2.1.2.

In general, the A.C. susceptibility of a magnet has both real and imaginary parts:

$$\chi_{ac} = \chi' + i\chi'' \ .$$

The real component χ' is in phase with the magnetic field produced by the primary coil, and effectively represents the zero-frequency susceptibility. On the other hand, χ'' is $\pi/2$ out of phase (or in quadrature) with the driving field, and represents a frequency-dependent energy dissipation. It can be shown that M is also a complex quantity, with components M' and M'' proportional to χ' and χ'', respectively.

Mode	M' $\left[\frac{\Omega\cdot\text{sec}}{\text{radian}}\right]$	M'' $\left[\frac{\Omega\cdot\text{sec}}{\text{radian}}\right]$
Multiply	$10^{-6}\,\lambda\alpha$	$-10^{-9}\,\lambda\beta\omega$
Divide	$10^{-6}\,\frac{\alpha}{\lambda}$	$-10^{-9}\,\frac{\beta\omega}{\lambda}$

Table 2.1: The relationships between the bridge balance conditions and the in-phase and quadrature components of M.

The model RBU bridge is used to measure M' and M'', and operates as follows. The secondary of M is connected in series with the secondary of a fixed mutual inductance m (which is sealed within the multifunction SQUID probe). Two ratio transformers are used to tap voltages αv_{excite} and βv_{excite} from the signal generator. The component αv_{excite} is close-coupled (through resistor R_m) to the primary of m, and is in phase with the voltage across the primary of M (actually, use of the Forward/Reverse switch, which reverses the polarity of the signal, may be required to obtain phase matching). The component βv_{excite} is loosely coupled (through capacitor C_m) to the primary of m, and provides a quadrature signal. An additional ratio transformer is used to either multiply or divide α and β by an amount λ.

The idea is to adjust α, β, and λ until the emf induced in the secondary of m exactly balances the emf induced in the secondary of M. In this respect, the RF SQUID magnetometer is used as a sensitive null-current detector by placing the signal coil in series with the secondary coils. A bi-phase detector is required to measure separately the in-phase and quadrature components of the current between the secondaries, as both must be nulled for true balance to occur. Table 2.1 shows how M' and M'' are related to ω and the balance values of α, β, and λ.

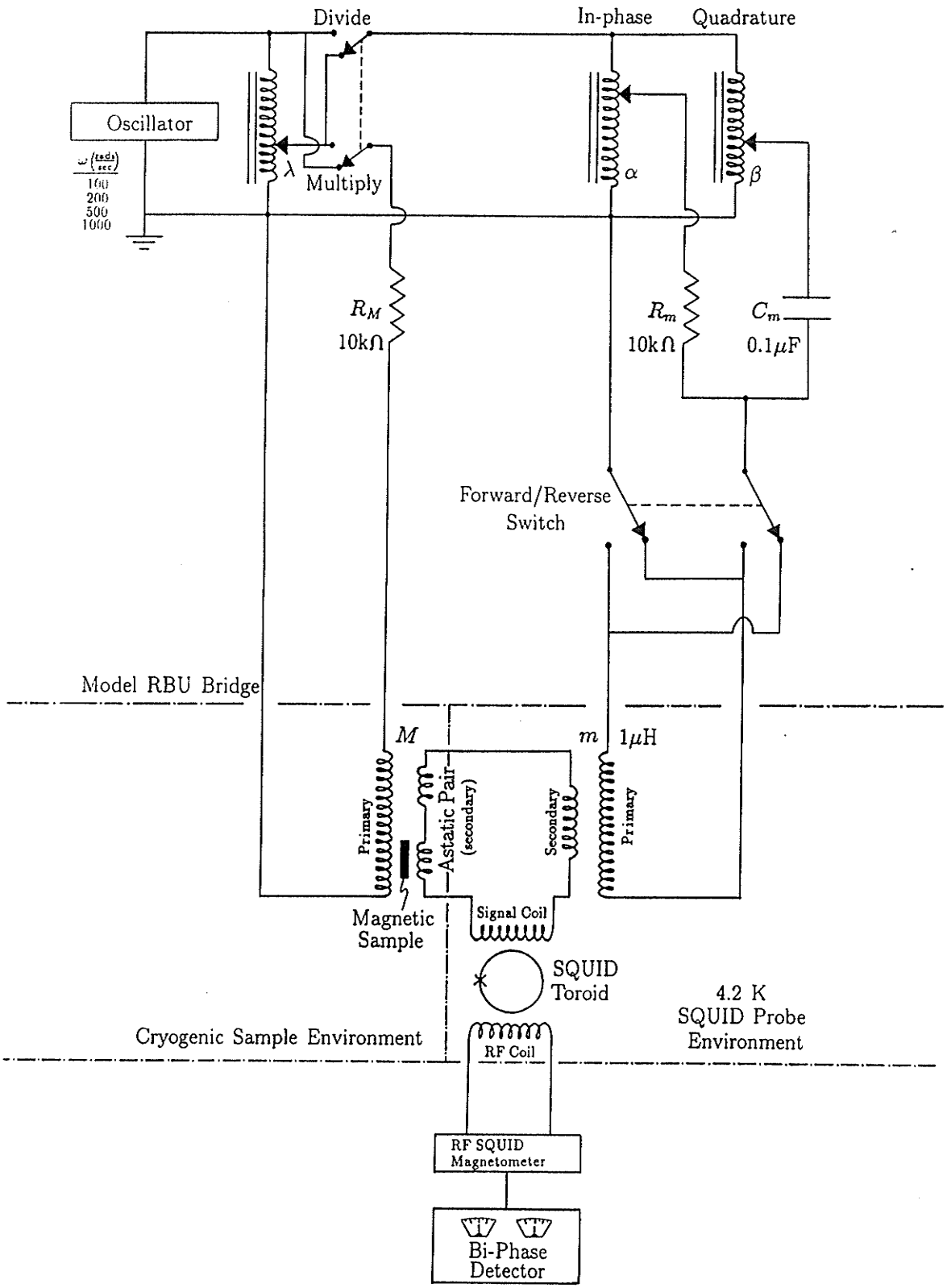

Figure 2.7: The RF SQUID Susceptometer.

2.1.2 Cryogenic Sample Environments

The weak magnetic nature of our dilute alloy samples requires the use of cryogenic techniques to maintain them at low temperatures. Two different systems are used; a He^3–He^4 dilution refrigerator purchased from the S.H.E. Corporation, and a home-made He^4 cryostat. The dilution refrigerator is operated in conjunction with an RF SQUID magnetometer, while the cryostat is used together with an RF SQUID in an A.C. susceptometer configuration. The general layout and operation of these two systems is documented below.

The Dilution Refrigerator/Magnetometer

At low temperatures, the helium isotopes He^3 and He^4 are both liquid, even near absolute zero. The normal boiling point of He^4 is 4.2 K, but the temperature of such a bath may be reduced to $\sim$ 0.9 K by pumping on its vapour (due to the latent heat of evaporation). Similarly, the normal boiling point of He^3 is 3.7 K, and its bath temperature may be reduced to as low as $\sim$ 0.3 K through vigorous pumping.

Even lower temperatures are obtainable when a liquid mixture of He^3 and He^4 is considered. Figure 2.8 shows the phase diagram for such a mixture. Because the He^3 and He^4 atoms are fermions and bosons, respectively, their low temperature behavior differs considerably. Above 0.86 K, the fluid is a homogenous mixture of the two isotopes, and has either normal or superfluid (i.e. zero viscosity) properties, depending on whether the concentration of He^3 is to the right or left of the λ-curve. At lower temperatures, the mixture begins to separate into two distinct phases. One phase is a normal fluid and is rich in He^3; the

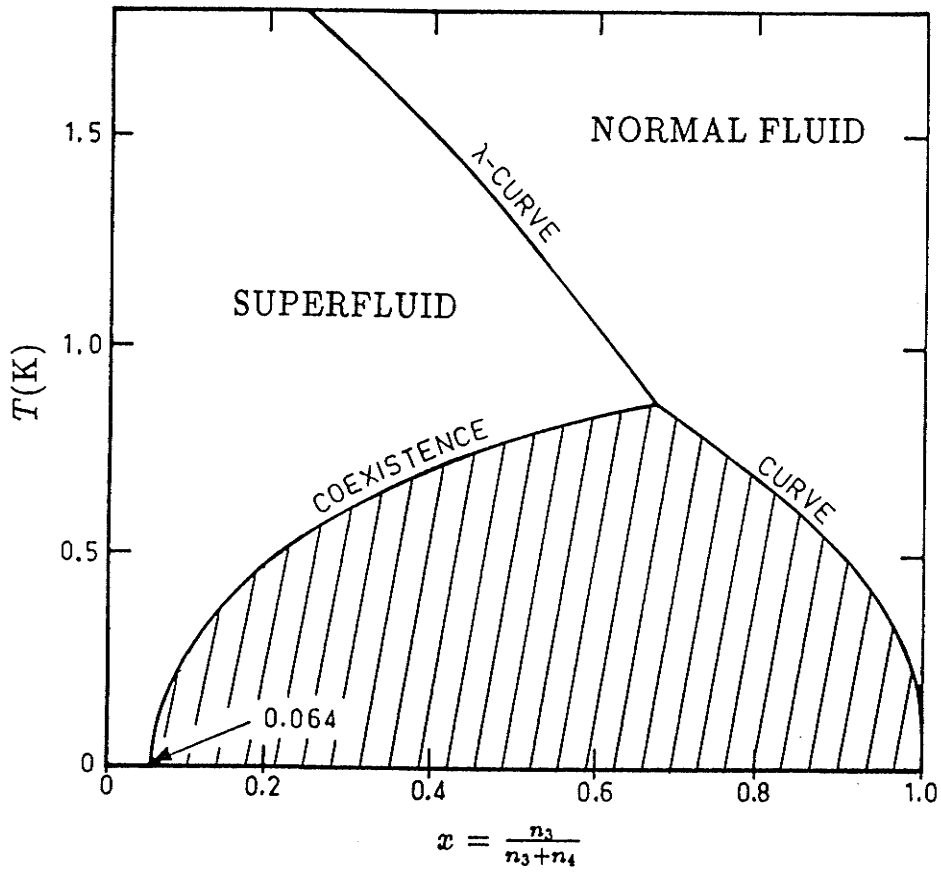

Figure 2.8: The He^3-He^4 phase diagram. The quantity x represents the fractional concentration of He^3 atoms in the fluid mixture. Below 0.86 K the mixture spontaneously separates into two distinct phases. As $T \rightarrow 0$ K, one phase consists entirely of normal fluid He^3, while the other phase is mostly superfluid He^4, but with a finite concentration ($x = 0.064$) of He^3 atoms (after Lounasmaa, 1974).

He^3 atomic concentration approaches 100% as the temperature approaches absolute zero. The other phase is a He^4–rich superfluid. However, even at absolute zero, the He^4–rich phase is a dilute solution with more than 6 at. % He^3.

The He^3–rich phase floats on top of the He^4–rich phase, due to their differing densities. Since the He^4–rich phase is superfluid, the dissolved He^3 atoms behave much like gas atoms in a vacuum. If He^3 atoms are somehow removed from the solution, they are immediately replaced by by He^3 atoms which cross over the phase boundary from the He^3–rich phase. There is a latent heat involved which is analogous to that of liquid evaporation. As a result, it is possible to cool the fluids down to temperatures of tens of milli-Kelvin. Our dilution refrigerator operates by this principle, but continuously cycles the He^3 atoms in a closed loop so that cooling can occur over long periods of time.

A schematic of our S.H.E. model DRI-236 Dilution Refrigerator Cryostat, along with its Pumping and Gas Handling system, is shown in Figure 2.9. To thermally isolate the cryogenic core of the refrigerator from room temperature, it is situated within a high-vacuum can immersed in a He^4 bath. The can is evacuated to $\sim 10^{-5}$ Torr by means of a Sargent Welch 1402 mechanical pump and an oil diffusion pump. Our system uses a mixture of approximately 30% He^3 and 70% He^4. As shown in Figure 2.10, the major components of the core are the cold-plate, the still, the continuous heat exchanger, the six step heat exchangers, and the mixing chamber. Most of the components are constructed from copper, since it provides high thermal conductivity.

The copper cold-plate contains a small chamber into which liquid He^4 is drawn from the bath through a capillary. Pumping on the chamber (with a

Sargent Welch 1374 mechanical pump) cools the cold-plate down to about 1 K. The heater on the plate is used only during a preliminary *bake-out* procedure, in which He^4 exchange gas (used to thermally couple the core to the He^4 bath) is evacuated from the vacuum can. A Speer carbon resistor (nominally 100Ω) is used to measure the approximate temperature of the plate.

During operation, the copper still contains a non-phase-separated mixture of superfluid He^3–He^4. A heater preferentially boils off the lighter He^3, and the vapour is pumped on through a specially designed orifice which restricts the escape of He^4. The still temperature is monitored with a calibrated carbon resistor, and is optimally 0.7 K. However, our system seems to run slightly hot, as the resistor indicates an operating temperature of about 0.8 to 0.95 K.

The copper mixing chamber, where the actual phase separation occurs, is lined with sintered copper to enhance thermal contact with the cold liquid. Warm liquid He^3 flows into the mixing chamber through a tube, and continually replenishes the He^3–rich phase. Simultaneously, He^3 atoms (from the He^3–rich phase) are drawn across the phase boundary, and removed from the chamber via a tube flooded with He^4–rich superfluid (more about this later).

Each of the six step heat exchangers is constructed from two short copper tubes which are welded together length-wise and packed with sintered copper. The mixing chamber's warm incoming He^3 flows through one tube, while the out-going cold fluid flows through the other.

In the continuous heat exchanger, the warm He^3 line is threaded through the cold line to place it in direct contact with the out-going cold fluid.

The closed-cycle operation of the core is as follows. For convenience we

shall assume that the circulating medium is entirely He^3, though there is a small amount of He^4 which escapes through the orifice in the still. An Edwards model 660 sealed mechanical pump is used to circulate the He^3 through the core.

Gaseous He^3 is first cooled to 4.2 K by the He^4 bath. Upon entering the vacuum can, the gas is liquefied by passing it through a condenser (placed in thermal contact with the 1 K cold-plate) and a flow impedence. After further cooling by means of the still heat exchanger and the continuous and step heat exchangers, the liquid He^3 enters the mixing chamber.

The out-going cold line (from the mixing chamber) passes back through the step and continuous heat exchangers, and opens into the superfluid bath in the still. In this way, the mixing chamber and the still are connected by an unbroken column of He^4–rich superfluid. By pumping on the still, the concentration of dissolved He^3 at the top of the column is made to be lower than that at the bottom. The resulting osmotic pressure gradient (see Lounasmaa, 1974) draws He^3 atoms across the phase boundary in the mixing chamber, and up into the still. Subsequently, He^3 vapour from the still is recirculated into the core by means of the sealed mechanical pump at room temperature.

The system is potentially capable of cooling the mixing chamber to approximately 30 mK. However, our refrigerator is in need of fine tuning, and is only able to reach about 50 mK. Stabilization at higher temperatures requires the use of a heater and a carbon resister (both in good thermal contact with the mixing chamber), together with a feed-back system (see Figure 2.12). The temperature stability is 5×10^{-4} K at 50 mK, and 5×10^{-3} K at 800 mK (after Yeung, 1988).

The sample environment is shown in Figure 2.11. The copper sample cham-

ber/holder is bolted in good thermal contact with the mixing chamber, and a calibrated germanium resistor (model GR-200A-30 from Lake Shore Cryotronics of Westerville, Ohio), together with a S.H.E. model PCB Potentiometric Conductance Bridge, is used for precision temperature determination (see Yeung, 1988). The sample is attached to the holder with G.E. varnish, and postioned half-way into the lower pickup coil.

The pickup coils for the magnetometer are made of 0.007″ superconducting Niobium-Titanium wire, and counter-wound (9 turns each) on a spool machined from Emerson and Cuming Stycast 1266 epoxy. The coils have a radius of 0.170″ and a center-to center separation of 0.750″. The leads of the pickup coils are connected to the appropriate terminals on the cryogenic SQUID probe, and enclosed by superconducting PbSn tubing to shield them from noise.

A uniform and highly stable D.C. magnetic field is applied to the sample by means of a Helmholtz pair (mounted outside the vacuum can) and a constant current source with a maximum 1 ampere capability (see Yeung, 1988). Each coil consists of 650 turns of 31-guage copper wire. The pair has a mean coil radius and separation distance of 6.033 cm, and delivers 96.81 gauss per ampere at its center.

To help reduce noise in the SQUID due to relative motion between the sample and the pickup coils, measures are taken to isolate the cryostat from vibration. The vibration of the mechanical pumps is decoupled from the cryostat by means of flexible bellows on the pumping lines. In addition, the cryogenic core and the entire dewar assembly are supported by a sturdy plywood bridge which rests on massive sand foundations.

Our refrigerator/magnetometer is capable of measuring the magnetization of the sample as a function of temperature, applied magnetic field, and time. The magnetometer is not calibrated, however, so that the changes in the sample magnetization are measured in arbitrary units.

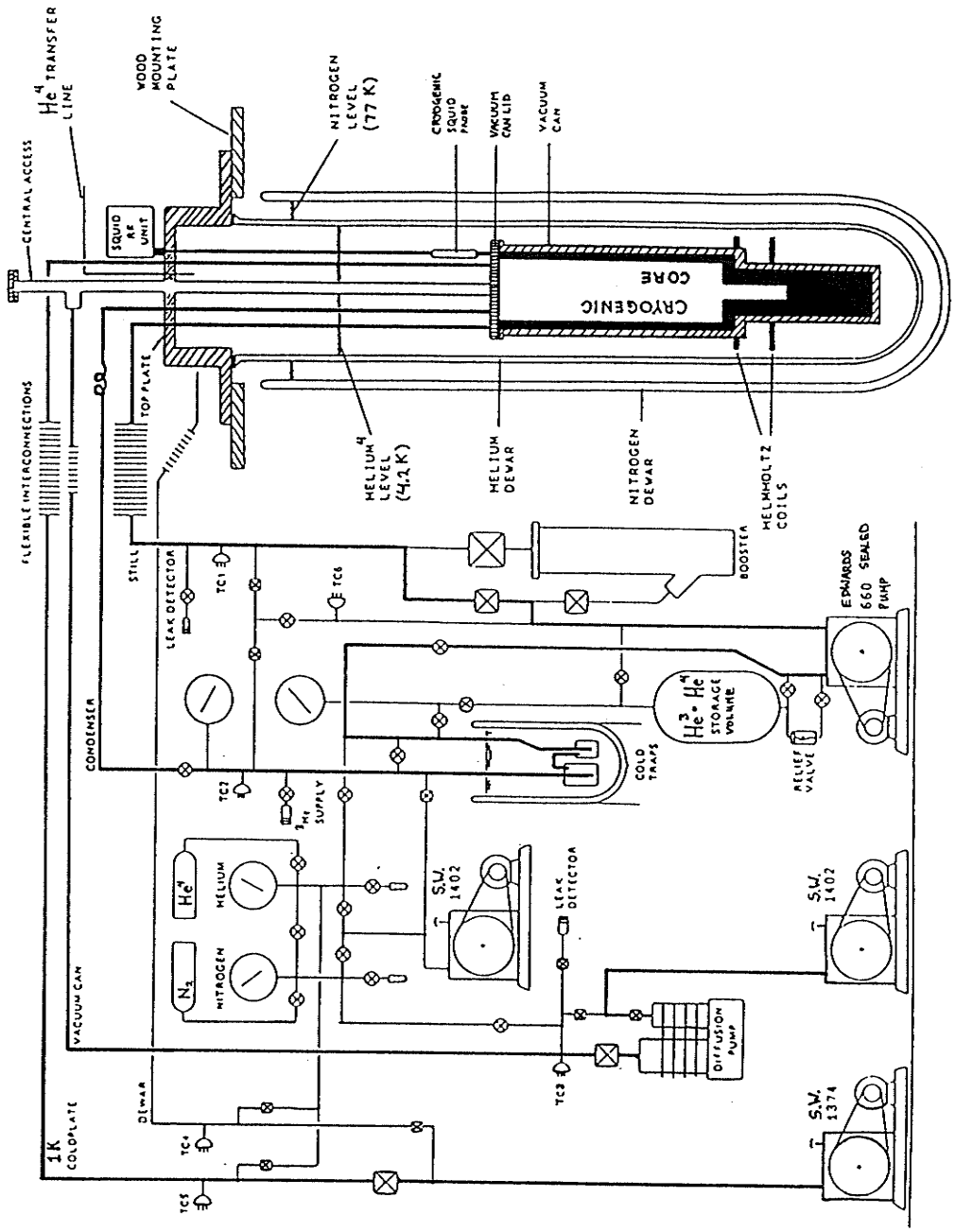

Figure 2.9: The Pumping and Gas Handling System (after S.H.E. Corporation).

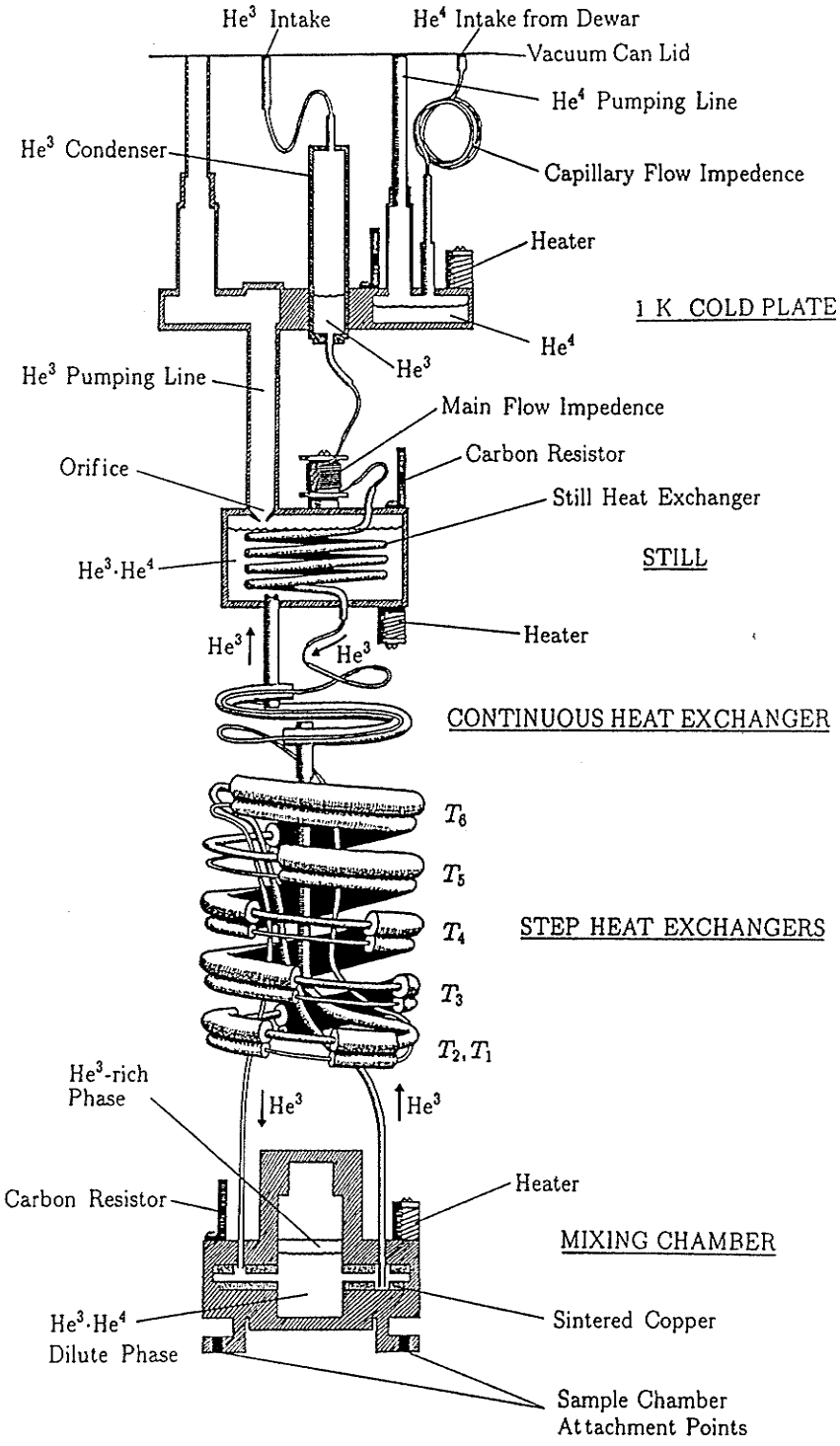

Figure 2.10: A schematic diagram of the dilution refrigerator cryogenic core. The entire assembly is $\sim$ 33 cm in length.

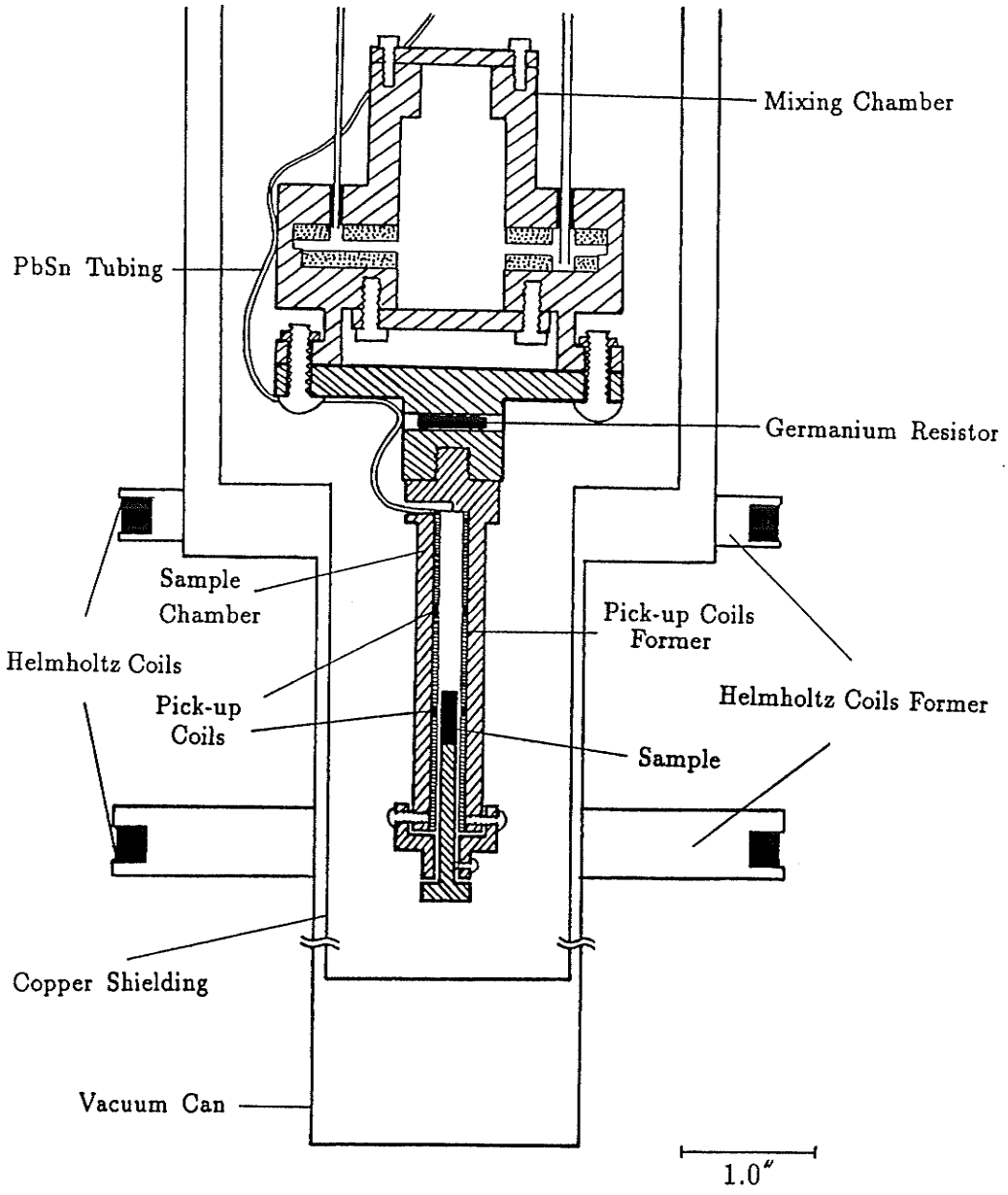

Figure 2.11: The sample environment of the magnetometer (after Yeung, 1988).

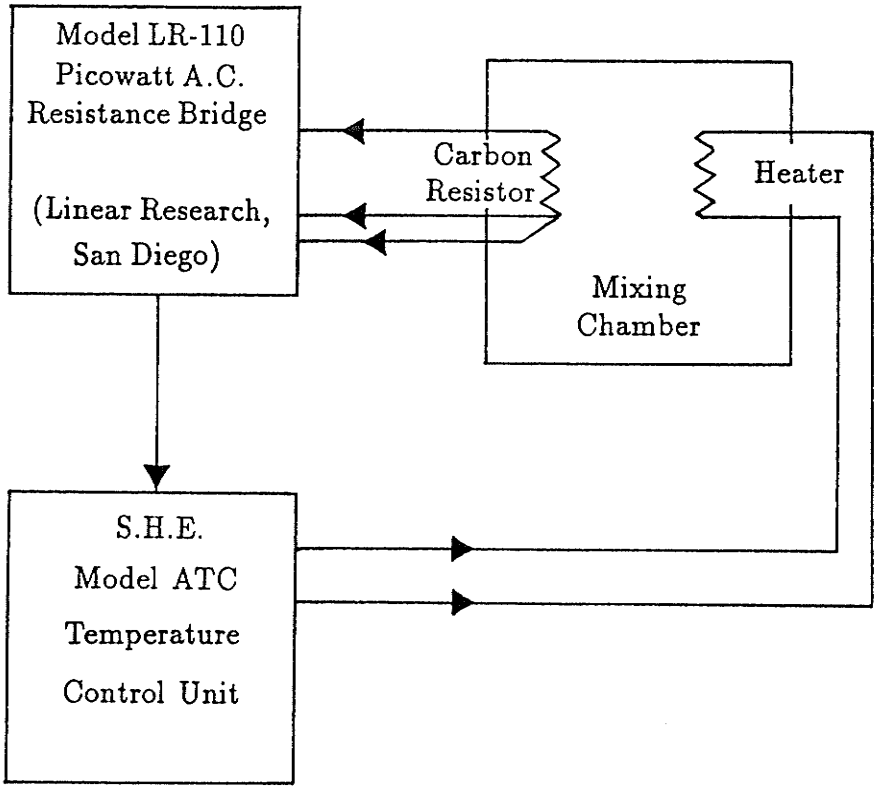

Figure 2.12: Temperature control of the mixing chamber. The carbon resistor and heater are in good thermal contact with the copper mixing chamber. A bridge compares the carbon resistance to a set value corresponding to the desired temperature. The difference is fed into the ATC, which in turn adjusts the heater current to oppose the imbalance (after Yeung, 1988).

The He^4 Cryostat/A.C. Susceptometer

Like the dilution refrigerator, the He^4 cryostat basically consists of a pumping system and a cryogenic core surrounded by a He^4 bath. However, there is no need for a large vacuum can since the cryogenic plumbing of the refrigerator is avoided. Instead, only a small volume containing the magnetic sample need be evacuated. The pumping network is also much simpler, and consists only of provisions to pump on the He^4 bath, the sample chamber, and the walls of the He^4 dewar. By pumping on the bath with an Alcatel model 2033 pump, the system can be cooled to as low as 1.5 K. A schematic diagram of the He^4 cryostat is displayed in Figure 2.13.

The sample chamber is machined out of Emerson and Cuming 1266 Stycast clear epoxy, and glued to one end of a meter long stainless steel pumping tube of low thermal conductivity. The use of epoxy avoids the skin-depth problems associated with metals in A.C. fields. During normal operation the sample chamber and much of the pumping tube are surrounded by the He^4 bath, while the far end of the pumping tube is exposed to room temperature.

The magnetic sample is attached with G.E. varnish and high-purity silver paint (from SPI Supplies, West Chester PA) to the bottom of a 99.99% pure silver sample block of high thermal conductivity. A 25Ω sample heater is made by winding 36-guage Manganin wire around the top of the sample block, while precise temperature measurement is obtained via a calibrated Silicon diode (model DT-470-SD-13 from Lake Shore Cryotronics) placed in good thermal contact with the block.

A sample rod of low thermal conductivity is constructed by bonding the

top of the sample block to a 1.25″ quartz tube, which in turn is glued to an approximately meter long stainless steel tube of small diameter. The heater and diode are connected by copper leads to an electrical socket at the opposite (room temperature) end of the rod. To suspend the sample within the sample chamber, the rod is fed down through the pumping tube. Brass spacers on the rod are used as a guide to prevent the sample from touching the sides of the chamber. The top end of the rod screws onto the top of the pumping tube with a vacuum-tight seal, enabling the sample chamber to be evacuated.

Between 1.5 and 4.2 K, the temperature of the sample is controlled solely by pumping on the He^4 bath through a manostat. A heat leak from room temperature (possibly due to the copper wire leads for the heater, etc.) makes it necessary to fill the sample chamber with He^4 exchange gas (about 10 Torr at 4K) to enhance the thermal coupling between the sample and the bath.

To heat the sample above 4.2 K, it is necessary to evacuate the sample chamber down to $\sim 10^{-5}$ Torr (using a Sargent Welch model 1402 mechanical pump and an oil diffusion pump) because the 25Ω heater is not effective enough to overcome strong thermal coupling to the cold bath. With the manostat disabled, the temperature is controlled by connecting the heater and the Silicon diode to a model 520 Cryogenic Temperature Controller from Lake Shore Cryotronics, Incorporated. The system is hypothetically capable of controlled operation as high as 300 K, though at the time this thesis was prepared, the highest temperature tested was about 250 K.

Figure 2.13 also portrays the coil geometry for the A.C. susceptometer. The pickup coils, A.C. field coil, and the D.C. field coil are all wound on clear

epoxy formers and designed to fit concentrically about the bottom of the sample chamber.

The pickup coils are wound (8 turns each) on a cylindrical spool, and have an inner diameter of 0.274″ and a center-to-center coil separation of 0.625″. Superconducting Niobium-Titanium 0.006″ wire is used. The sample rod is positioned such that the sample is half-way into the upper arm of the astatic pair.

The A.C. field coil (or primary coil) has an inner diameter of 0.41″, and is wound in a single layer with about 215 turns of 0.006″ Niobium-Titanium wire. The primary coil completely surrounds the pickup coils and the sample.

The superconducting leads for both the astatic pair and the primary coil are threaded through Pb tubing and connected to the appropriate terminals on the SQUID probe. The leads are also passed through a small Teflon box containing a carbon resistor. By supplying current to the resistor, the leads may be heated and driven into normal conduction to eliminate unwanted persistent currents in the coils.

The D.C. field coil is wound from 0.008″ copper wire, and is designed to provide a fairly uniform magnetic field for the sample and the astatic pair. It consists of a central solenoid with a single layer of 68 turns, plus two *compensating* solenoids (one at each end) with 3 layers and about 24 turns per layer. All three windings have the same inner diameter of 1.1024″. A field profile along the central axis of the coil is shown in Figure 2.14. The D.C. coil utilizes the same constant current source as the He^3–He^4 dilution refigerator/magnetometer, and is capable of delivering about 45 gauss at the maximum available current of 1 ampere. Copper wire is used to avoid remanent fields which can be produced

by superconducting solenoids. The leads for the D.C. coil are twisted together, threaded through a stainless steel tube, and connected to an electrical socket at room temperature.

RF noise is reduced by surrounding the SQUID probe and the sample chamber by a metal can covered in lead foil. To suppress vibrational noise, the cryostat is supported by a stand with a massive sand foundation, and flexible bellows are used on the pumping lines.

Besides measuring the A.C. susceptibility as a function of field and temperature, the system can be configured as a magnetometer simply by re-connecting the pickup coils to the appropriate terminals on the SQUID probe, and disconnecting the primary coil. As shown in Figure 2.13, the sample rod is attached through a vacuum seal to a hydraulically activated piston. This allows the sample to be withdrawn from the pickup coils at any time, and provides a means of determining whether the sample has been magnetized. Hence, it also provides a direct method to find the current required such that the D.C. field coil cancels the earth's magnetic field exactly.

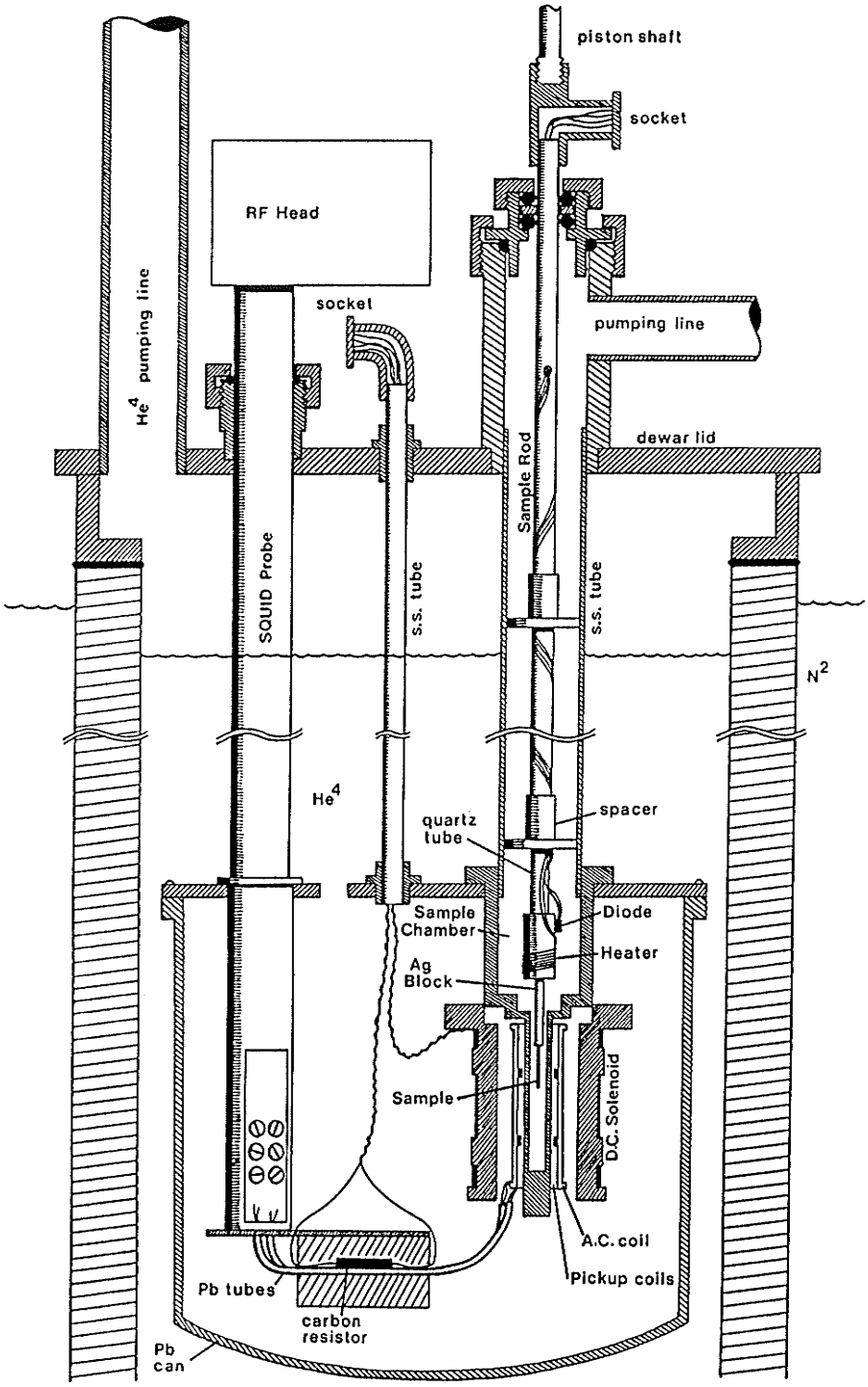

Figure 2.13: A schematic diagram of the He^4 cryostat/A.C. susceptometer. The sample chamber and various field-coil formers are drawn to scale, with the sample length representing 1 cm.

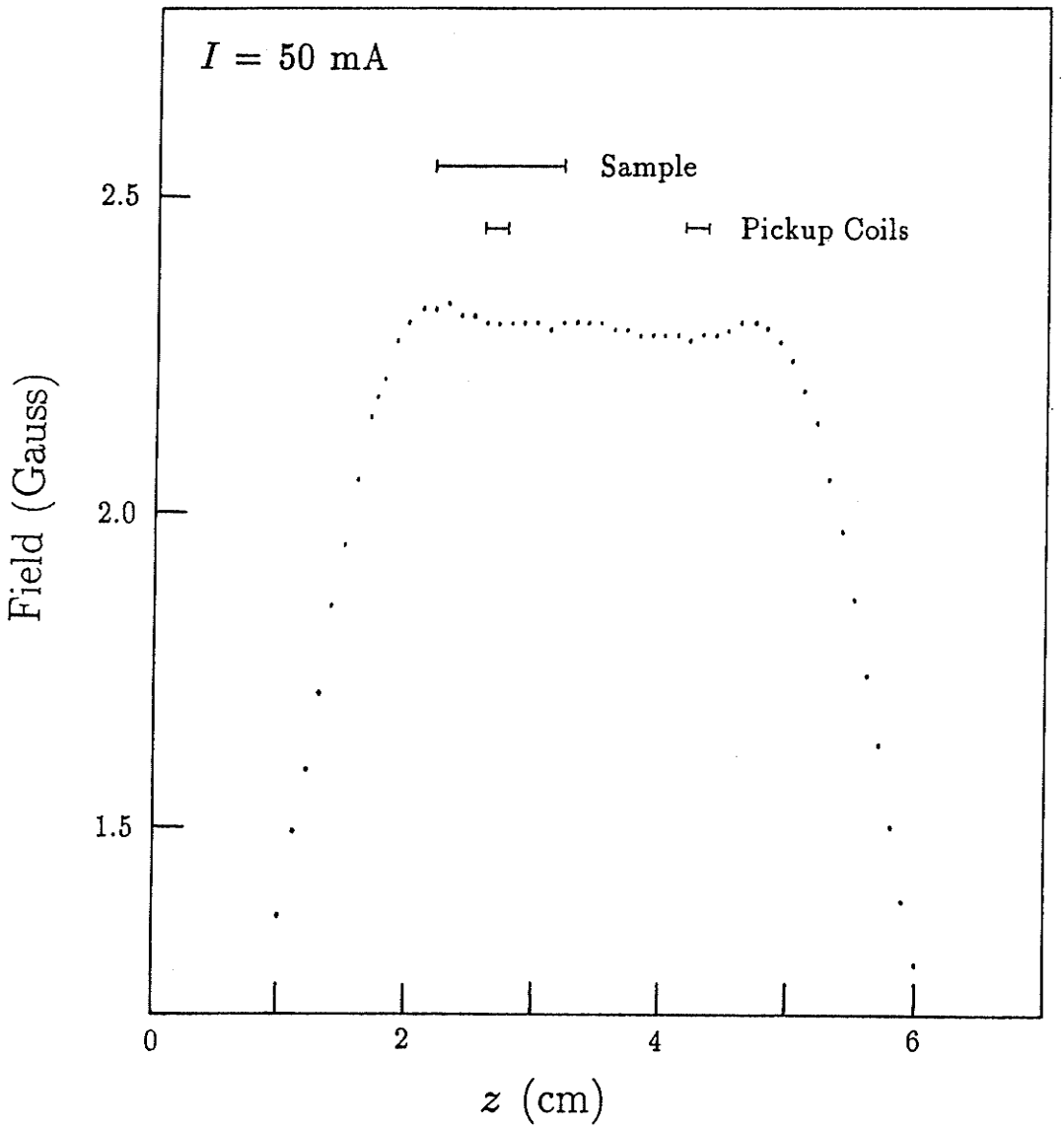

Figure 2.14: Magnetic field profile along the central axis of the D.C. field coil, for a current of 50 mA. The slight asymmetry is due to the measuring technique, and not the coil construction.

2.2 Preparation of Dilute Alloy Samples

A total of one ternary and three binary alloys were prepared with the following consistencies: **Pd** + 0.07 *at.*% Fe, **Pd** + 0.07 *at.*% Mn, **Pd** + 0.1 *at.*% Mn, and (**Pd** + 0.35 *at.*% Fe) + 5 *at.*% Mn. The magnetic impurity concentrations render all of the alloys potentially re-entrant.

The fabrication started with the creation of **Pd**Fe and **Pd**Mn master alloys of fairly high magnetic impurity concentration ($\sim$ 10 *at.*%). The basic components were 99.999% pure Pd sponge (Johnson-Mathey, London), 99.99% pure Mn flake (Aldrich Chemical Company, Inc., Milwaukee, Wisconsin), and 99.99% pure Fe pellets (Johnson-Mathey, London). To begin, the Pd sponge was pressed into disc-shaped pellets and melted on the water-cooled hearth of an arc furnace with an inert Argon atmosphere. The resulting button was then cold-rolled between Mylar sheets until it was thin enough to cut with scissors. A similar procedure was followed to obtain Fe and Mn foils. Next, the appropriate amounts of either Fe foil or Mn foil were wrapped within the Pd foil, and the metals were melted together in the arc furnace. Each alloy button was inverted and re-melted several times over to ensure homogeneity, and negligably small melting losses were noted at every stage of the master alloy preparation.

With the master alloys prepared, it was straight-forward to add the appropriate amounts of pure Pd and dilute them down to the concentrations required for the three binary alloys—in the case of the ternary alloy, it was also necessary to mix the two types of master alloys together in the proper ratio. The new mixtures were repeatedly melted and inverted in the arc furnace, as described previously, and once again negligable melting losses were observed for all of the

samples. To remove carbon scoring etc., each alloy was etched in a mixture of 3 parts hydrochloric acid, 1 part nitric acid, and a few drops of hydrogen peroxide. They were then placed in Vycor quartz tubes evacuated to $\sim 5 \times 10^{-6}$ Torr, annealed at 970 ± 5°C for approximately 24 hours, and rapidly quenched in ice water. (The quenching is inessential, however, considering that impurity atom clustering is unlikely to occur in such dilute alloys.)

The three binary alloys were spark cut (using a copper-tube type blade) into needles of about 0.7 mm diameter and 1 cm length. Each needle was etched and cleaned by rolling it along the bottom of a beaker filled with the aforementioned acid mixture, and the resulting needle diameters were $\sim$ 0.5 mm. The **Pd**Fe needle was annealed (in vacuum) for 17 hours at 970 ± 5°C, and quenched in ice water, while the **Pd**Mn needles were annealed for 12 hours at 650 °C, and slow cooled in vacuum. Needle-like shapes were chosen to minimize the effects of sample demagnetization. The samples were destined to be measured on the SQUID magnetometer, so that A.C. skin depth effects were not a factor in deciding their shapes.

On the other hand, the ternary alloy was intended to be analysed on the SQUID A.C. susceptometer, so that skin depth considerations were of prime importance in deciding the sample shape. To this end, the alloy was cold-rolled into a foil of thickness 0.18 mm and cut into three identical strips of dimension 11.5×1.2 mm^2. The strips were then placed in a Vycor glass tube, and annealed for 6 hours with at a pressure of 0.7×10^{-6} Torr and a temperature of 650 °C. Lastly, the strips were stacked upon one another (being careful to separate the adjacent surfaces with masking tape) and bound together with masking tape.

Chapter 3

Data and Analysis: A Study of the Effective Field Model and Several Potentially Re-entrant Palladium Alloys

3.1 Phase Diagrams of PdFe and PdMn

The magnetic properties of dilute **Pd**Fe and **Pd**Mn alloys are highly dependent on the atomic concentrations of the magnetic Fe and Mn impurities (see section 1.1.2 for an overview). Experiments indicate that **Pd**Fe alloys sustain paramagnetic to ferromagnetic transitions for Fe concentrations as low as $c \approx 0.02$ *at.*%Fe (Figure 1.3); the persistence of ferromagnetic ordering in such dilute systems is a consequence of the spherical clouds of polarized (exchange-enhanced) conduction electrons which surround each Fe impurity atom in the Pd host matrix. Associated with each cloud is a giant-moment of up to $10\mu_B$, and their large spatial extent (diameter$\sim$ 10Å) enables overlapping and direct ferromagnetic exchange coupling to occur between them, even in very dilute alloys. Furthermore, the

Curie temperature T_c displays a linear c dependence above $c \approx 0.1$ *at.*%Fe, and a quadratic dependence below. A.C. susceptibility studies performed by Peters et al. (1984) have shown that alloys with concentrations below 0.01 *at.*%Fe are typical RKKY-induced spin glasses. Based on extrapolations of the existing data, the intermediate regime $0.01 < c[at.\%\text{Fe}] < 0.10$ hypothetically corresponds to a re-entrant domain of the magnetic phase diagram, but the very dilute nature of such alloys requires the use of a sophisticated cryogenic apparatus to reveal their magnetic behavior, and hence little direct experimental evidence for such re-entrant transitions has been forthcoming in the literature.

The **Pd**Mn systems possess similar characteristics (including the development of giant-moment polarization clouds about the Mn atoms), though the magnetic phase diagram (Figure 1.5) is more complex, due to anti-ferromagnetic exchange interactions which can occur between closely spaced Mn impurities. For certain concentrations, these short ranged couplings may compete in some way with the longer ranged ferromagnetic exchange bonds which act between the giant-moment polarization clouds, and frustration of the impurity spin orientations can occur. Consequently, there exists in the phase diagram a ferromagnetic regime $0.1 < c < 2.5$ (in which the variation of T_c with c is linear at low concentrations), followed by a re-entrant regime ($2.5 < c < 5$) and a spin glass regime ($c > 5$) at higher concentrations. The static magnetization measurements of Thomson and Thompson (1979) reveal that a more usual RKKY-induced spin glass domain exists for concentrations $c < 0.06$ *at.*%Mn. Extrapolations of the existing data predict the existence of an RKKY-induced re-entrant region for intermediate concentrations of $0.06 < c < 0.1$. However, as in the **Pd**Fe studies, the literature has

not yet provided direct experimental support for such an assertion.

The SQUID magnetometer/dilution refrigerator is ideally suited to the study of these weakly magnetic systems, since it provides the appropriate temperature window (50mK to 1K) and sensitivity. Presented below are the first ever detailed measurements of the temperature and field dependent static magnetizations of several potentially re-entrant (and very dilute) **Pd**Fe and **Pd**Mn alloys. Because significant impurity atom clustering is unlikely to occur in these very dilute samples, the experimental zero-field-cooled magnetization curves should provide a good foundation for comparisons to a simple mean-field model which displays genuine re-entrant transitions, from paramagnetic to ferromagnetic to spin glass (as opposed to cluster glass) ordering.

3.2 PdFe Magnetization Measurements

The dilution refigerator/magnetometer was used to measure the magnetization of the **Pd** + 700 ppm Fe needle as a function of temperature, applied magnetic field, and time. The Fe concentration was deliberately chosen to fall within the potentially re-entrant region of the **Pd**Fe phase diagram, and the needle-like shape of the sample rendered demagnetizing corrections to the internal field unnecessary.

3.2.1 Temperature Dependence of FC and ZFC Magnetization

The field-cooled (FC) magnetization curve was obtained by cooling the sample down to 0.0548 K in a net applied field of $1.25 \pm .25$ Gauss (parallel to the long axis of the needle). Next, the temperature was incremented in steps and the

magnetization recorded until the highest temperature of 0.898 K was reached. The uncertainty in the field is due to the difficulty in determining the helmholtz pair current required to cancel the earth's magnetic field in the neighborhood of the sample.

To acquire the zero-field-cooled (ZFC) curve, the sample was cooled down to 0.0568 K in zero field (± 0.25 Gauss); a field of $1.25 \pm .25$ Gauss was then applied and the magnetization recorded as the temperature was incremented up to 0.737 K in steps.

As shown in Figure 3.0, the FC and ZFC curves are essentially identical above a point of inflection which occurs at temperature $T_{infl} = 0.470 \pm 0.10$ K, but their behavior differs considerably at lower temperatures. In particular, the FC magnetization increases monotonically as the temperature is lowered, and displayed no discernible time effects over the duration of the measurements. On the other hand, the ZFC curve peaks at 0.264 K, and tends towards a zero magnetization ground state at absolute zero. The ZFC magnetization also displayed a noticible upward drift with time for all temperatures below about 0.315 K; to be consistent, 8 to 10 minutes were allowed to elapse before the magnetization was recorded at these temperatures.

Since the magnetometer does not measure in emu/gram, but in volts relative to an arbitrary zero, it was necessary to calibrate the system in some way. This was accomplished by associating T_{infl} with the Curie temperature T_c, and fitting the high temperature ZFC and FC data to a Curie-Weiss law such that

$$M = \frac{CH}{T - T_c} \ .$$

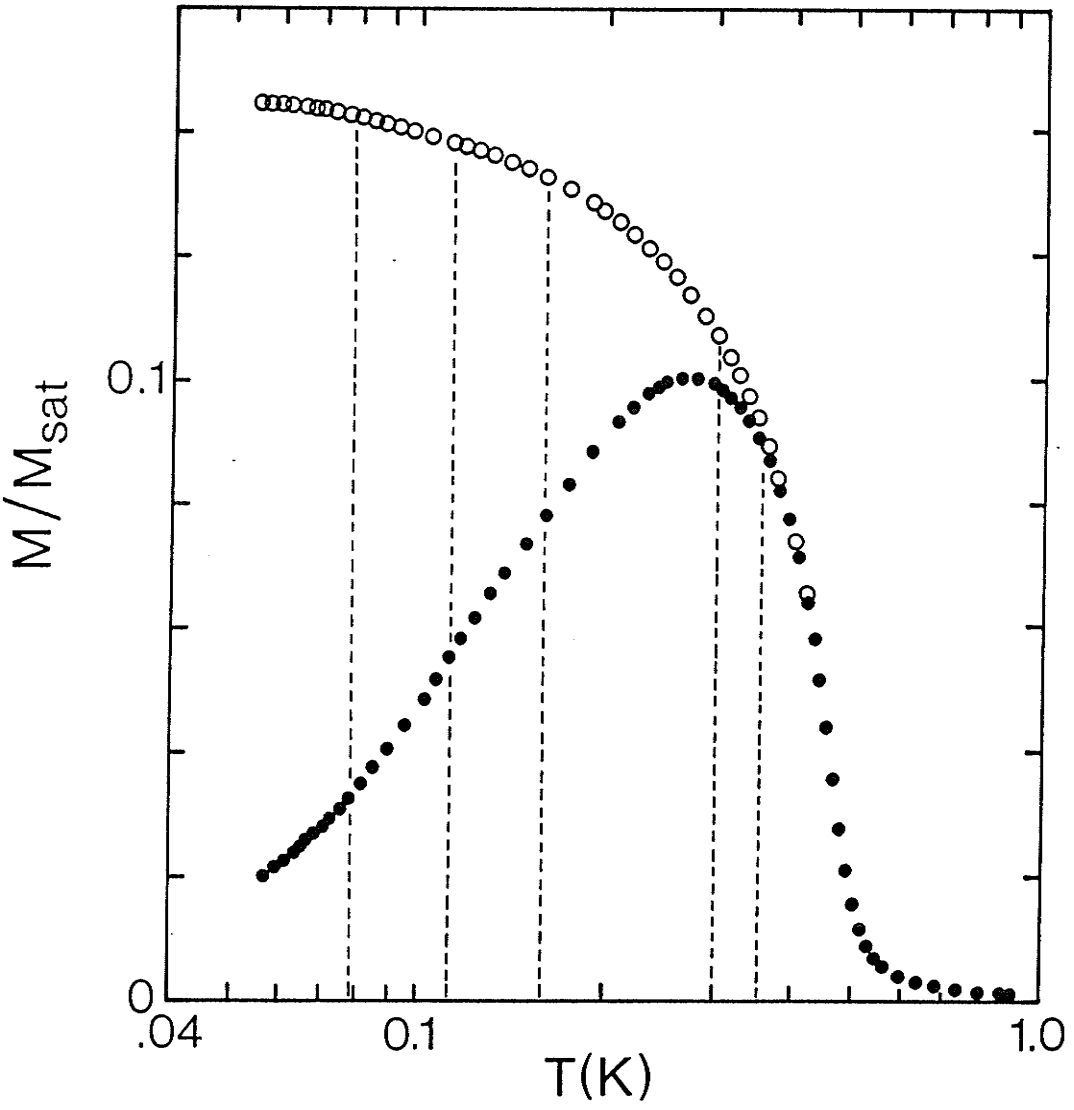

Figure 3.0: The FC (o) and ZFC (•) magnetization curves of the Pd + 700 ppm Fe needle. The vertical lines indicate the temperatures at which time-effects were investigated.

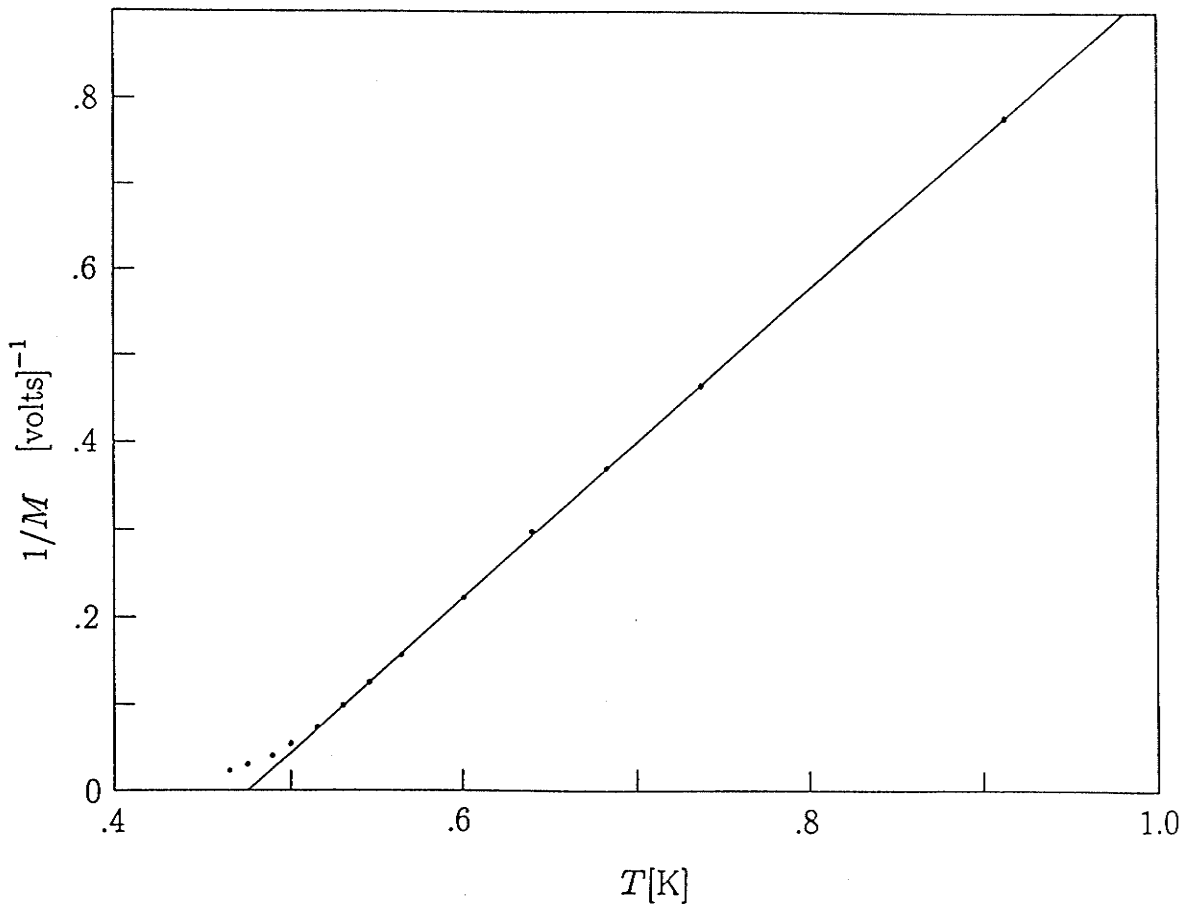

Figure 3.1: The calibration plot of the ZFC data. The straight line represents a fit to a Curie-Weiss law with slope $\frac{1}{CH} = 1.8$ [volts $\cdot$ K]$^{-1}$. A similar plot of the FC data yields a slope $\frac{1}{CH} = 2.2$ [volts $\cdot$ K]$^{-1}$.

The applied field is denoted by H, while C is the Curie constant. By plotting M[volts] versus $\frac{1}{T[\mathrm{K}]}$ for both the ZFC and FC data, it was possible to extrapolate to the infinite temperature limit and obtain the true zeroes (in volts) for the two sets of data.

As shown in Figure 3.1, high temperature plots of $\frac{1}{M[\mathrm{volts}]}$ versus T[K] yield straight lines with slopes of $\frac{1}{CH} = 2.0 \pm .2$ [volts$^{-1} \cdot$K^{-1}]. However, the mean-field theory of ferromagnetism predicts that

$$\begin{aligned} CH &= \frac{cN_A g^2 S(S+1)\mu_B^2 H}{\mathsf{M}3k_B} \\ &= (1.4 \pm .3) \times 10^{-4} \ \frac{\mathrm{emu} \cdot \mathrm{K}}{\mathrm{gram}} \ , \end{aligned}$$

where $c = 7 \times 10^{-4}$ is the atomic ratio of Fe to Pd in the sample, N_A is Avogadro's number, M is the molar mass of Pd, and the effective spin $S = 5$ is chosen in accordance to the results of Chouteau and Tournier (1971). Hence, a calibration of about 1 volt $= 3.4 \times 10^{-4}$[emu/gram] was derived, which can also be written in terms of the saturation magnetization $M_{sat} = \frac{cN_A}{\mathsf{M}} g\mu_B S$ such that 1 volt $= 8.5 \times 10^{-4}\ M_{sat}$.

It is clear that the high temperature behavior of both the ZFC and FC magnetizations is ferromagnetic in character. However, the low temperature behavior of the ZFC curve also suggests a further re-entrant transition into a phase with a spin glass ground state. Such transitions are in fact predicted to occur in the re-entrant domain ($0.8 \leq \overline{J}/\overline{J_0} \leq 1.0$) of the mean-field Effective Field Model (section 1.2.4). With this in mind, the Sherrington-Kirkpatrick-like coupled equations were solved numerically (the technique is described in section 3.5), and the

theoretical temperature dependence of the magnetization was compared to the ZFC experimental curve.

Such a calculation requires the specification of several parameters. Firstly, the spin quantum number is predetermined as S=5. The reduced field $h = \frac{g\mu_B H}{k_B T_c}$ is also predetermined to within the range 0.0003 to 0.0005. Lastly, the exchange-bond parameter $\eta = \overline{J}/\overline{J_0}$ must fall within the re-entrant region defined previously.

Figure 3.2 displays a best fit to the experimental data, with $h = 0.0005$ and $\eta = 0.98$. The temperature T_{SG} indicates the approximate location of the theoretical ferromagnetic/spin-glass phase boundary, and coincides with the location of the peak in the ZFC curve. Also shown is the de Almeida-Thouless temperature T_{AT}, which indicates the theoretical onset of broken replica-symmetry.

The discrepancy at temperatures below the peak is at least partly attributable to the dynamic component of the ZFC magnetization; the model is static and hence incapable of duplicating the time-dependent behavior of the experimental system. Even so, the resemblance between the experimental data and the numerical calculations is striking, and provides some evidence that the experimental system is re-entrant.

3.2.2 Field Dependence of Magnetic Isotherms

Magnetic isotherms were measured for eight temperatures T between 0.4645 K and 0.611 K. Each isotherm was obtained by first cooling in zero field from about 1 K to the desired measuring temperature. With the temperature stabilized, the magnetization was recorded as the field H was increased from approximately 0

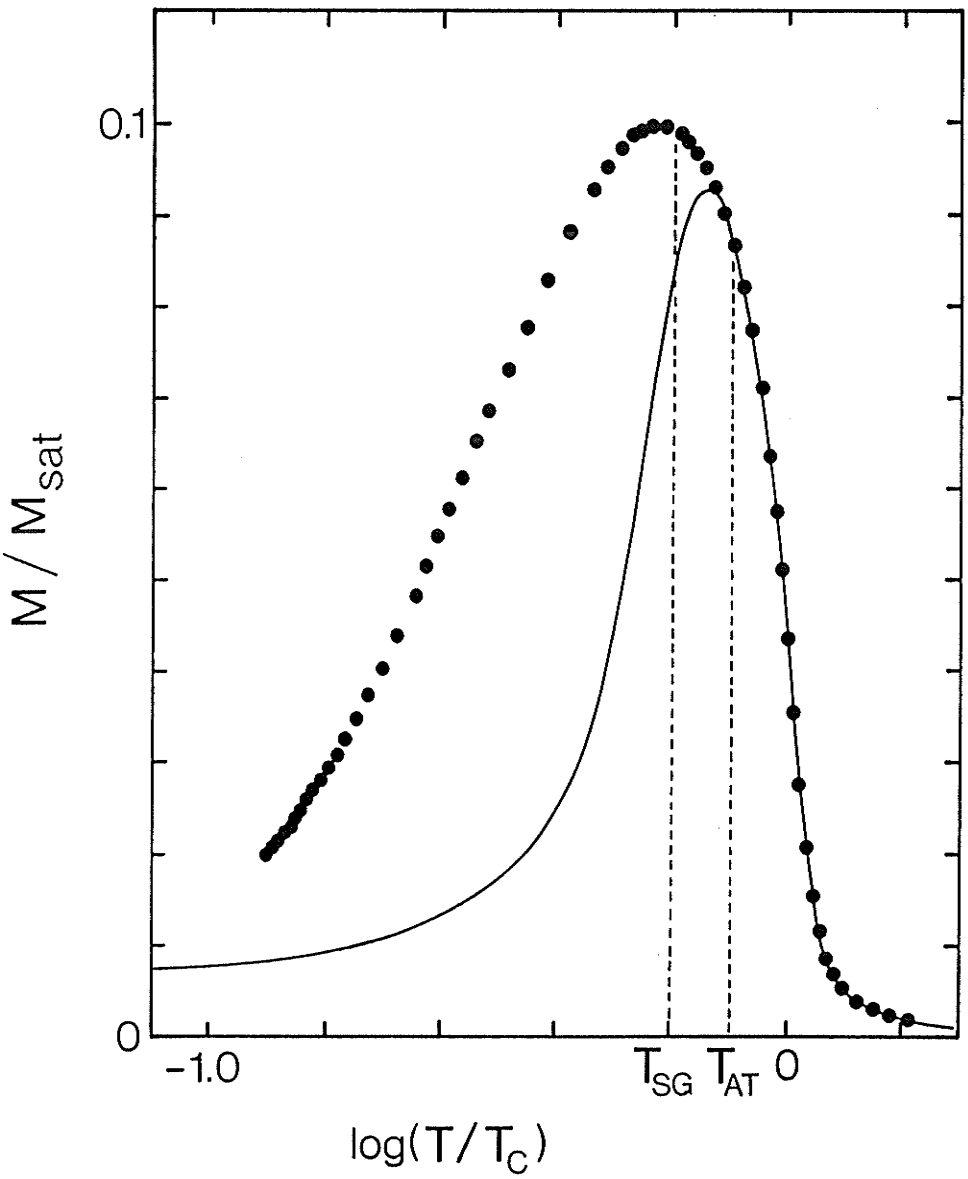

Figure 3.2: A comparison between the ZFC curve (•) of the **Pd** + 700 ppm Fe sample and a theoretical re-entrant calculation (solid curve) with $h = 0.0005$, $S = 5$, and $\eta = 0.98$. The theoretical re-entrant spin glass temperature T_{SG} is indicated, as is the de Almeida-Thouless instability temperature T_{AT}.

to 10 Gauss. Figure 3.3(a) shows the experimental isotherms plotted in terms of M/M_{sat} versus the reduced field h, such that $0 \leq h \leq 0.0030$.

For comparison, the Effective Field Model was used to generate isotherms over the same interval of reduced field and with a value of $\eta = 0.98$ chosen to be within the re-entrant region. The theoretical isotherms are plotted in Figure 3.3(b). The calculations span the range of reduced temperature $t = T/T_c$ from 1.001 to 1.5, while the experimental isotherms have reduced temperatures from about 1.001 to 1.3 (assuming $T_c = 0.464$ K). Once again the behavior of the experimental data is remarkably similar to that of the theoretical re-entrant system.

The initial slopes of the experimental isotherms represent the zero field susceptibilities, and were found to diverge as $[(T - T_c)/T_c]^{-\gamma}$ with $\gamma = 1.7 \pm 0.1$ and $T_c \simeq 0.464$ K. The exponent is greater than the typical value of $\gamma = 4/3$, as determined from the three-dimensional Heisenberg model of ferromagnetism. However, even larger exponents have been observed by Ho et al. (1981) in their investigations of **Pd**Mn alloys with concentrations between those typical of the ferromagnetic and spin glass systems.

3.2.3 Time Dependence of the Thermo-remanent Magnetization

As mentioned in the first chapter, the magnetic relaxation of ferromagnets is generally associated with a logarithmic time dependence, while the relaxation in spin glass systems is better described by a stretched-exponential function. Hence, an anomaly in the relaxation of a re-entrant system might be expected to occur as the system is passed through the spin glass/ferromagnetic phase boundary.

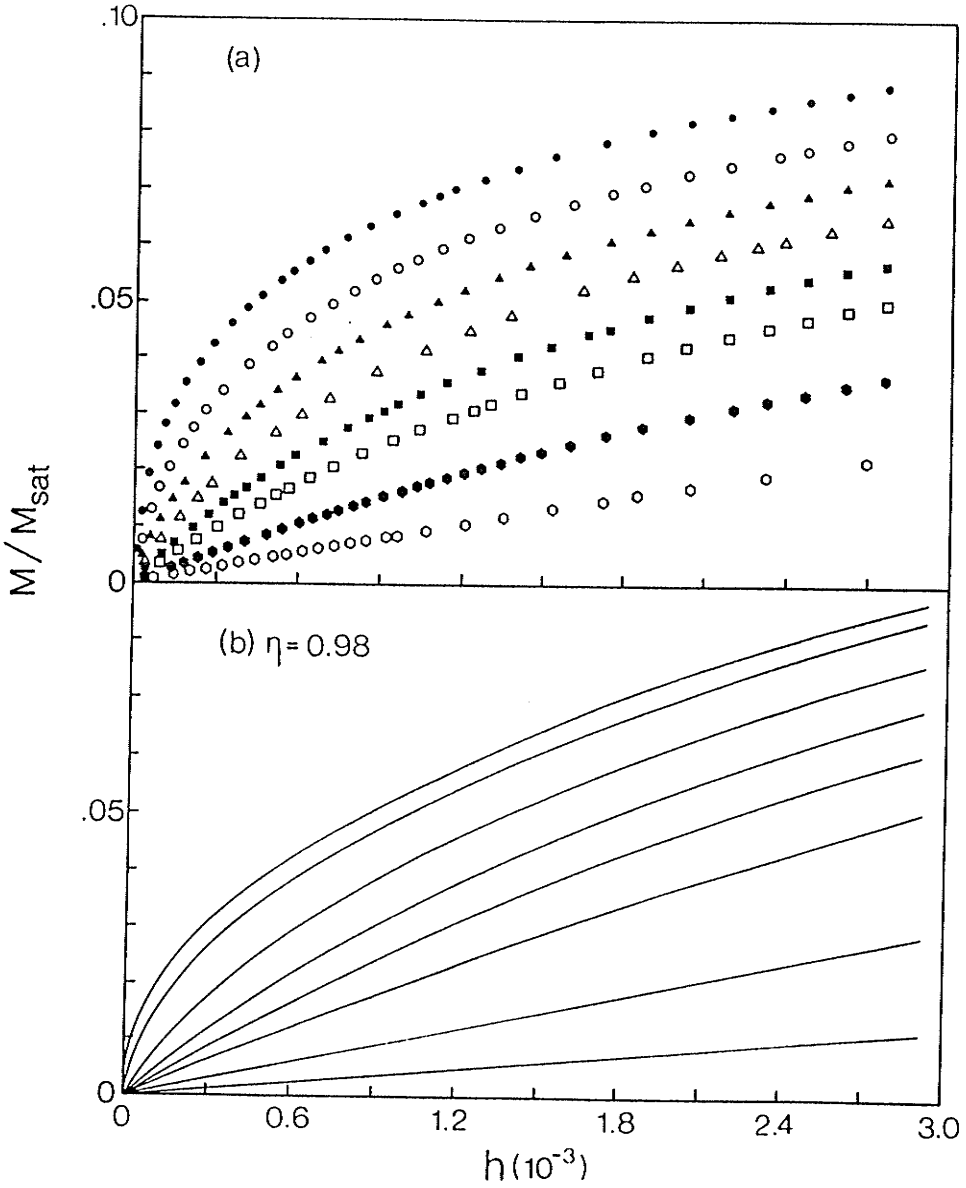

Figure 3.3: (a) Experimental magnetic isotherms of **Pd** + 700 ppm Fe. The temperatures from top to bottom are T =0.4645, 0.475, 0.488, 0.500, 0.516, 0.530, 0.561, and 0.611 K.

(b) Theoretical isotherms calculated using $S = 5$ and a re-entrant value of $\eta = 0.98$. From top to bottom the reduced temperatures are t =1.001, 1.01, 1.03, 1.05, 1.07, 1.1, 1.2, and 1.5.

To search for such an anomaly in the PdFe system, the decay of the thermo-remanent magnetization σ_{trm} was measured for five temperatures T between 0.0788 K and 0.354 K. These temperatures are indicated in Figure 3.0, and represent the entire range over which time-effects were observed in the ZFC magnetization measurements. To measure the decay, a field of ~ 2 Gauss was applied while the sample was cooled down to T from a reference temperature of 0.475 K (at which no time effects were observed). After stabilizing at T for about 30 minutes, the applied field was set to zero and the σ_{trm} relaxation was monitored for 7200 seconds on a chart recorder. The same reference temperature was used for all the runs, as this allowed scaling of the magnetization data relative to a common zero.

Figure 3.4 displays semi-log plots of σ_{trm} versus time for all the temperatures T—linear behavior indicates a logarithmic decay. The time zeroes are chosen so that the curves are as linear as possible within the range of uncertainty; all times could be increased by up to 8 seconds, though this enhances the curvature, especially at low times. The discrepancies for times $t > 10^3$ seconds are accounted for by slight field drifts and temperature instabilities. Clearly, the data are almost logarithmic, except for the appearance of small deviations at times $t < 100$ seconds. The relaxation rate $\partial\sigma_{trm}/\partial \log t$ is, however, essentially independent of temperature, with no indication of an anomaly.

As demonstrated in Figure 3.5, the lowest temperature data (which are representative of all the measurements) are well described over the full range of

times by a stretched-exponential function

$$\sigma_{trm} = \sigma_0 \exp\left[-\left(\frac{t}{\tau}\right)^{1-n}\right] \quad .$$

However, the extracted value of the exponent n is unusually close to unity. A likely explanation is that the weakness of the decay renders the fit somewhat insensitive to the parameters n and τ. The suggestion of a stretched-exponential decay (for all temperatures studied) implies that the distinction between the spin glass and ferromagnetic phases is becoming vague in this system.

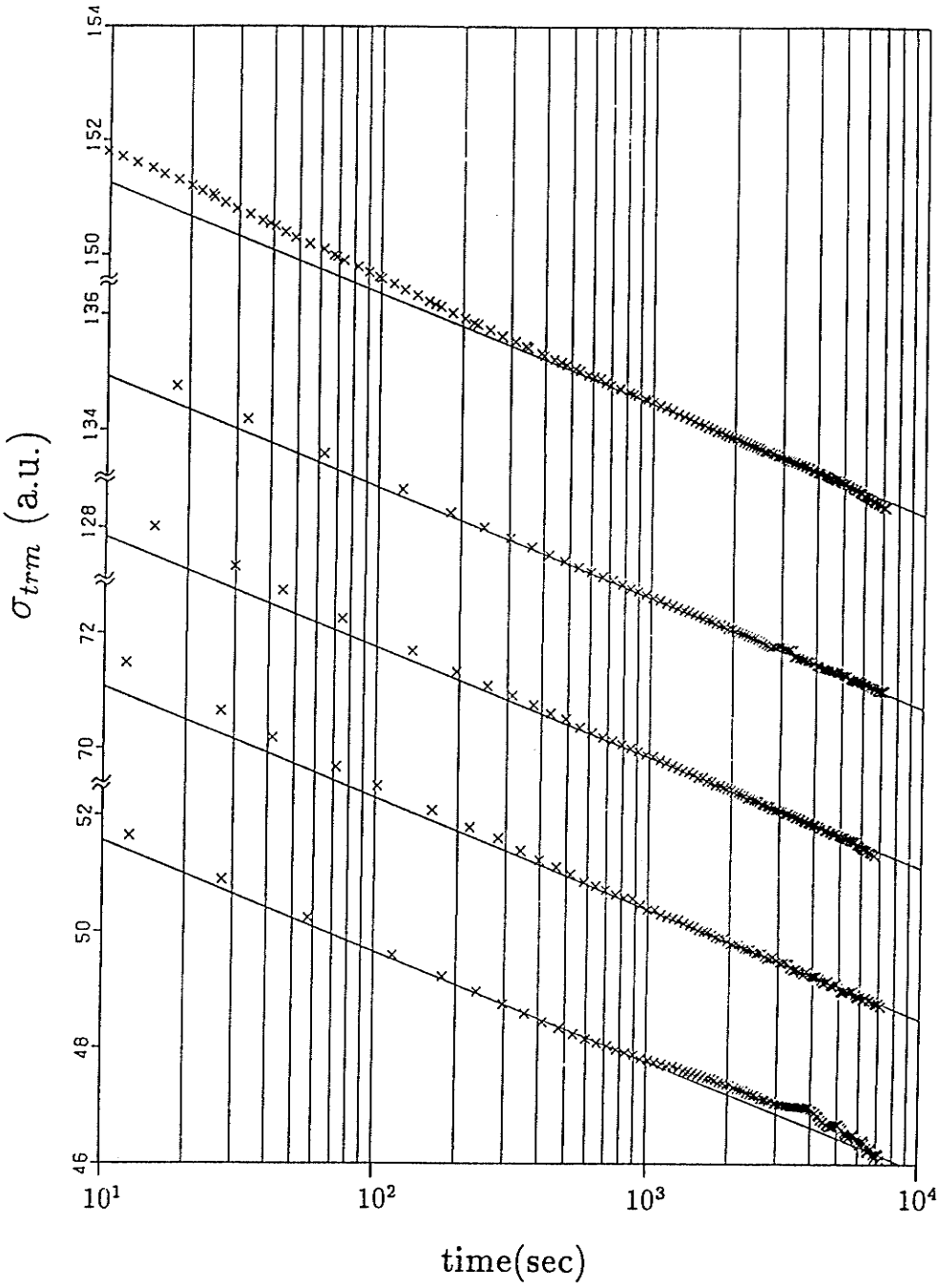

Figure 3.4: Logarithmic tests of the σ_{trm} decay for the **Pd** + 700 ppm Fe system. From top to bottom the temperatures correspond to $T = 0.0788 \pm .0004$, $0.113 \pm .001$, $0.161 \pm .001$, $0.300 \pm .002$, and $0.354 \pm .002$ K. The straight lines have a common slope, and are provided to guide the eye.

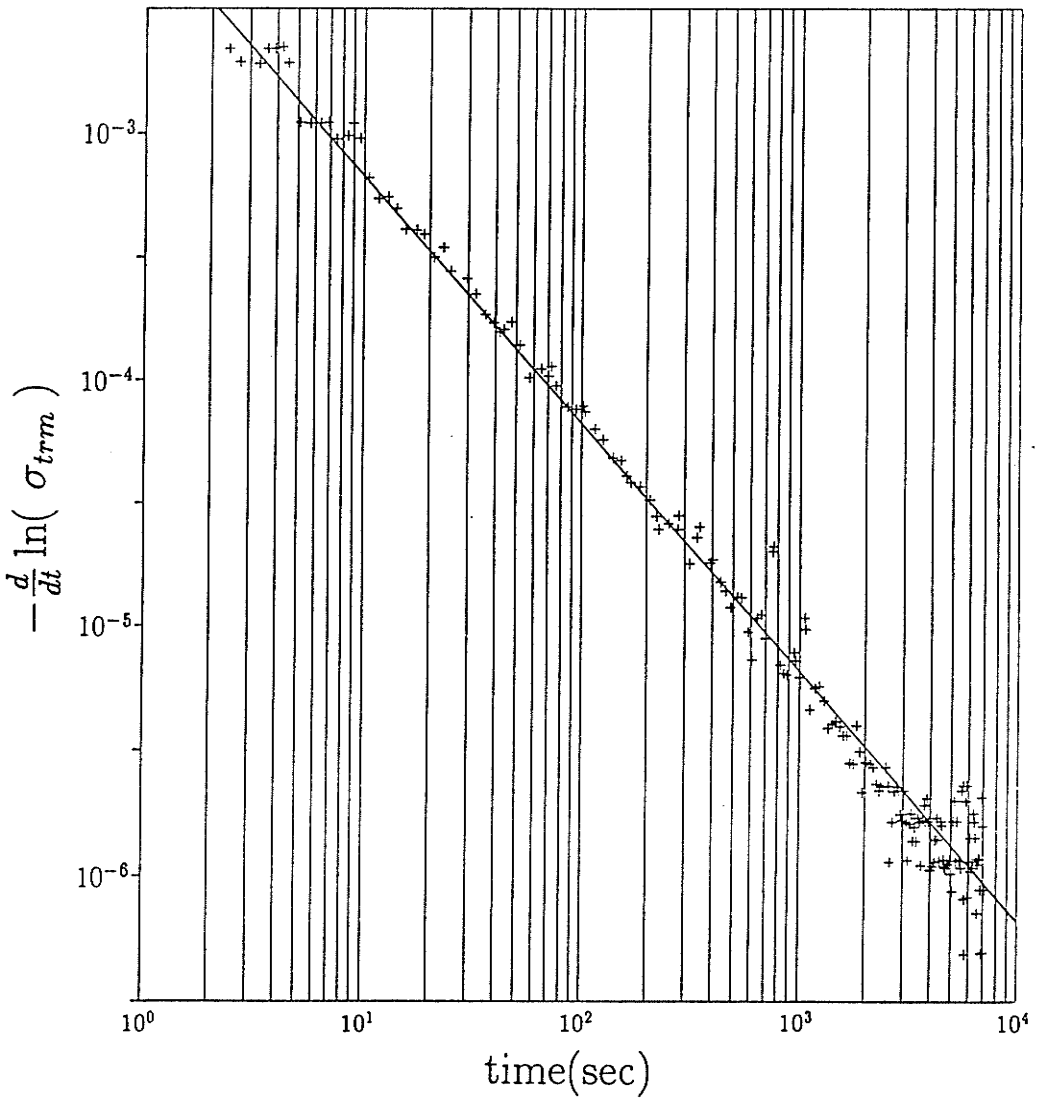

Figure 3.5: A typical stretched-exponential test of the σ_{trm} decay ($T = 0.0788 \pm .0004$ K). The slope represents the exponent $-n$ and, as indicated by the straight line, is unusually close to unity.

3.3 PdMn Magnetization Measurements

Like the **Pd** + 700 ppm Fe system, alloys of **Pd** + 700 ppm Mn and **Pd** + 1000 ppm Mn have concentrations within a potentially re-entrant region of their phase diagram. Samples of these two **Pd**Mn alloys were prepared as needles and investigated using the dilution refigerator/ magnetometer. Once again the shape of the samples made demagnetizing corrections unnecessary.

3.3.1 Temperature Dependence of ZFC Magnetization

The ZFC curves for the **Pd**Mn samples were acquired and analysed in a fashion identical to the **Pd**Fe system. Each sample was first cooled down to $\sim$ 0.05 K under approximately zero field conditions. A field of $H = 1.25 \pm .25$ Gauss was then applied and the magnetization recorded as the temperature was increased up to $\sim$ 0.5 K in steps. As shown in Figure 3.6, both of the curves display a peak similar to that of the **Pd**Fe system, though the low temperature structures are not revealed.

The 700 ppm Mn curve has an inflection point at $T_{infl} = 0.085 \pm .005$ K (tentatively associated with T_c), above which the data follows a Curie-Weiss behavior. A plot of M versus $\frac{1}{T}$ was constructed to zero the data, while a plot of $\frac{1}{M}$ versus T gave a slope of $\frac{1}{CH} = 9 \pm 1$ [volts$^{-1} \cdot$ K^{-1}] and a calibration of approximately 1 volt=1.1×10^{-3} [emu/gram] (assuming a spin of $S = 5$ and an impurity concentration of $c = 7 \times 10^{-4}$).

Similarly, the 1000 ppm Mn curve displays Curie-Weiss behavior above the inflection point $T_{infl} = T_c = 0.135 \pm .005$ K, and the data were zeroed in the usual way. The calibration plot yielded a slope of $\frac{1}{CH} = 3.6 \pm .1$ [volts$^{-1} \cdot$ K^{-1}],

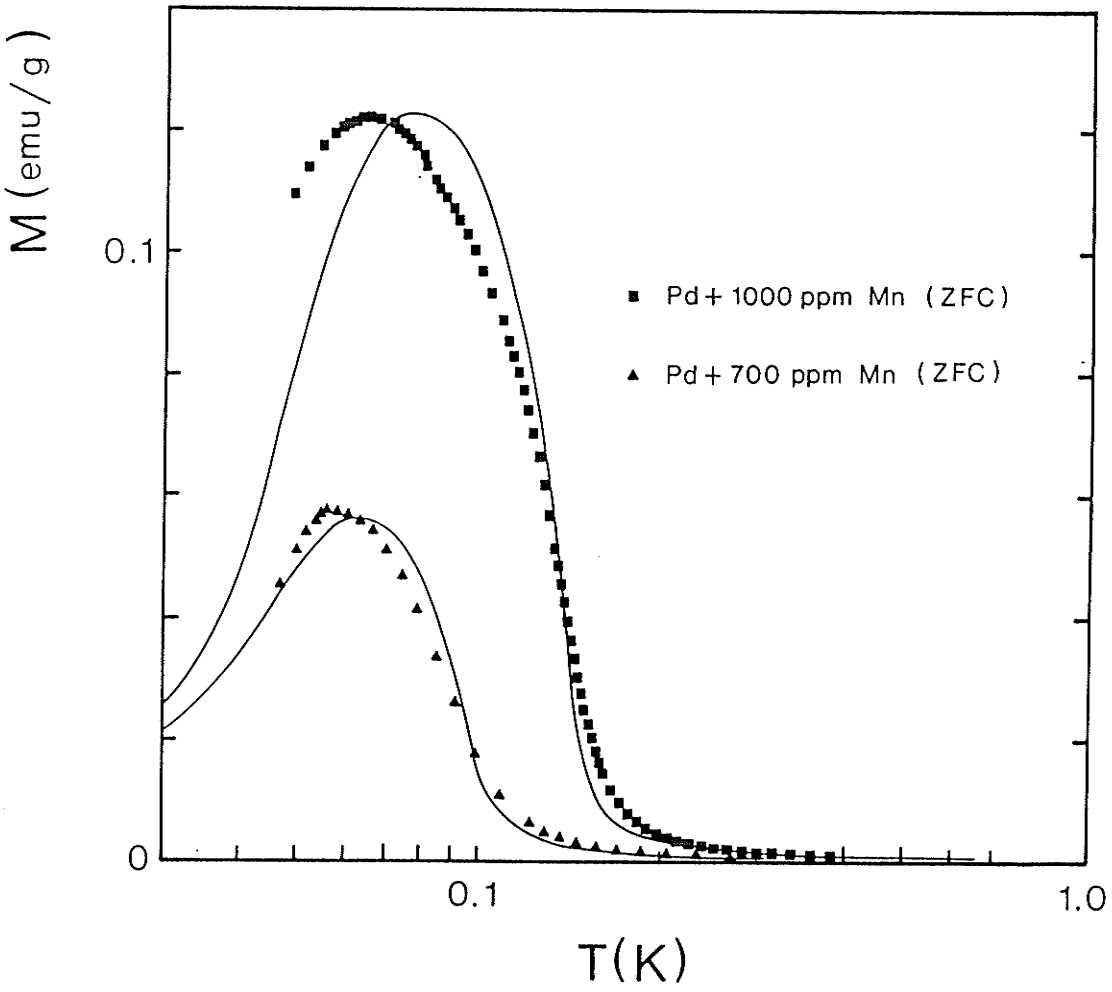

Figure 3.6: The ZFC magnetization curves of the **Pd** + 700 ppm Mn and **Pd** + 1000 ppm Mn needles are compared to theoretical re-entrant calculations (solid curves).

which corresponds to 1 volt=6×10^{-4} [emu/gram] (using $c = 10^{-3}$ and $S = 5$). Incidently, the independent calibrations for the two alloys are self consistent; the value of $\frac{1}{CH}$ (in units of [gram/emu·K]) for the 700 ppm Mn case is a factor of $\frac{1000}{700}$ larger than the value for the 1000 ppm Mn data.

The Effective Field Model with spin S=5 was used to generate theoretical curves within the re-entrant region $0.8 \leq \eta \leq 1.0$. The best fit to the 700 ppm Mn data is displayed in Figure 3.6, and corresponds to an exchange bond parameter of $\eta = 0.97$ and a reduced field of $h = \frac{g\mu_B H}{k_B T_c} = 0.0017$ (equivalent to $H \simeq 1$ Gauss). Also included is the best fit to the 1000 ppm Mn curve; this calculation used $\eta = 0.93$ and a reduced field of h=0.0010 ($H \simeq 1$ Gauss). Note that the two values of η have internal consistency, as the alloy of higher concentration is, as expected, farther from the tricritical point $\eta = 1.0$. Moreover, the basic features of the two ZFC curves are duplicated by the re-entrant model calculations.

3.3.2 Field Dependence of Magnetic Isotherms

Several magnetic isotherms were measured for the **Pd** + 700 ppm Mn sample by zero field cooling the specimen down to the appropriate measuring temperature; with the temperature stabilized, the magnetization was then recorded as the applied field was increased from approximately 0 to 10 Gauss. This is equivalent to a reduced field range of about $0 \leq h \leq 0.0030$. The calibration of 1 volt=1.1×10^{-3} [emu/gram] was used to scale the data which are plotted in Figure 3.7(a). The isotherms were measured for temperatures T between 0.061 K and 0.182 K, or a reduced temperature interval of $0.72 \leq T/T_c \leq 2.14$ (assuming $T_c = 0.085$ K).

Figure 3.7(b) portrays the curves generated from the Effective Field Model

with $S = 5$, $\eta = 0.97$, and reduced temperature and field ranges of $0.6 \leq T/T_c \leq 1.4$ and $0 \leq h \leq 0.0030$, respectively. The re-entrant calculations are able once again to mimic the behavior of the experimental curves.

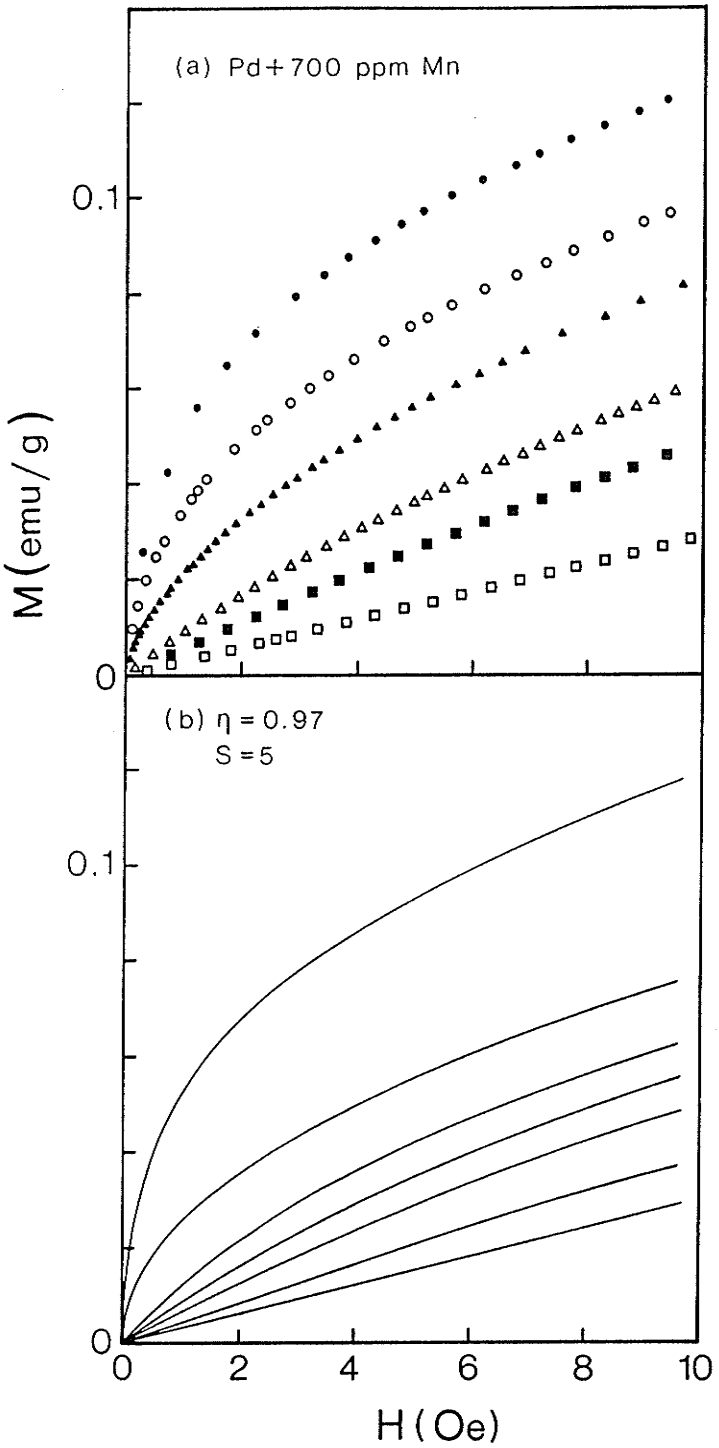

Figure 3.7: (a) Experimental magnetic isotherms of **Pd** + 700 ppm Mn for temperatures (from top to bottom) of $T = 0.061$, 0.070, 0.098, 0.118, 0.133, and 0.182 K.

(b) Theoretical isotherms calculated with a re-entrant value of $\eta = 0.97$. From top to bottom the reduced temperatures are $t = 0.6$, 1.01, 1.1, 1.15, 1.2, 1.3, and 1.4.

3.4 A Possible Mean-Field Criterion for Identifying a Re-entrant Phase Transition

As introduced in section 1.1.3, Kunkel and Williams (1988) have presented intriguing evidence for the existence of a re-entrant transition in a (**Pd**Fe)Mn system. In particular, they discovered a weak anomaly in the non-linear component of the susceptibility which, though not singular, is suggestive of re-entrant critical behavior. Based on the success of the mean-field Effective Field Model (section 1.2.4) in describing the magnetization of the potentially re-entrant **Pd**Fe and **Pd**Mn systems, it was decided to determine whether the re-entrant model calculations are also able to duplicate the systematics of the (**Pd**Fe)Mn susceptibility measurements. Additionally, the calculations are compared to more recent SQUID A.C. susceptometer measurements on the same alloy. An explanation of the numerical techniques involved with solving the model is provided in Section 3.5.

3.4.1 Temperature Dependence of the Magnetization and Susceptibility

All of the simulations in the sections following were performed using spin $S = 5/2$, and a value of $\eta = \overline{J}/\overline{J_0} = 0.9$ within the re-entrant regime $0.8 \leq \eta \leq 1.0$. Figure 3.8 shows a plot of the calculated local magnetization m versus the reduced temperature $t = T/T_c$ for various values of the reduced field $h = \frac{g\mu_B H}{k_B T_c}$ within the interval $0 \leq h \leq 0.01$. By carefully noting where the spontaneus magnetization curve vanishes for $t < 1.0$, a ratio of $T_{SG}/T_c = 0.269285$ was established for the ferromagnetic/spin glass re-entrant temperature T_{SG}.

Figure 3.9 shows the differential susceptibility $\chi = \partial m/\partial h$ plotted versus t over the same range of reduced temperatures and fields as the magnetization. For $h \neq 0$, the curves are qualitatively the same as those shown in Figure 1.8(b) for the experimental (**Pd**Fe)Mn system in a finite static biasing field. The experimental and theoretical curves both display twin peaks which are driven apart and reduced in amplitude by increasing the field. Furthermore, the heights of the lower-temperature peaks are (in both systems) generally greater than those of the corresponding higher-temperature peaks. Though the theoretical zero-field curve diverges at T_{SG} and T_c, the experimental zero-field susceptibility is quite different. Instead, the experimental data possess an essentially temperature independent plateau, located roughly between T_{SG} and T_c, which is thought to be caused primarily by domain wall dynamics which cannot be reproduced by the simple model. These effects tend to restrict the experimental critical analyses to temperatures $T > T_c$ and $T < T_{SG}$. (Experiments performed by Zastre et al. (1985) indicate that the magnetic time effects observed in spin glass systems do *not* conceal the associated critical behavior, and it is probable that the same is true for re-entrant systems below T_{SG}.)

3.4.2 Field Dependence of Susceptibility Isotherms

The model was used to generate susceptibility isotherms in the vicinity of both the upper and lower transitions. With the data separated into four regions ($T > T_{SG}$, $T < T_{SG}$, $T > T_c$, and $T < T_c$), the susceptibility χ, which can generally be expanded in powers of h as

$$\chi(h,t) = \chi(0,t) - a_2(t)h^2 + a_4(t)h^4 - \ldots \tag{3.1}$$

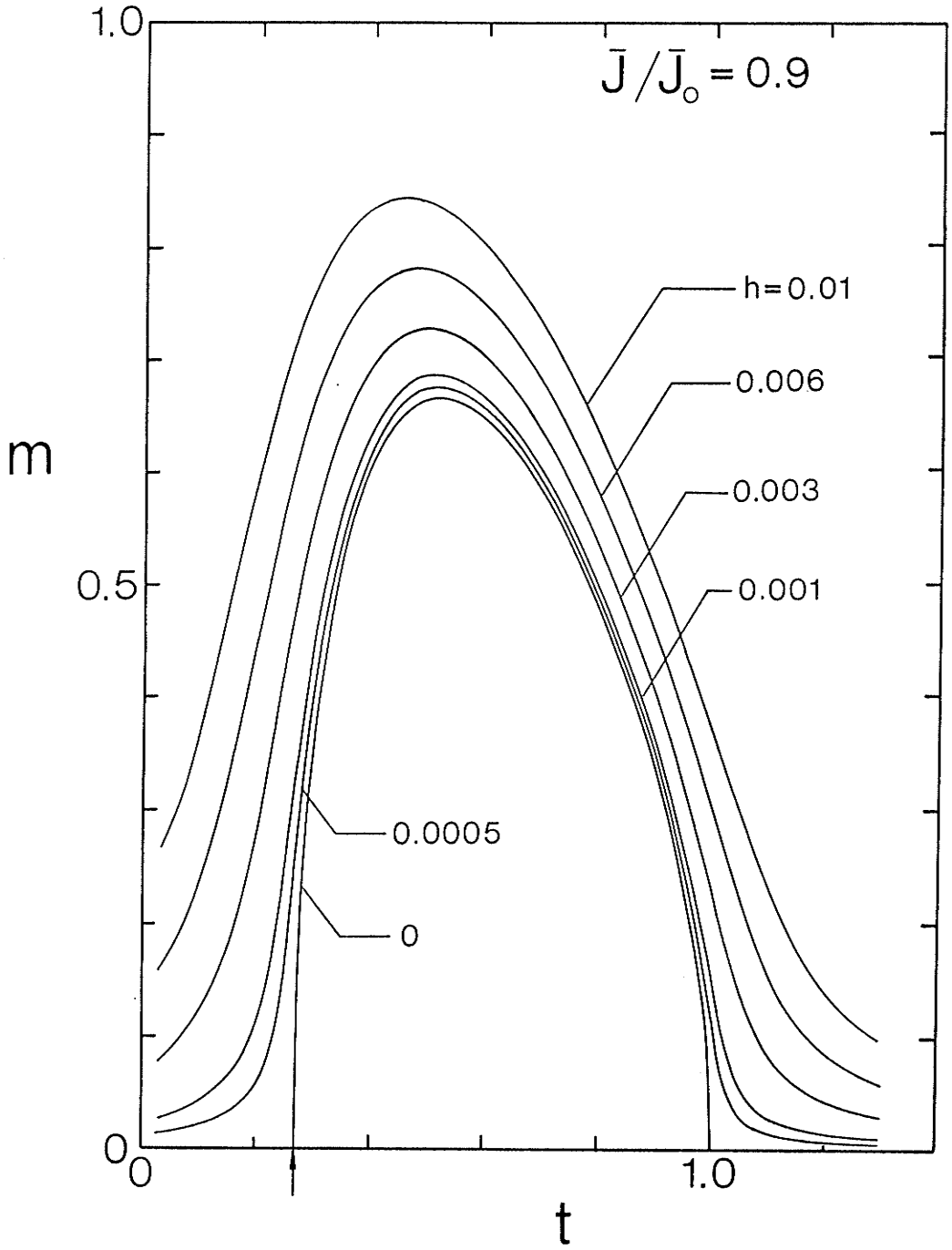

Figure 3.8: A theoretical plot of the local magnetization m versus the reduced temperature t for various reduced fields h. The calculations used $S = 5/2$ and a re-entrant value of $\eta = 0.9$. The arrow indicates T_{SG}.

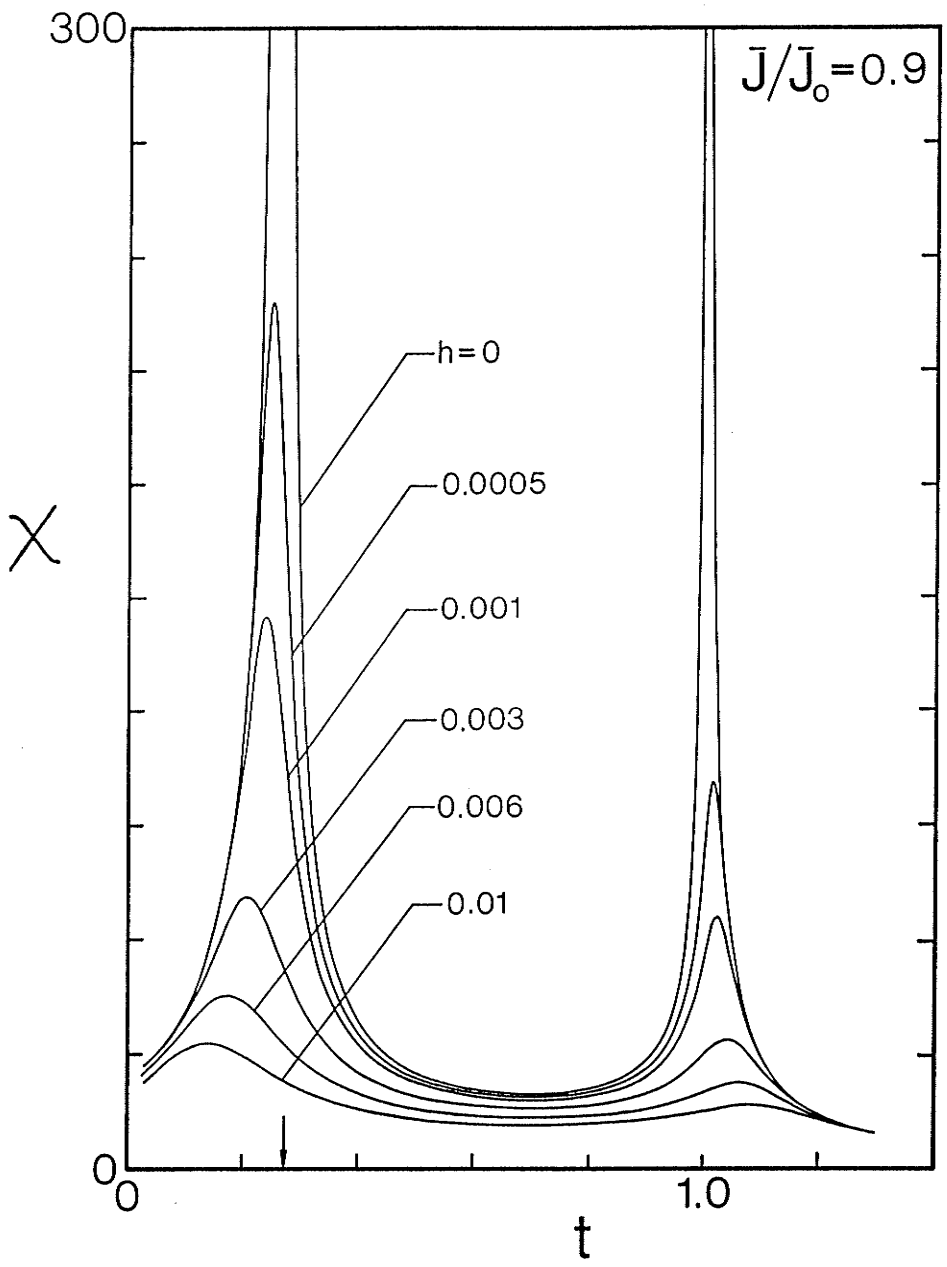

Figure 3.9: The differential susceptibility curves corresponding to the magnetization plots of the previous figure. Again, the arrow indicates T_{SG}.

was plotted versus h and h^2. In this way, it was possible to determine whether the theoretical leading critical behavior occurs in the linear or the non-linear response.

Critical Behavior at the Ferromagnetic Transition

Isotherms for the paramagnetic phase $T > T_c$ and the ferromagnetic phase $T < T_c$ were calculated within the reduced field domain $0 \leq h \leq 10^{-5}$, and for respective reduced temperature ranges of $1.0004 \leq (t = T/T_c) \leq 1.0750$ and $0.9250 \leq t \leq 0.9995$.

Some typical paramagnetic isotherms are plotted versus h^2 in Figure 3.10 to demonstrate the dominance of the quadratic field term in this region. In particular, the zero field slopes represent the values of the coefficient $a_2(t)$ at each temperature, while the extent of the quadratic field dominance is indicated by the field range over which the data are linear. Moreover, as $T \rightarrow T_c$ from above, the higher order susceptibility terms (H^4, H^6, etc.) grow in strength, and a pronounced curvature develops to confine the linear portions to lower and lower fields. Incidently, these same systematics were observed by Kunkel and Williams for the quadratic response of their (**Pd**Fe)Mn system within the paramagnetic region.

The theoretical critical behavior is characterized by the divergence of the zero-field slope as $T \rightarrow T_c$ from above; a power law dependence of the form

$$a_2(t) \sim |t - 1|^{-\gamma}$$

was established, with $\gamma = 4$, by means of the log-log plot of Figure 3.12. The weak deviations from a strict power law are due to non-critical components which

become increasingly evident away from T_c and near the tri-critical point $\eta = 1.0$ (see Yeung et al. 1987).

In Figure 3.11, some typical ferromagnetic isotherms ($T < T_c$) are plotted versus h to show that the magnetic response in this region is dominated by a linear field dependence. (The linear susceptibility is a consequence of the existence below T_c of a spontaneous magnetization component.) As before, the range of dominance for the leading term becomes confined to lower fields as $T \rightarrow T_c$ (from below). Furthermore, the log-log plot of Figure 3.12 reveals a power law divergence of the zero field slope (and hence the linear coefficient) as $T \rightarrow T_c$, but with an exponent $\gamma = 5/2$.

Critical Behavior at the Re-entrant Transition

The isotherms for the ferromagnetic phase $T > T_{SG}$ were generated within the reduced field and temperature domains of $0 \leq h \leq 10^{-5}$ and $1.0015 \leq (t^* = T/T_{SG}) \leq 1.3926$, while those in the re-entrant spin glass phase $T < T_{SG}$ were calculated over the same field range, but with $0.4085 \leq t^* \leq 0.9971$.

As illustrated in Figure 3.13 for the ferromagnetic phase, the presence of a spontaneous magnetization once again results in a dominant linear susceptibility component. The log-log plot of Figure 3.15 indicates a critical divergence of the linear field coefficient, with a power law dependence $|t^* - 1|^{-\gamma}$ and exponent $\gamma = 5/2$. Though not shown explicitly, the model also predicts singular behavior in the quadratic field coefficient, but it is not the dominant term in this region. The corresponding experimental data of Kunkel and Williams does not display a leading linear response; this is probably the result of a ferromagnetic domain

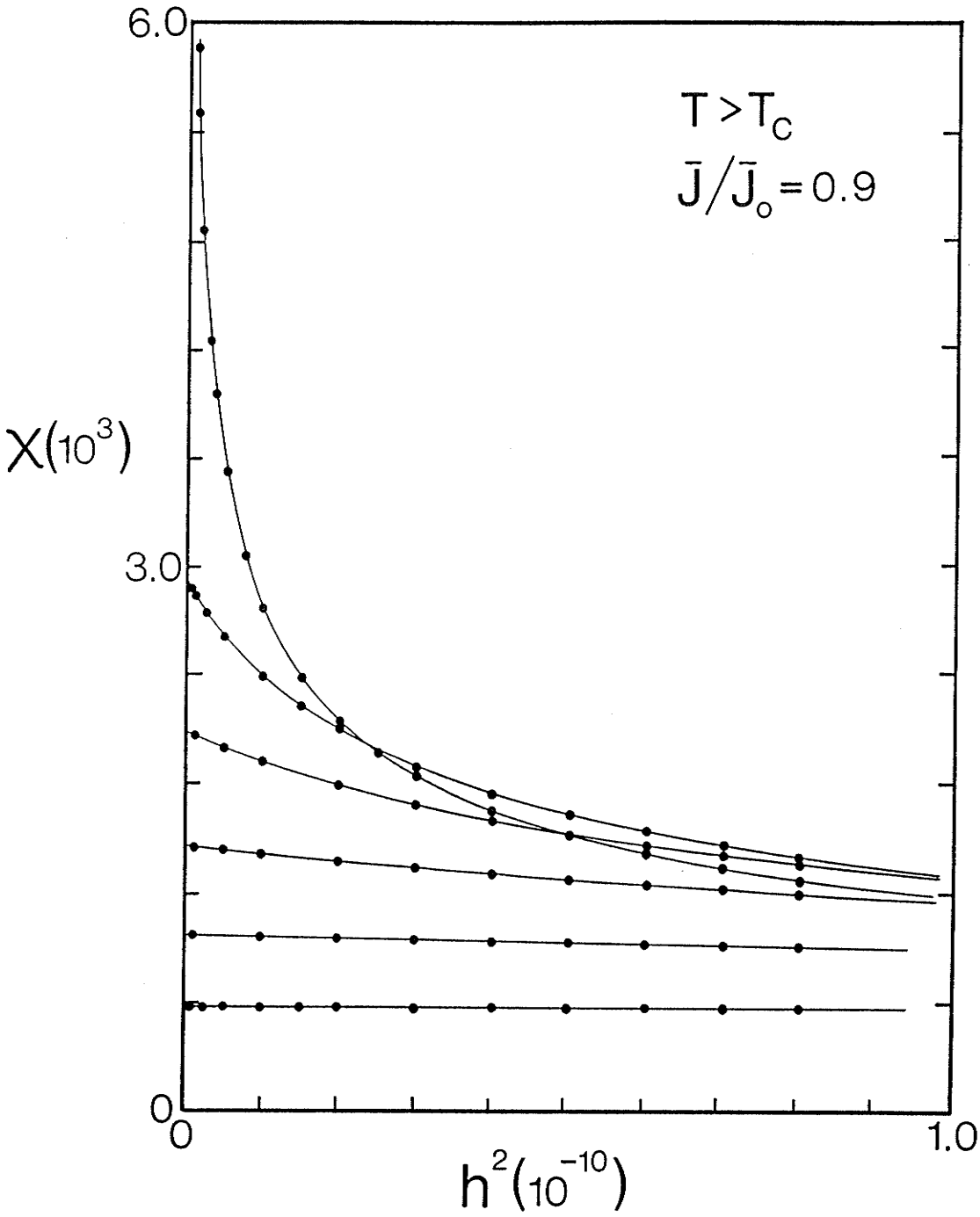

Figure 3.10: Typical theoretical susceptibility isotherms for the paramagnetic region $T > T_c$. In order of decreasing intercept, the reduced temperatures are $t = 1.0004$, 1.0010, 1.0014, 1.0020, 1.0020, 1.0030, and 1.0050. A re-entrant value of $\eta = 0.9$ is used.

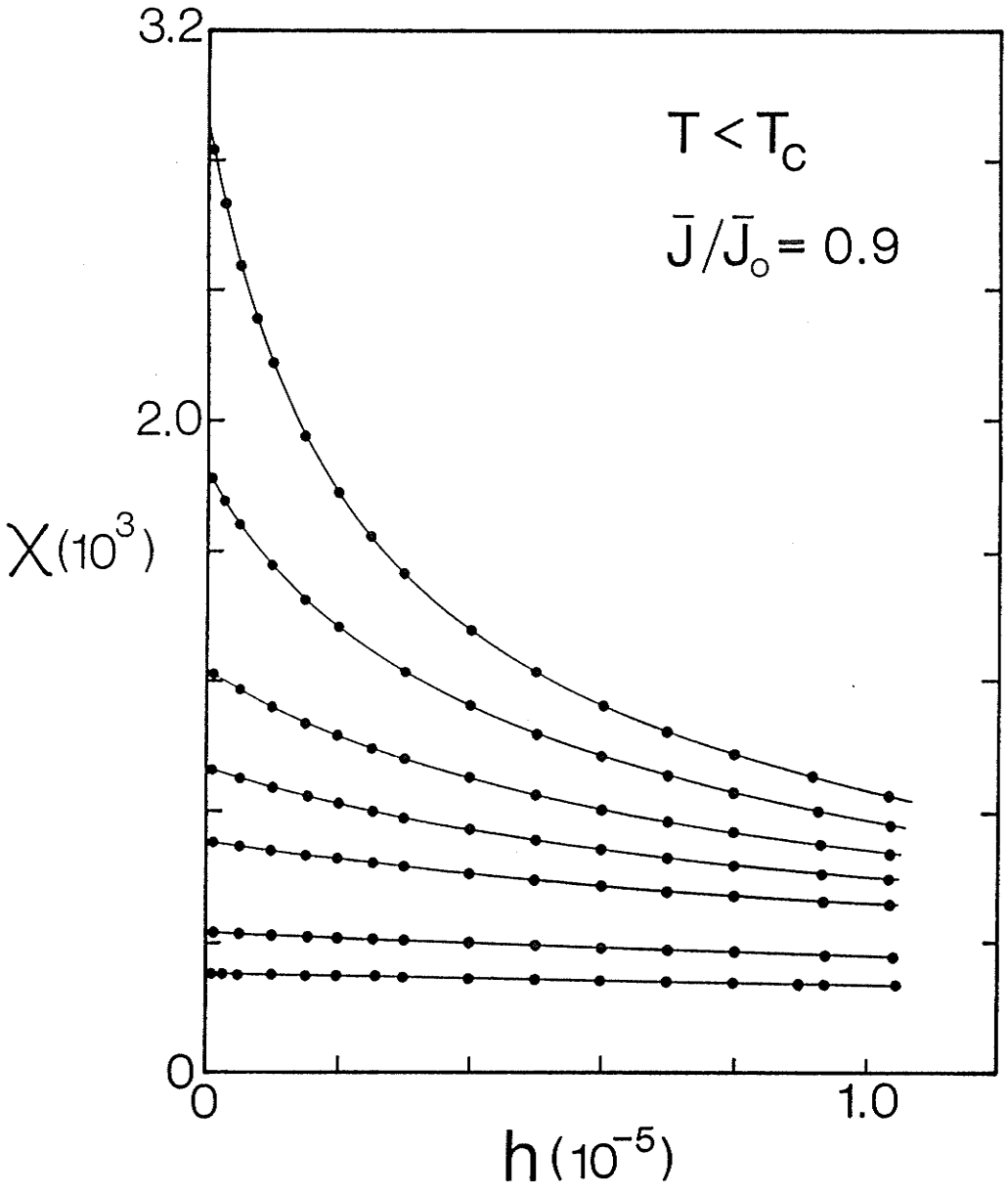

Figure 3.11: Typical theoretical isotherms for the ferromagnetic region $T < T_c$. From top to bottom the reduced temperatures are $t = 0.9995$, 0.9992, 0.9988, 0.9984, 0.9979, 0.9965, and 0.9950.

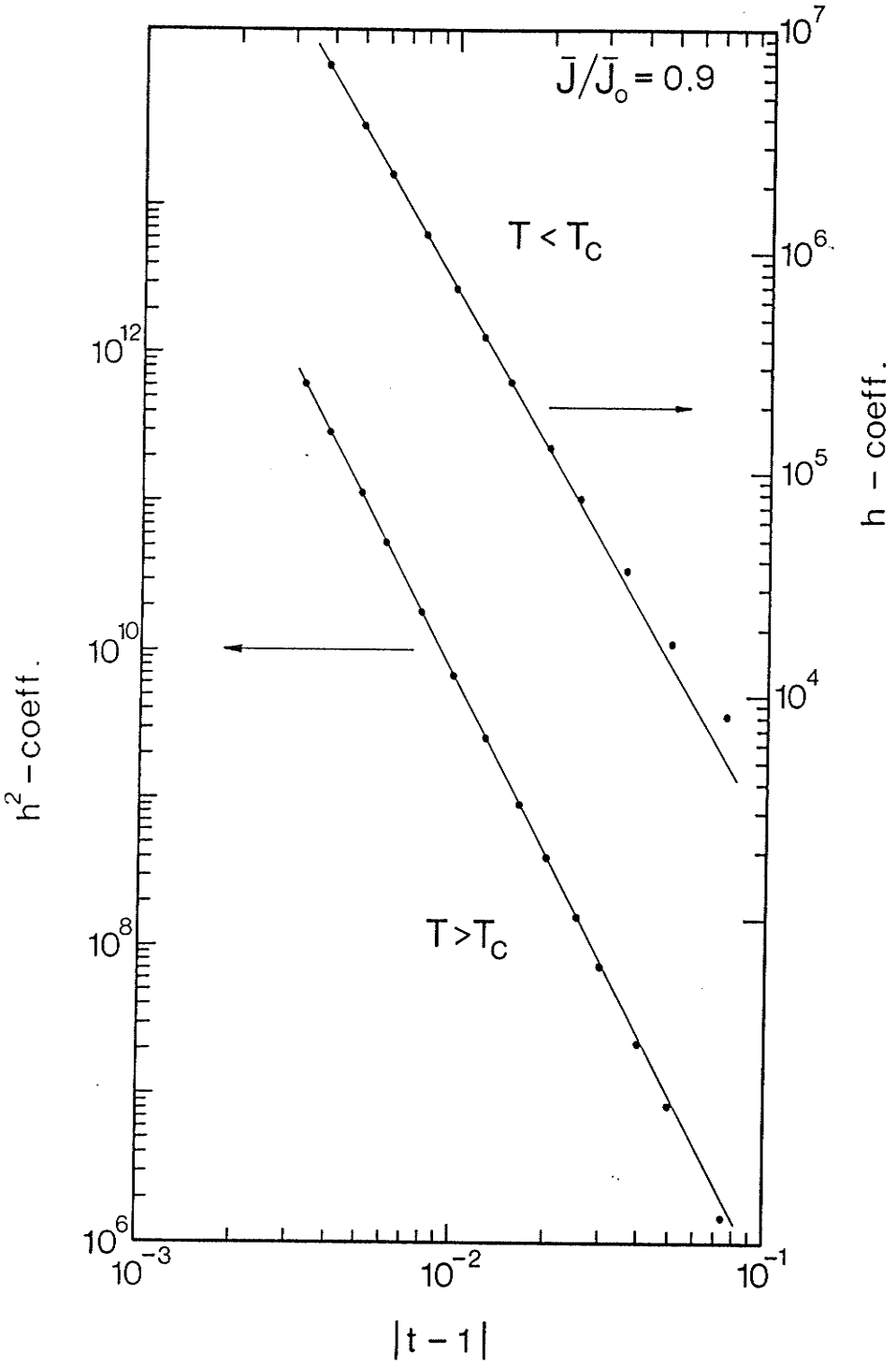

Figure 3.12: Double logarithmic plots of the zero-field slope of the susceptibility isotherms in the viscinity of T_c, as a function of $|t-1|$.

structure which conceals the spontanteous magnetization component. However, they did observe an increase in the quadratic field coefficient which, though too weak to determine a critical exponent, is reminiscent of the theoretical behavior.

Within the re-entrant phase, the model isotherms display features very similar to those found within the paramagnetic phase, and are plotted in Figure 3.14 as a function of h^2. Here the leading field dependence of the susceptibility is quadratic, and the coefficient $a_2(t)$ diverges as a power law with an exponent $\gamma = 4$ (Figure 3.15). Once again, the experimental quadratic coefficient (now on the spin glass side of the transition) does not diverge, though Kunkel and Williams were able to extract a power law dependence, using data far away from T_{SG}, with an exponent $\gamma = 3.6 \pm .6$.

Critical Behavior in the Re-entrant Phase of (PdFe)Mn

A sample of the re-entrant alloy $(\mathbf{Pd}_{0.9965}\mathrm{Fe}_{0.0035})_{0.95}\mathrm{Mn}_{0.05}$ was prepared as a stack of three $11.5 \times 1.2 \times 0.18$ mm^3 strips bound together with masking tape, and electrically insulated from one another to avoid A.C. field skin depth problems. The He^4 cryostat/A.C. susceptometer was used to measure several susceptibility isotherms within the proposed re-entrant spin glass phase of the system. Previous results of Verbeek et al. (1978) and Kunkel et al. (1988) indicate that the transition temperature T_{SG} for this alloy is located just above 4 K.

An A.C. driving field of 16 Hz and amplitude 7 milli-Gauss was applied parallel to the longest axis of the sample, as were the D.C. biasing fields H. However, the field H_i within the sample is effectively given by $H_i = H - DM$,

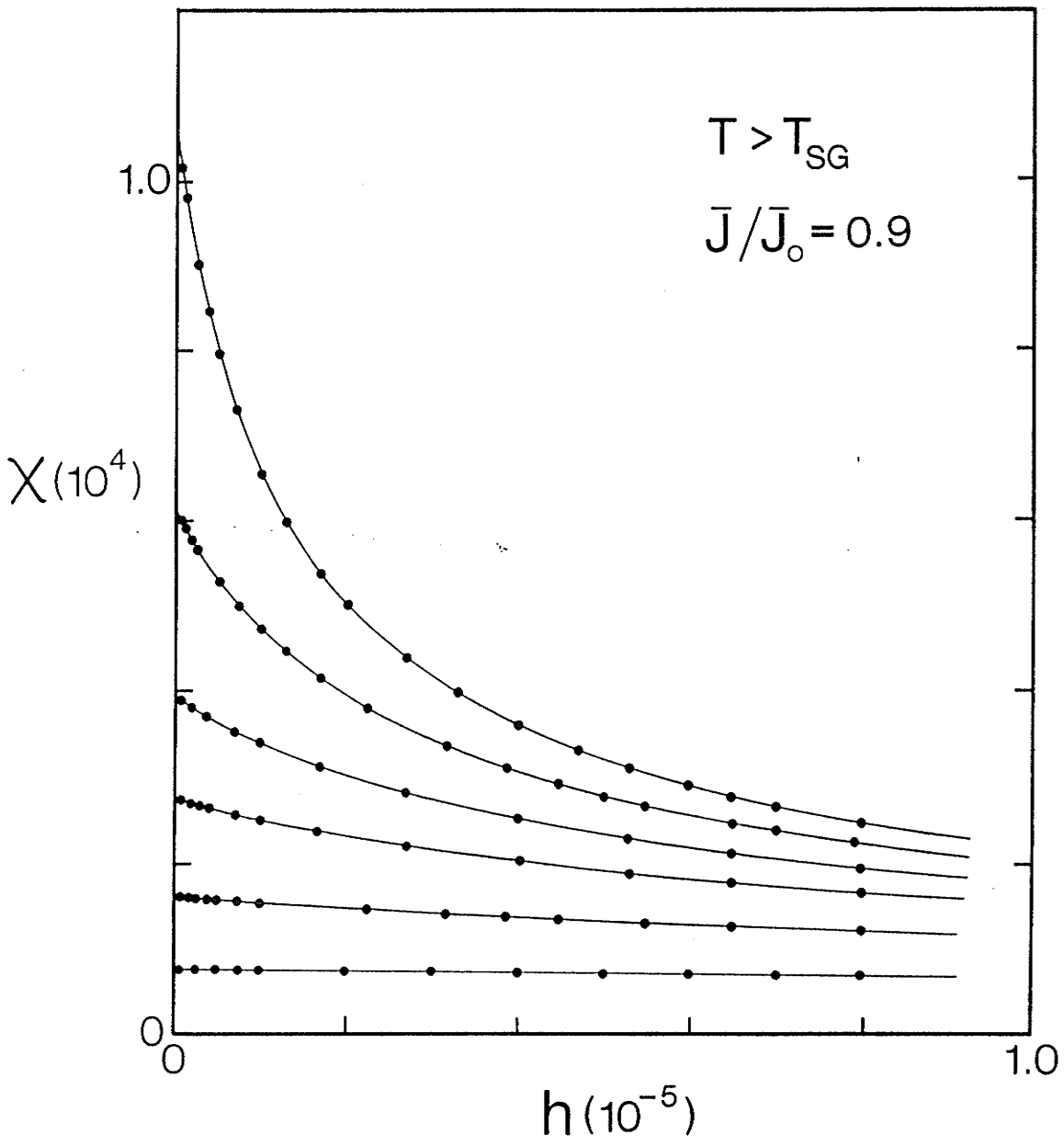

Figure 3.13: Typical theoretical isotherms for the ferromagnetic region $T > T_{SG}$. The reduced temperatures from top to bottom are $t^* = 1.0015$, 1.0027, 1.0041, 1.0060, 1.0101, and 1.0212.

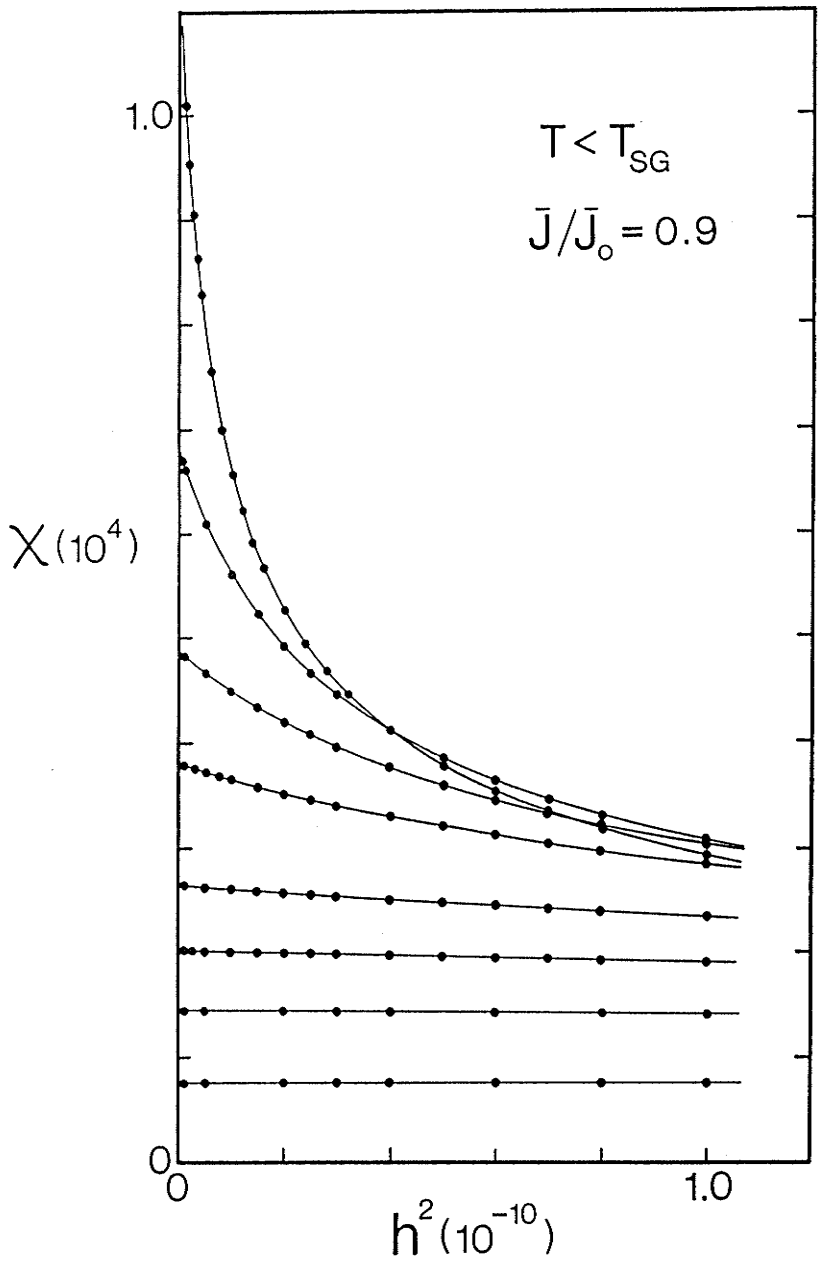

Figure 3.14: Typical theoretical isotherms for the spin glass region $T < T_{SG}$. In order of decreasing vertical intercept, the reduced temperatures are $t^* = 0.9971$, 0.9952, 0.9934, 0.9915, 0.9878, 0.9841, 0.9804, and 0.9581.

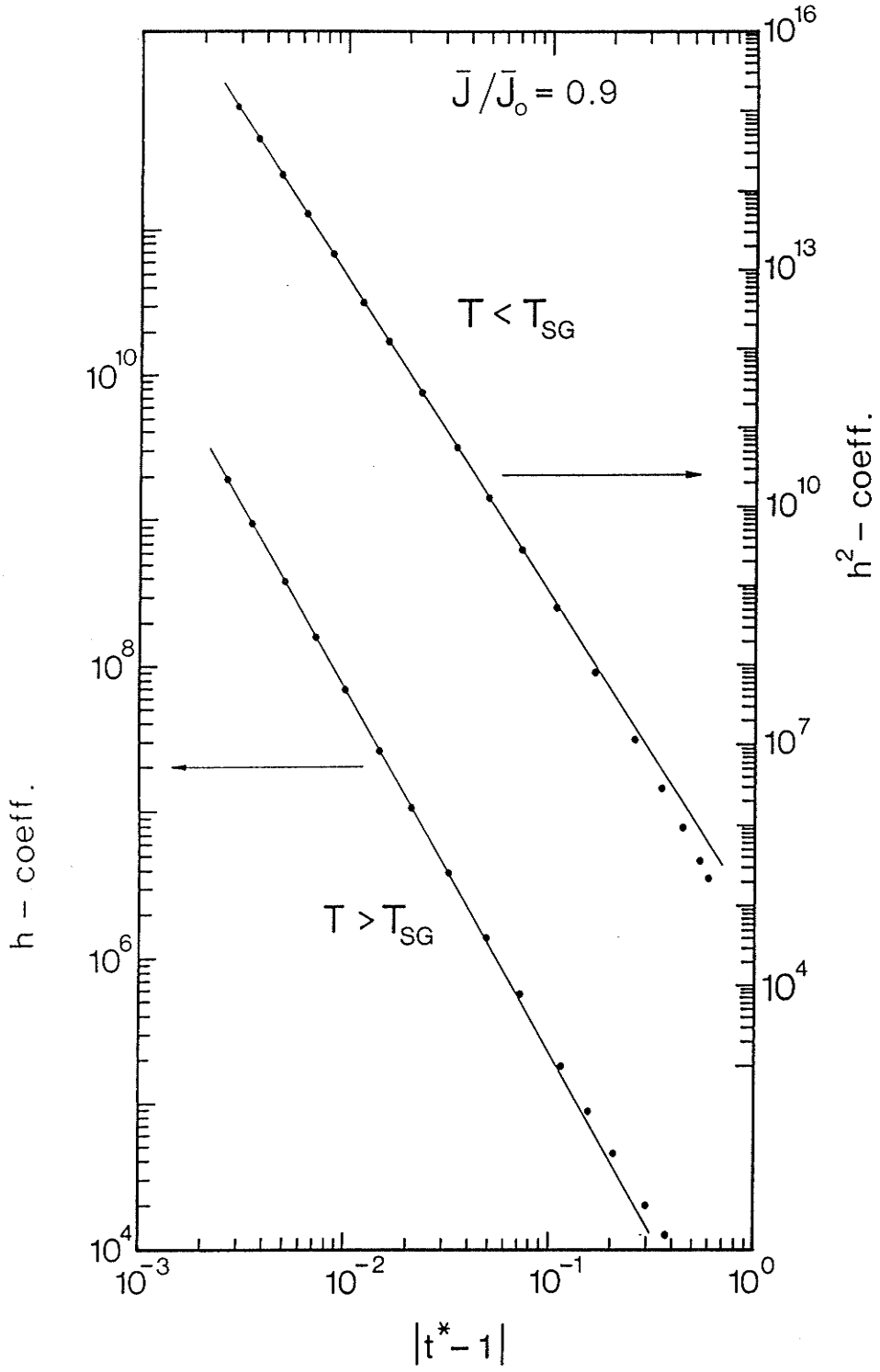

Figure 3.15: Double logarithmic plots of the zero-field slope of the susceptibility isotherms in the viscinity of T_{SG}, as a function of $|t^* - 1|$.

where M is the magnetization of the sample (along the field direction) and $D \approx 0.06$ is the estimated longitudinal demagnetizing factor due to the geometry of the sample. The data were corrected for the demagnetizing effect by means of the expression

$$\chi_{true} = \frac{\chi_{measured}}{1 - D\chi_{measured}} \ ,$$

where $\chi_{measured}$ represents the real component of the complex susceptibility.

Each isotherm was obtained by initially warming the sample above the Curie temperature $T_c \approx 10$ K to remove magnetic remanence, followed by cooling down to the appropriate measuring temperature T. With the temperature stabilized, the magnetization was recorded as the internal field was incremented, in roughly 50 steps, from 0 to 42 Gauss. In Figure 3.16, the isotherms are plotted in terms of χ_{true} versus H_i; though not shown, they all converge to a common saturation value for fields above $H_i \simeq 20$ Gauss. The plots clearly demonstrate the lack of any critical behavior in the linear component of the susceptibility. However, with the isotherms replotted versus H_i^2 (Figure 3.17), the curves bear a remarkable similarity to the theoretical χ versus h^2 plots of Figure 3.14.

Both the model and experimental curves are dominated initially by a quadratic field dependence which shrinks to lower fields as $T \rightarrow T_{SG}$ (again, this is caused by the increasing strength of the higher order field terms in equation 3.1). Also, both sets of curves possess intersecting isotherms which result from the peaked structure of $\chi(T)$ in fixed field. However, while the quadratic coefficient $a_2(t)$ theoretically diverges as $|T - T_{SG}|^{-\gamma}$ with $\gamma = 4$, the experimental coefficients reveal a much less pronounced temperature dependence. Even so, the experimental quadratic coefficient, plotted versus temperature in Figure 3.18,

clearly increases monotonically as $T \rightarrow T_{SG}$, and shows no tendancy to saturate like the zero-field susceptibility (also plotted). Moreover, as illustrated in Figure 3.19, the low temperature data do obey a power law, with an exponent $\gamma = 3.0 \pm 0.4$ roughly the same as the theoretical value.

The deviation from power law behavior as $T \rightarrow T_{SG}$ has also been observed by Zastre et al. (1985) in their study of direct paramagnetic/spin glass transitions in **Pd**Mn. Furthermore, as explained by Kunkel et al. (1988), experiments involving dynamical scaling of spin glass data tend to support the notion that critical slowing down is at least partially to blame. That is, the critical fluctuations of the system become slow enough, near the transition temperature, that the A.C. probing field is unable to register the full amplitude of the magnetic response within the period of oscillation. (An analogous effect occurs at paramagnetic/ferromagnetic transitions, but generally to a lesser extent.) This would certainly result in an underestimate of the coefficient values near T_{SG}, and the same argument might be true of the re-entrant case as well.

Unlike the results of Kunkel and Williams, the present data do <u>not</u> reveal an anomaly in the quadratic field coefficient around 4.07 K, despite the fact that the isotherms extend as high as 4.19 K. Since the coefficients which Kunkel and Williams extracted from their data were, by necessity, based on linear fits to as few as three data-points, while the present SQUID measurements provide well-defined isotherms (even at low fields), it is evident that no anomaly occurs below 4.19 K. Neither of the experiments rule out the existence of an anomaly at higher temperatures, though such measurements were not pursued with the SQUID susceptometer.

Nonetheless, the remarkable similarity between the mean-field re-entrant simulations and the (**Pd**Fe)Mn system, especially in regards to the systematics of the susceptibility isotherms for temperatures within the proposed re-entrant spin glass region, suggests that the experimental system does indeed possess a re-entrant critical transition of the sort defined by the Sherrington-Kirkpatrick model. Perhaps more importantly, the analysis illustrates a potentially valuable technique for identifying such re-entrant transitions.

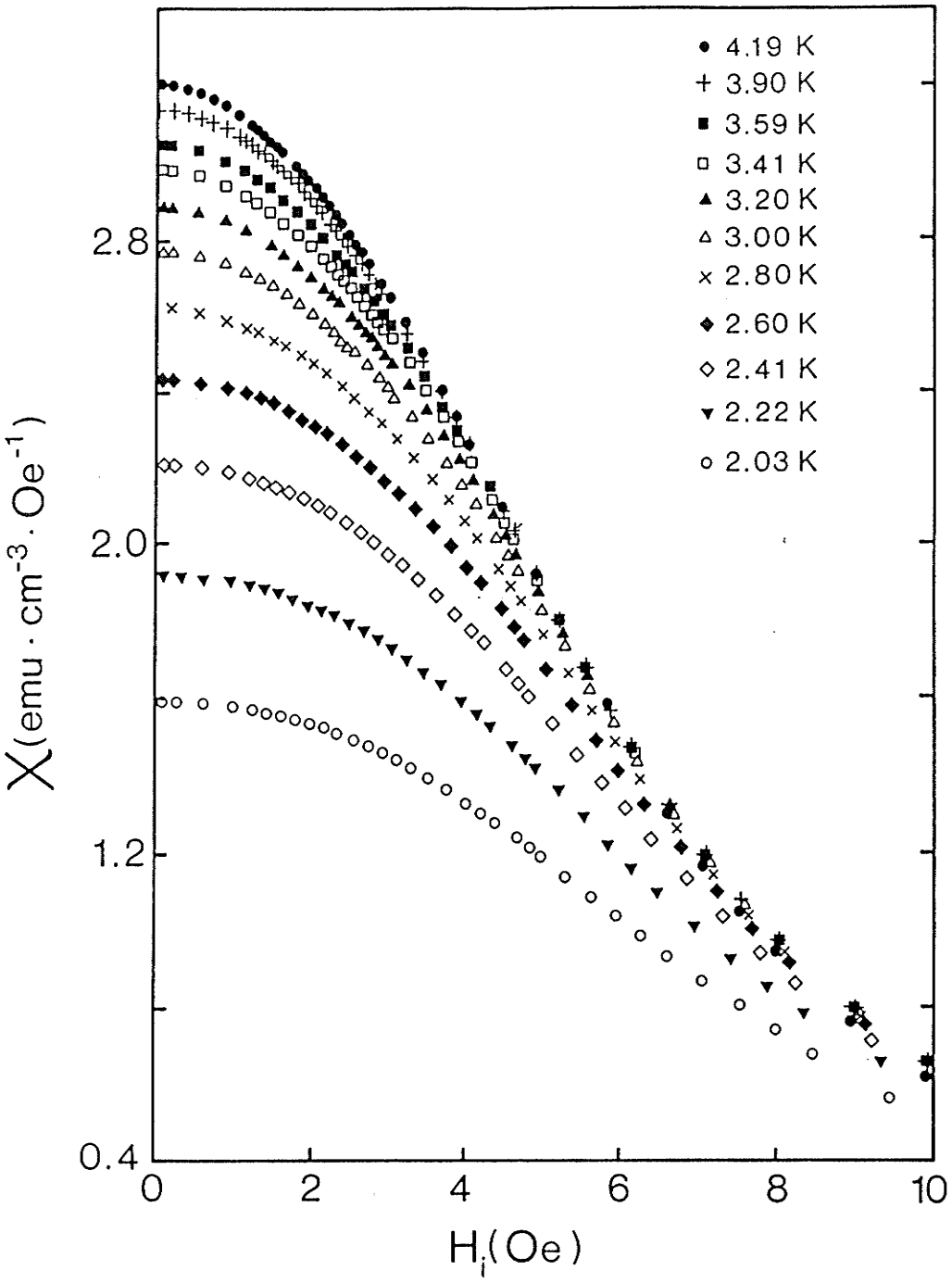

Figure 3.16: A typical set of susceptibility isotherms for the (potentially) re-entrant $(Pd_{0.9965}Fe_{0.0035}) + 5$ *at.*% Mn system, as plotted versus the internal field H_i.

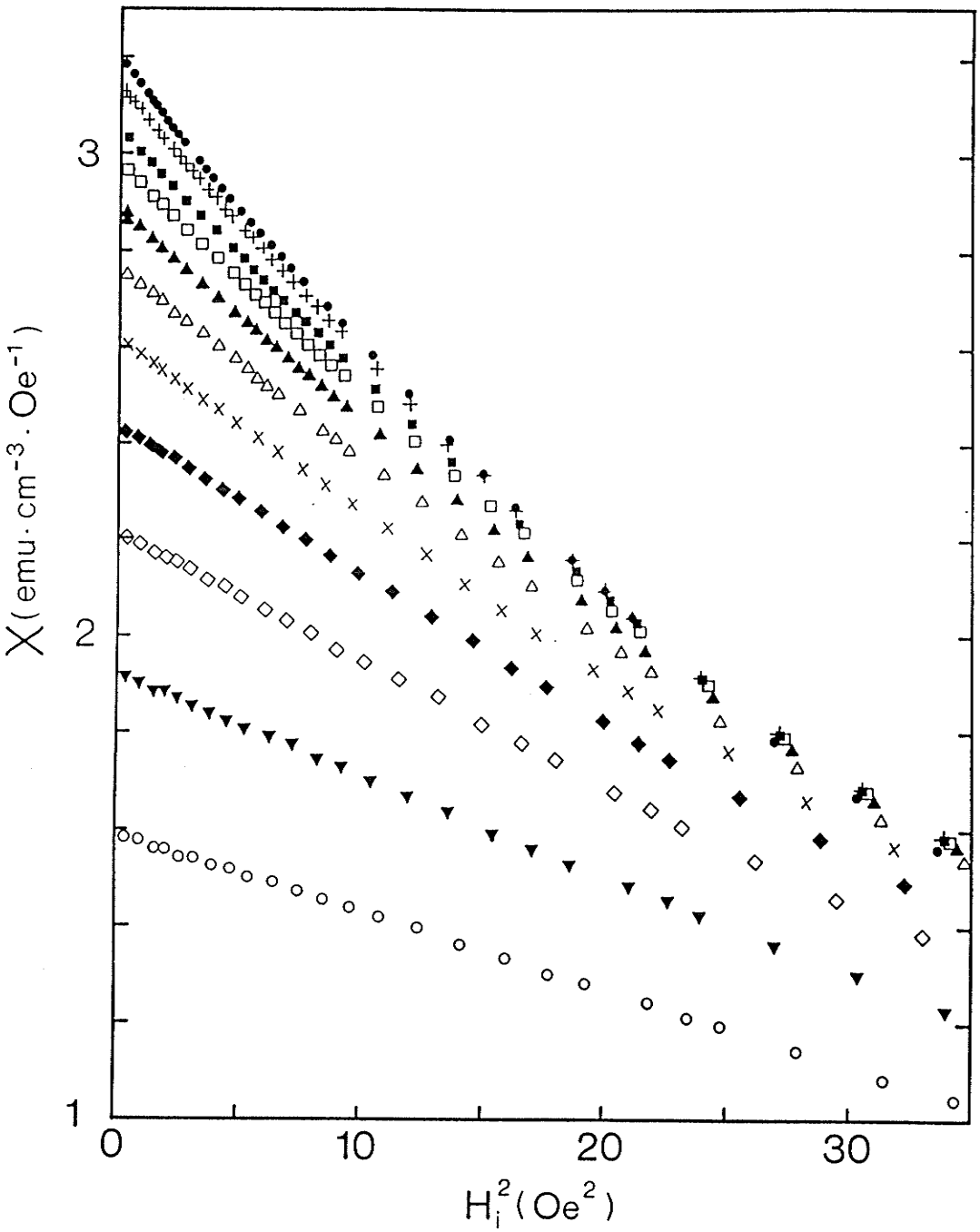

Figure 3.17: The same set of susceptibility isotherms as in the last figure, but re-plotted as a function of H_i^2.

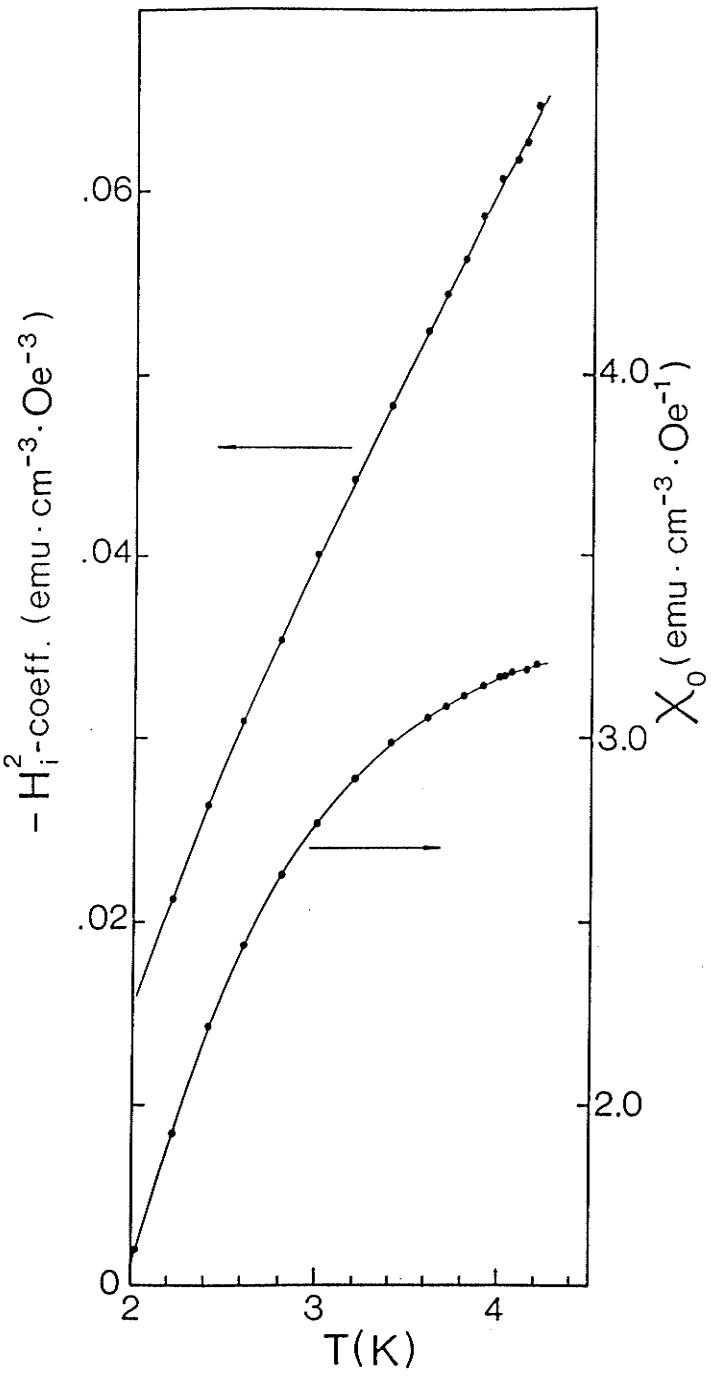

Figure 3.18: Temperature dependence of the quadratic field coefficient and the zero-field susceptibility, as determined from the ($\mathbf{Pd}_{0.9965}\mathrm{Fe}_{0.0035}$) + 5 *at.*% Mn isotherms below 4.2 K.

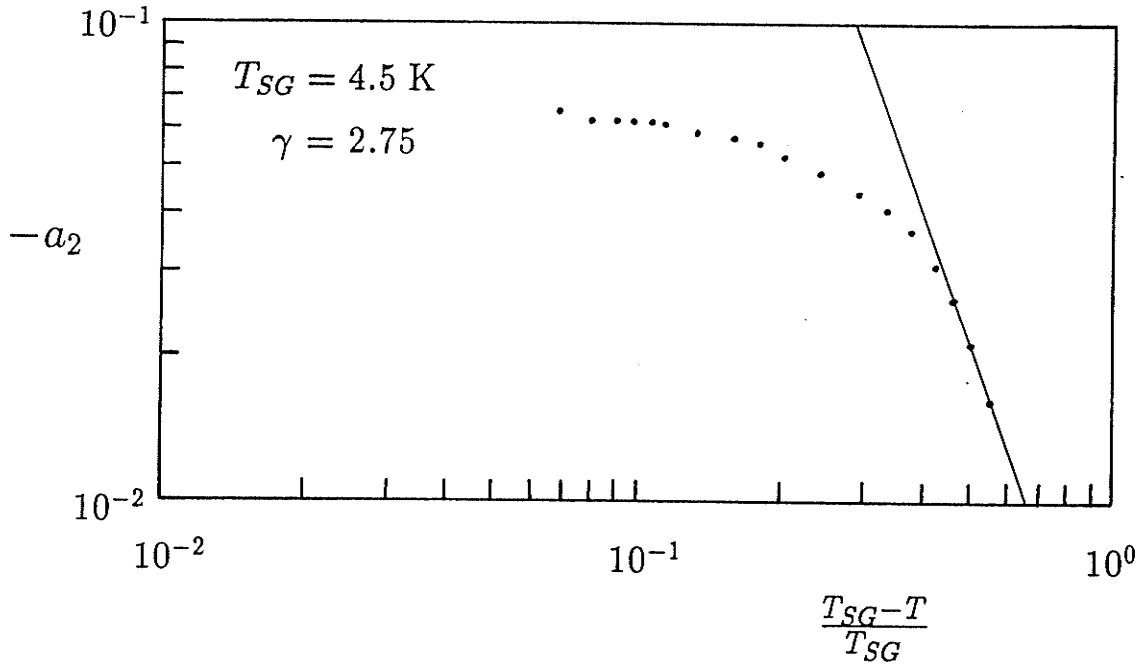

Figure 3.19: A double logarithmic plot of the experimental quadratic field coefficient versus temperature. Assuming that $T_{SG} = 4.5$ K, the low temperature data follow a power law with exponent $\gamma \approx 2.75$. By considering other reasonable guesses for T_{SG}, one gets an exponent of $\gamma = 3.0 \pm .4$.

3.4.3 Discussion of Model Validity

The numerical simulations presented in section 3.4.2 suggest a valuable criterion for experimentally identifying a sequence of genuine phase transitions, from paramagnetic to ferromagnetic to spin glass ordering, and lend support to the contention that the anomalous behavior observed in the (PdFe)Mn system is indeed a manifestation of critical fluctuations. The calculations are based on a particular mean-field version of the Effective Field Model, in which the thermal fluctuations are introduced using a Weiss mean-field approximation, while the exchange bond distribution takes a Gaussian form. Although this hierarchy of approximations yields a set of coupled equations which, aside from being generalized for arbitrary spin, are identical to those obtained by Sherrington and Kirkpatrick (S-K), the corresponding expressions for the free energy and entropy are *different.* Unlike the S-K results, the thermodynamic properties of the Effective Field Model are well behaved at low temperatures, and the third law is <u>not</u> violated (Southern, 1976). Moreover, within the limitations of the effective field approach, the solutions of the coupled equations are not subject to the instabilities normally associated with replica-symmetry breaking below the A-T lines in the S-K phase diagram, and the re-entrant phase boundary is well defined.

In explanation, the Effective Field Model essentially ignores the Onsager reaction-field term $-J_{ij}^2\chi_{jj}m_i$ in the so-called TAP equations for the local magnetization at each spin site (after Thouless et al. 1977):

$$m_i = \tanh\left[\beta\sum_j\left(J_{ij}m_j - J_{ij}^2\chi_{jj}m_i\right)\right] \quad ,$$

where χ_{jj} is the local susceptibility at site j, and unit Ising spins and zero applied field are assumed. The local magnetization m_i at site i arises from the fields $J_{ij}m_j$ created by the neighboring magnetizations m_j, but Thouless et al. argue that the contributions to m_j from m_i should be removed when considering the effects of m_j on m_i. This is accomplished via the reaction-field term. However, its inclusion leads directly to instabilities of the sort encountered in the replica--symmetric S-K solutions. (Recall from section 1.2.5 that the S-K solutions are apparently superceded, below the A-T lines, by those of Parisi.) By avoiding the reaction-field term, the Effective Field Model solutions are able to remain stable throughout the phase diagram, albeit artificially. Moreover, other considerations suggest that the instabilities are not relevant to the experimental situation.

There is reason to believe that, in spite of the A-T instabilities, numerical calculations of the differential susceptibility and magnetization based on the replica-symmetric S-K model, or the Effective Field Model, may possess physical relevance as the theoretical equivalents of dynamical probes such as the (in-phase part of the) A.C. susceptibility and the ZFC magnetization. The peaks observed in susceptibility measurements of **Pd**Mn spin glasses below T_{SG} display systematics, as a function of applied field and temperature, which are replicated remarkably well by the model calculations (Gash et al. 1984). The symmetry, with respect to T_{SG}, of the critical behavior observed in the non-linear components of the **Pd**Mn spin glass susceptibility is also a characteristic of the models (Zastre et al. 1985). Further evidence for such critical symmetry is provided by a recent dynamical study at ultra-low frequencies of the non-linear susceptibility of a very dilute **Ag**Mn spin glass (Levy, 1988): in a static field of 90 Gauss and just below

T_{SG}, the system appears to approach quasistatic thermodynamic equilibrium for applied frequencies less than about 10^{-3} Hz, with an effective non-linear critical exponent γ which is close to its value above T_{SG}, and hence consistent with the predictions of the Effective Field Model (but not with the Parisi solution, which does not yield singular behavior below T_{SG}). In contrast, neither the A.C. susceptibility nor the ZFC magnetization of spin glasses ever seem to exhibit the temperature independent plateau predicted by the Parisi solution (even in the ultra-low frequency limit); this feature appears to be uniquely characteristic of the FC magnetization, which may correspond to the equilibrium response of the system.

The numerical calculations of sections 3.2 and 3.3 indicate that these correlations between experiment and theory extend into the re-entrant region of the magnetic phase diagram as well. The ZFC magnetization curves of three very dilute **Pd**Fe and **Pd**Mn alloys, with concentrations intermediate between those of the usual spin glass and ferromagnetic phases, have been fitted successfully with curves generated numerically in the vicinity of the tri-critical point of the Effective Field Model, using re-entrant values for the parameter $\overline{J}/\overline{J_0}$.

Although the zero field A-T instability line in the ferromagnetic regime of the magnetic phase diagram (Figure 1.21) lies above the re-entrant boundary in temperature, the curvature of the instability surface, plotted with field and $\overline{J}/\overline{J_0}$ as independent variables, is stongly concave up, particularly in the vicinity of the tri-critical point ($\overline{J}/\overline{J_0} = 1$) where the slope $\partial T_{AT}/\partial h$ approaches infinity. This means that the instability temperature in the re-entrant regime is rapidly depressed by the application of a finite field h. While the zero-field boundary itself

may not be visible, manifestations of the transition in finite field, both above and below the re-entrant temperature, will penetrate the surface and survive in the region where the solutions are considered to be stable. (An analogous situation occurs in the pure spin glass regime, where the model susceptibility peaks for fixed field lie above the A-T line, but below the (zero field) critical temperature T_{SG}, and provide a valuable anomaly for comparing theoretical predictions to experimental systematics (Gash et al. 1984).) Thus, while the actual singularity in the non-linear susceptibility may be obscured close to the re-entrant temperature T_{SG}, evidence of the critical behavior in the non-linear components will nonetheless still be identifiable farther from T_{SG}.

Based on these arguments, the mean-field Effective Field Model seems particularly well suited to describing the physics of very dilute magnetic alloys, and its use in developing a meaningful criterion for identifying re-entrant transitions in experimental systems is justified.

3.5 Numerical Solution of the Effective Field Model

The mean-field version of the Effective Field Model for arbitrary spin S (section 1.2.4) yields Sherrington-Kirkpatrick-like coupled equations for the local magnetization m and the order parameter q (equations 1.69 and 1.70). However, for exchange parameters $\eta \equiv \frac{\overline{J}}{J_0} \leq 1.0$, there exists a paramagnetic/ferromagnetic phase transition at temperature $T_c = \frac{S(S+1)\overline{J_0}}{3k_B}$, so that the coupled equations can be written in the form

$$m = \frac{1}{\sqrt{2\pi}} \int_{-\infty}^{+\infty} d\alpha \, \exp\left(\frac{-\alpha^2}{2}\right) \, SB_S[Y] \quad , \tag{3.2}$$

$$q = \frac{1}{\sqrt{2\pi}} \int_{-\infty}^{+\infty} d\alpha \, \exp\left(\frac{-\alpha^2}{2}\right) \, S^2 B_S^2[Y] \quad , \tag{3.3}$$

with

$$Y = \frac{3}{t(S+1)} \left(m + \eta\sqrt{q}\,\alpha + \frac{S(S+1)h}{3} \right) \quad . \tag{3.4}$$

The reduced temperature and reduced field are defined by $t = T/T_c$ and $h = \frac{g\mu_B H}{k_B T_c}$, respectively, where H is the applied field. (Note that the present definition of η is the inverse of that used in the first chapter).

For a particular choice of η, t, and h, the coupled equations were solved numerically by means of the FORTRAN program in Figure 3.20. The Gaussian form of the integrands enabled the infinite integration limits to be replaced by the finite domain $-10 \leq \alpha \leq 10$, with an insignificant loss of accuracy. Evaluation of the integrals was facilitated by dividing the domain into 50 sectors of equal

width Δ, and then applying a 10-point Gauss-Legendre quadrature technique to numerically compute the area corresponding to each sector.

An iterative technique (based on Newton's Method) was used to solve the equations for m and q, with the quality of the solutions characterized by the fractional differences between the left-hand and right-hand sides of equations 3.2 and 3.3. Note that for a system of N spins, the bulk magnetization is given by $M = Ng\mu_B m$, while the saturation value is $M_{sat} = Ng\mu_B S$. These expressions allow direct quantitative comparisons to be made between the theoretical calculations and experimental data.

An expression for the differential magnetic susceptibility $\chi = \frac{\partial m}{\partial h}$ was derived by differentiating equations 3.2 and 3.3 with respect to h and analytically solving for χ. The resulting integral equation, shown below, depends on the values of m and q. Hence,

$$\chi = \frac{\mathcal{N}}{1 - S^2\mathcal{K}_2\mathcal{I}_4 - \frac{3}{S(S+1)}\mathcal{N}} \ , \tag{3.5}$$

where Y and $B_S[Y]$ are defined in equations 3.4 and 1.56, and

$$\begin{aligned}
\mathcal{N} &= S^3\mathcal{K}_1\mathcal{K}_2\left(\mathcal{I}_2\mathcal{I}_3 - \mathcal{I}_1\mathcal{I}_4\right) + S\mathcal{K}_1\mathcal{I}_1 \ , \\
\mathcal{K}_1 &= S/t \ , \\
\mathcal{K}_2 &= \frac{3\eta}{2\sqrt{q}\,t(S+1)} \ , \\
\mathcal{I}_1 &= \frac{1}{\sqrt{2\pi}}\int_{-\infty}^{+\infty} d\alpha \, \exp\left(\frac{-\alpha^2}{2}\right) \frac{\partial B_S[Y]}{\partial Y} \ , \\
\mathcal{I}_2 &= \frac{1}{\sqrt{2\pi}}\int_{-\infty}^{+\infty} d\alpha \, \exp\left(\frac{-\alpha^2}{2}\right) \alpha \frac{\partial B_S[Y]}{\partial Y} \ ,
\end{aligned}$$

$$\mathcal{I}_3 = \frac{2}{\sqrt{2\pi}} \int_{-\infty}^{+\infty} d\alpha \, \exp\left(\frac{-\alpha^2}{2}\right) \, B_S[Y] \, \frac{\partial B_S[Y]}{\partial Y} \ ,$$

$$\mathcal{I}_4 = \frac{2}{\sqrt{2\pi}} \int_{-\infty}^{+\infty} d\alpha \, \exp\left(\frac{-\alpha^2}{2}\right) \, \alpha \, B_S[Y] \, \frac{\partial B_S[Y]}{\partial Y} \ ,$$

$$\frac{\partial B_S[Y]}{\partial Y} = -\left[\frac{2S+1}{2S} \coth\left(\frac{2S+1}{2S} Y\right)\right]^2 + \left[\frac{1}{2S} \coth\left(\frac{Y}{2S}\right)\right]^2 + \frac{S+1}{S} \ .$$

The integrals were evaluated by means of the quadrature technique outlined previously.

```
C*****************************************************************
C  FORTRAN PROGRAM TO CALCULATE THE LOCAL MAGNETIZATION 'MAG', THE
C  ORDER PARAMETER 'ORDER', AND THE DIFFERENTIAL SUSCEPTIBILITY 'SUSC'
C  FROM THE SHERRINGTON-KIRKPATRICK-LIKE COUPLED EQUATIONS OF THE
C  EFFECTIVE FIELD MODEL FOR ARBITRARY SPIN 'S'.  THE RATIO ETA=J/JO
C  CHARACTERIZES THE EXCHANGE BOND DISTRIBUTION.
C
C  TEMP=T/TC=REDUCED TEMPERATURE
C  ETA=J/JO
C  H=G*MU*HA/KB*TC=REDUCED FIELD
C  TSG=GLASS TEMPERATURE=S(S+1)J/3KB
C  TC=CURIE TEMPERATURE=S(S+1)JO/3KB
C
C*****************************************************************
      IMPLICIT REAL*8 (A-H,O-Z)
      DIMENSION X(20),DBRILL(20),
     *ARG(20),COTH1(20),COTH2(20),BRILL(20),
     *FUNCT1(20),FUNCT2(20),W(20),Y(20),A(100),B(100),FUNCT3(20),
     *FUNCT4(20),FUNCT5(20),FUNCT6(20)
      REAL*8 MU,KB,ITEMP,MAG,M,INTEG1,INTEG2,LAMBDA,K1,K2,K3,INTEG3,
     *INTEG4,INTEG5,INTEG6
      INTEGER R
C
C*****************************************************************
C  VARIABLE INITIALIZATION.
      DATA MU/+0.92731D-20/,KB/1.38044D-16/
      C=2.0D0
      S=2.5D0
      ETA=0.9D0
      H=0.0D0
      TEMP=0.8D0
      ITEMP=1.0D0/TEMP
C
C*****************************************************************
C  POSITIONS 'X' AND WIDTHS 'W' OF THE 10-POINT GAUSS-LEGENDRE
C  QUADRATURE INTEGRATION SCHEME.
      X(1)=-0.9739065285D0
      W(1)=0.0666713443D0
      X(2)=-0.8650633667D0
      W(2)=0.1494513492D0
      X(3)=-0.6794095683D0
      W(3)=0.2190863625D0
      X(4)=-0.4333953941D0
      W(4)=0.2692667193D0
      X(5)=-0.1488743389D0
      W(5)=0.2955242247D0
      X(6)=-X(5)
      W(6)=W(5)
      X(7)=-X(4)
      W(7)=W(4)
      X(8)=-X(3)
      W(8)=W(3)
      X(9)=-X(2)
      W(9)=W(2)
      X(10)=-X(1)
      W(10)=W(1)
C
C*****************************************************************
C  SOLVE COUPLED EQUATIONS USING NUMERICAL INTEGRATION AND NEWTON'S
C  METHOD.  'M' AND 'Q' ARE INITIAL GUESS VALUES TO START ITERATION.
C  LAMDA=LIMIT ON DOMAIN OF INTEGRATION,
C  N=NUMBER OF SECTORS,
C  DELTA=WIDTH OF EACH SECTOR, AND
C  R=NUMBER OF ITERATIONS.
      M=0.5D0
      Q=0.5D0
      N=50
      LAMBDA=10.D0
      DELTA=2.D0*LAMBDA/DFLOAT(N)
      FACTOR=S*(S+1.D0)/3.D0
      R=0
   20 CONTINUE
      INTEG1=0.D0
      INTEG2=0.D0
      DO 30 J=1,N
        A(J) = -LAMBDA+DFLOAT(J-1)*DELTA
        B(J) = -LAMBDA+DFLOAT(J)*DELTA
        DO 30 K=1,10
          Y(K) = (B(J)-A(J))*X(K)/2.D0+(B(J)+A(J))/2.D0
          ARG(K) = ITEMP*S*(M   + Y(K)*DSQRT(Q)*ETA + FACTOR*H)/FACTOR
          ARG1 = (2.D0*S+1.D0)*ARG(K)/(2.D0*S)
          ARG2 = ARG(K)/(2.D0*S)
          COTH1(K) = 1.D0/DTANH(ARG1)
          COTH2(K) = 1.D0/DTANH(ARG2)
          BRILL(K) = (2.D0*S+1.D0)*COTH1(K)/(2.D0*S)-COTH2(K)/(2.D0*S)
          FUNCT1(K)= DEXP(-Y(K)**2/2.D0)*S*BRILL(K)/
     *                DSQRT(3.14159265D0*2.D0)
          FUNCT2(K)= DEXP(-Y(K)**2/2.D0)*(S**2)*(BRILL(K)**2)/
     *                DSQRT(2.D0*3.14159265D0)
          INTEG1 = INTEG1 + (B(J)-A(J))*W(K)*FUNCT1(K)/2.D0
          INTEG2 = INTEG2 + (B(J)-A(J))*W(K)*FUNCT2(K)/2.D0
   30 CONTINUE
```

Figure 3.20: A FORTRAN program to numerically solve the coupled equations for m and q, and calculate the differential susceptibility χ.

```
C  HALT CALCULATION IF COUPLED EQUATIONS ARE SOLVED TO ADEQUATE
C  PRECISION, OR R > 40,000 ITERATIONS.
      R=R+1
      DELTA1 = DABS(INTEG1/M-1)
      DELTA2 = DABS(INTEG2/Q-1)
      IF ( DELTA1 .LT. .1D-7 .AND. DELTA2 .LT. .1D-7 ) GO TO 40
      M = INTEG1
      Q = INTEG2
      IF ( R .GT. 40000 ) GO TO 40
      GO TO 20
   40 MAG = INTEG1
      ORDER = INTEG2
C
C*********************************************************************
C  CALCULATION OF DIFFERENTIAL SUSCEPTIBILITY 'SUSC' USING VALUES
C  OF 'MAG' AND 'ORDER' OBTAINED ABOVE.
      K1=S /(TEMP*FACTOR)
      K2=S/TEMP
      K3=S*ETA/(2.D0*DSQRT(ORDER)*TEMP*FACTOR)
      INTEG3=0.D0
      INTEG4=0.D0
      INTEG5=0.D0
      INTEG6=0.D0
      DO 50 J=1,N
        DO 60 K=1,10
        Y(K) = (B(J)-A(J))*X(K)/2.D0+(B(J)+A(J))/2.D0
        ARG(K) = ITEMP*S*(MAG+Y(K)*DSQRT(ORDER)*ETA*FACTOR*H)/
     *           FACTOR
        ARG1=(2.D0*S+1.D0)*ARG(K)/(2.D0*S)
        ARG2=ARG(K)/(2.D0*S)
        COTH1(K) = 1.D0/DTANH(ARG1)
        COTH2(K) = 1.D0/DTANH(ARG2)
        BRILL(K) = (2.D0*S+1.D0)*COTH1(K)/(2.D0*S)-COTH2(K)/(2.D0*S)
        DBRILL(K) = -((2.D0*S+1.D0)*COTH1(K)/(2.D0*S))**2
     *              +(COTH2(K)/(2.D0*S))**2 + (S+1.D0)/S
        FUNCT3(K) = DEXP(-Y(K)**2/2.D0)*DBRILL(K)/
     *              DSQRT(2.D0*3.14159265D0)
        FUNCT4(K) = DEXP(-Y(K)**2/2.D0)*Y(K)*DBRILL(K)/
     *              DSQRT(2.D0*3.14159265D0)
        FUNCT5(K) = 2.D0*DEXP(-Y(K)**2/2.D0)*BRILL(K)*DBRILL(K)/
     *              DSQRT(2.D0*3.14159265D0)
        FUNCT6(K) = 2.D0*DEXP(-Y(K)**2/2.D0)*Y(K)*BRILL(K)*DBRILL(K)/
     *              DSQRT(2.D0*3.14159265D0)
        INTEG3 = INTEG3+(B(J)-A(J))*W(K)*FUNCT3(K)/2.D0
        INTEG4 = INTEG4+(B(J)-A(J))*W(K)*FUNCT4(K)/2.D0
        INTEG5 = INTEG5+(B(J)-A(J))*W(K)*FUNCT5(K)/2.D0
        INTEG6 = INTEG6+(B(J)-A(J))*W(K)*FUNCT6(K)/2.D0
   50 CONTINUE
      SUSCO = (S**3)*K2*K3*(INTEG4*INTEG5-INTEG3*INTEG6)+S*K2*INTEG3
      DEN = 1.D0-(S**2)*K3*INTEG6-SUSCO/FACTOR
      SUSC = SUSCO/DEN
      PRINT S,ETA,H,TEMP,MAG,ORDER,SUSC,R
      STOP
      END
```

3.6 Summary

The static magnetization of three Pd alloy needles (with 700 ppm Fe, 700 ppm Mn, and 1000 ppm Mn) was measured as a function of temperature and applied magnetic field. The characteristic features of the experimental data are duplicated by theoretical re-entrant calculations performed over similar ranges of temperature and field.

For temperatures above and below the proposed re-entrant transition temperature T_{SG}, the thermo-remanent magnetization of the 700 ppm Fe sample displays an essentially logarithmic, or perhaps a stretched-exponential, decay with time. The lack of an anomaly in the relaxation rate as a function of temperature, together with the possibility of a stretched-exponential dependence (albeit weak), suggests that the ferromagnetic and spin glass dynamics are indistinct in re-entrant systems.

Extensive numerical studies of the differential susceptibility provide clear theoretical evidence for the occurrence, in the vicinity of the ferromagnetic/spin glass transition, of a critical anomaly in the non-linear susceptibility components. Furthermore, the systematic behavior of the theoretical isotherms is highly reminiscent of A.C. susceptibility measurements performed within the (proposed) re-entrant spin glass phase of a $(\mathbf{Pd}_{0.9965}\mathrm{Fe}_{0.0035})$ + 5 $at.\%$ Mn sample. The theoretical predictions may provide a practical criterion for identifying critical behavior in experimental re-entrant systems.

Bibliography

[1] Ausloos, M., Elliot, R.J. (editors) *Magnetic Phase Transitions* (1983) Springer-Verlag Press, Berlin.

[2] Binder, K., Young, A.P., *Rev. Mod. Phys.* **58** (1986) p.801.

[3] Bouchiat, H., *J. de Phys.* **47** (1986) p.71.

[4] Carnegie Jr., D.W., Claus, H., *Phys. Rev. B* **20** (1979) p.1280.

[5] Chamberlin, R.V., *Phys. Rev. B* **30** (1984) p.5393.

[6] Chamberlin, R.V., *J. Appl. Phys.* **57** (1985) p.3377.

[7] Chouteau, G., Tournier, R., *J. Phys. Colloq. France* **32** (1971) p.C1-1002.

[8] Cohen-Tannoudji, C., Diu, B., Laloë, F., *Quantum Mechanics, Vol. Two* (1977) John Wiley and Sons, Toronto.

[9] Coles, B.R., Sarkissian, B.V.B., Taylor R.H., *Phil. Mag.* **37** (1978) p.489.

[10] Cragg, D.M., Sherrington, D., Gabay, M., *Phys. Rev. Lett.* **49** (1982) p.158.

[11] Crangle, J., Scott, W.R., *J. of Appl. Phys.* **3** (1965) p.36.

[12] de Almeida, J.R.L., Thouless, D.J., *J. Phys. A* **11** (1978) p.983.

[13] Edwards, S.F., Anderson, P.W., *J. Phys. F* **5** (1975) p.965.

[14] Foner, S. (editor), *Quantum Theory of Magnetism* (1970) McGraw-Hill Co., New York.

[15] Gabay, M., Toulouse, G., *Phys. Rev. Lett.* **47** (1981) p.201.

[16] Gash, P., Roshko, R.M., Williams, G., *J. Phys. F* **14** (1984) p.1501.

[17] Grest, G.S., Soukoulis, C.M., Levin, K., (1983) —see page 183 of reference 1.

[18] Ho, S.C., Maartense, I., Williams, G., *J. Phys. F* **11** (1981) p.1107.

[19] Hoogerbeets, R., Luo, Wei-Li, Orbach, R., *Phys. Rev. Lett.* **55** (1985) p.111.

[20] Hoogerbeets, R., Luo, Wei-Li, Orbach, R., *Phys. Rev. B* **34** (1986) p.1719.

[21] Huang, C.Y., *J. Magn. Magn. Mat.* **51** (1985) p.1.

[22] Kittel, C., *Introduction to Solid State Physics, fifth edition* (1976) John Wiley and Sons, Toronto.

[23] Kittel, C., *Solid State Physics* **22** (1968) p.1.

[24] Kunkel, H.P., Williams, G., *J. Magn. Magn. Mat.* **75** (1988) p.98.

[25] Lounasmaa, O.V., *Experimental Principles and Methods Below 1 K* (1974) Academic Press, New York.

[26] Low, G.G., Holden, J.M., *Proc. Phys. Soc.* **89** (1966) p.119.

[27] Lundgren, L., Svedlindh, P., Beckman, O., *Phys. Rev. B* **26** (1982) p.3990.

[28] Lundgren, L., Svedlindh, P., Nordblad, P., Beckman, O., *Phys. Rev. Lett.* **51** (1983) p.911.

[29] Lundgren, L., *J. Phys. (Paris)* **49** (1988) p.C8-1001.

[30] Mühlschlegal, B., and Zittartz, H., *Zeitschrift für Physik* **175** (1963) p.553.

[31] Mydosh, J.A., Budnick, J.I., Kawatra, M.P., Skalski, S., *Phys. Rev. Lett.* **21** (1968) p.1346.

[32] Nieuwenhuys, G.J., Stocker, H., Mydosh, J.A., *Solid State Comm.* **27** (1978) p. 197.

[33] Nieuwenhuys, G.J., Verbeek, B.H., Mydosh, J.A., *J. Appl. Phys.* **50** (1979) p.1685.

[34] Nordblad, P., Svedlindh, P., Lundgren, L., Sandlund, L., *Phys. Rev. B* **33** (1986) p.645.

[35] Parisi, G., *Phys. Rev. Lett.* **43** (1979) p.1754.

[36] Parisi, G., *Phys. Rep.* **67** (1980) p.25.

[37] Parisi, G., article in *Lecture Notes in Physics, Vol. 149* (1981) p.116, Springer-Verlag, New York.

[38] Parisi, G., Toulouse, G., *J. Phys. (Paris) Lett.* **41** (1980) p.L-361.

[39] Peters, R.P, Buchal, Ch., Kubota, M., Mueller, R.M., Pobell, F., *Phys. Rev. Lett.* **53** (1984) p.1108.

[40] Roshko, R.M., Williams, G., *J. Phys. F* **14** (1984) p.703.

[41] Roshko, R.M., Williams, G., *J. Magn. Magn. Mat.* **50** (1985) p.311.

[42] Sherrington, D., Kirkpatrick, S., *Phys. Rev. Lett.* **35** (1975) p.1792.

[43] Sherrington, D., Kirkpatrick, S., *Phys. Rev. B* **17** (1978) p.4384.

[44] Sherrington, D., Southern, B.W., *J. Phys. F* **5** (1975) p.L-49.

[45] Southern, B.W., *J. Phys. C* **9** (1976) p.4011.

[46] Stanley, H.E., *Introduction to Phase Transitions and Critical Phenomena* (1971) Oxford University Press, Oxford.

[47] Thomson, J.O., Thompson, J.R., *J. Appl. Phys.* **50** (1979) p.7364.

[48] Thouless, D.J., Anderson, P.W., Palmer, R.G., *Philos. Mag.* **35** (1977) p.593.

[49] Toulouse, G., *J. Phys. (Paris) Lett.* **41** (1980) p.L-447.

[50] Toulouse, G., Gabay, M., *J. Phys. (Paris) Lett.* **42** (1981) p.L-103.

[51] Verbeek, B.H., Nieuwenhuys, G.J., Stocker, H., Mydosh, J.A., *Phys. Rev. Lett.* **40** (1978) p.586.

[52] White, R.M., *Quantum Theory of Magnetism* (1970) McGraw-Hill Co., New York.

[53] Yeung, I., Roshko, R.M., Williams, G., *J. Magn. Magn. Mat.* **68** (1987) p.39.

[54] Yeung, W.T.I., *D.C. Magnetization Measurements on Two PtMn Spin Glasses* (1988), Thesis: University of Manitoba.

[55] Zastre, E., Roshko, R.M., Williams, G., *J. Appl. Phys.* **57** (1985) p.3447.

[56] Zastre, E., Roshko, R.M., Williams, G., *Phys. Rev. B* **32** (1985) p.7597.